PHYSICAL REVIEW C **69**, 034909 (2004)

Identified charged particle spectra and yields in Au+Au collisions at $\sqrt{s_{NN}}$=200 GeV

S. S. Adler,[5] S. Afanasiev,[17] C. Aidala,[5] N. N. Ajitanand,[43] Y. Akiba,[20,38] J. Alexander,[43] R. Amirikas,[12] L. Aphecetche,[45] S. H. Aronson,[5] R. Averbeck,[44] T. C. Awes,[35] R. Azmoun,[44] V. Babintsev,[15] A. Baldisseri,[10] K. N. Barish,[6] P. D. Barnes,[27] B. Bassalleck,[33] S. Bathe,[30] S. Batsouli,[9] V. Baublis,[37] A. Bazilevsky,[39,15] S. Belikov,[16,15] Y. Berdnikov,[40] S. Bhagavatula,[16] J. G. Boissevain,[27] H. Borel,[10] S. Borenstein,[25] M. L. Brooks,[27] D. S. Brown,[34] N. Bruner,[33] D. Bucher,[30] H. Buesching,[30] V. Bumazhnov,[15] G. Bunce,[5,39] J. M. Burward-Hoy,[26,44] S. Butsyk,[44] X. Camard,[45] J.-S. Chai,[18] P. Chand,[4] W. C. Chang,[2] S. Chernichenko,[15] C. Y. Chi,[9] J. Chiba,[20] M. Chiu,[9] I. J. Choi,[52] J. Choi,[19] R. K. Choudhury,[4] T. Chujo,[5] V. Cianciolo,[35] Y. Cobigo,[10] B. A. Cole,[9] P. Constantin,[16] D. G. d'Enterria,[45] G. David,[5] H. Delagrange,[45] A. Denisov,[15] A. Deshpande,[39] E. J. Desmond,[5] O. Dietzsch,[41] O. Drapier,[25] A. Drees,[44] R. du Rietz,[29] A. Durum,[15] D. Dutta,[4] Y. V. Efremenko,[35] K. El Chenawi,[49] A. Enokizono,[14] H. En'yo,[38,39] S. Esumi,[48] L. Ewell,[5] D. E. Fields,[33,39] F. Fleuret,[25] S. L. Fokin,[23] B. D. Fox,[39] Z. Fraenkel,[51] J. E. Frantz,[9] A. Franz,[5] A. D. Frawley,[12] S.-Y. Fung,[6] S. Garpman,[29,*] T. K. Ghosh,[49] A. Glenn,[46] G. Gogiberidze,[46] M. Gonin,[25] J. Gosset,[10] Y. Goto,[39] R. Granier de Cassagnac,[25] N. Grau,[16] S. V. Greene,[49] M. Grosse Perdekamp,[39] W. Guryn,[5] H.-Å. Gustafsson,[29] T. Hachiya,[14] J. S. Haggerty,[5] H. Hamagaki,[8] A. G. Hansen,[27] E. P. Hartouni,[26] M. Harvey,[5] R. Hayano,[8] X. He,[13] M. Heffner,[26] T. K. Hemmick,[44] J. M. Heuser,[44] M. Hibino,[50] J. C. Hill,[16] W. Holzmann,[43] K. Homma,[14] B. Hong,[22] A. Hoover,[34] T. Ichihara,[38,39] V. V. Ikonnikov,[23] K. Imai,[24,38] D. Isenhower,[1] M. Ishihara,[38] M. Issah,[43] A. Isupov,[17] B. V. Jacak,[44] W. Y. Jang,[22] Y. Jeong,[19] J. Jia,[44] O. Jinnouchi,[38] B. M. Johnson,[5] S. C. Johnson,[26] K. S. Joo,[31] D. Jouan,[36] S. Kametani,[8,50] N. Kamihara,[47,38] J. H. Kang,[52] S. S. Kapoor,[4] K. Katou,[50] S. Kelly,[9] B. Khachaturov,[51] A. Khanzadeev,[37] J. Kikuchi,[50] D. H. Kim,[31] D. J. Kim,[52] D. W. Kim,[19] E. Kim,[42] G.-B. Kim,[25] H. J. Kim,[52] E. Kistenev,[5] A. Kiyomichi,[48] K. Kiyoyama,[32] C. Klein-Boesing,[30] H. Kobayashi,[38,39] L. Kochenda,[37] V. Kochetkov,[15] D. Koehler,[33] T. Kohama,[14] M. Kopytine,[44] D. Kotchetkov,[6] A. Kozlov,[51] P. J. Kroon,[5] C. H. Kuberg,[1,27] K. Kurita,[39] Y. Kuroki,[48] M. J. Kweon,[22] Y. Kwon,[52] G. S. Kyle,[34] R. Lacey,[43] V. Ladygin,[17] J. G. Lajoie,[16] A. Lebedev,[16,23] S. Leckey,[44] D. M. Lee,[27] S. Lee,[19] M. J. Leitch,[27] X. H. Li,[6] H. Lim,[42] A. Litvinenko,[17] M. X. Liu,[27] Y. Liu,[36] C. F. Maguire,[49] Y. I. Makdisi,[5] A. Malakhov,[17] V. I. Manko,[23] Y. Mao,[7,38] G. Martinez,[45] M. D. Marx,[44] H. Masui,[48] F. Matathias,[44] T. Matsumoto,[8,50] P. L. McGaughey,[27] E. Melnikov,[15] F. Messer,[44] Y. Miake,[48] J. Milan,[43] T. E. Miller,[49] A. Milov,[44,51] S. Mioduszewski,[5] R. E. Mischke,[27] G. C. Mishra,[13] J. T. Mitchell,[5] A. K. Mohanty,[4] D. P. Morrison,[5] J. M. Moss,[27] F. Mühlbacher,[44] D. Mukhopadhyay,[51] M. Muniruzzaman,[6] J. Murata,[38,39] S. Nagamiya,[20] J. L. Nagle,[9] T. Nakamura,[14] B. K. Nandi,[6] M. Nara,[48] J. Newby,[46] P. Nilsson,[29] A. S. Nyanin,[23] J. Nystrand,[29] E. O'Brien,[5] C. A. Ogilvie,[16] H. Ohnishi,[5,38] I. D. Ojha,[49,3] K. Okada,[38] M. Ono,[48] V. Onuchin,[15] A. Oskarsson,[29] I. Otterlund,[29] K. Oyama,[8] K. Ozawa,[8] D. Pal,[51] A. P.T. Palounek,[27] V. S. Pantuev,[44] V. Papavassiliou,[34] J. Park,[42] A. Parmar,[33] S. F. Pate,[34] T. Peitzmann,[30] J.-C. Peng,[27] V. Peresedov,[17] C. Pinkenburg,[5] R. P. Pisani,[5] F. Plasil,[35] M. L. Purschke,[5] A. K. Purwar,[44] J. Rak,[16] I. Ravinovich,[51] K. F. Read,[35,46] M. Reuter,[44] K. Reygers,[30] V. Riabov,[37,40] Y. Riabov,[37] G. Roche,[28] A. Romana,[25] M. Rosati,[16] P. Rosnet,[28] S. S. Ryu,[52] M. E. Sadler,[1] N. Saito,[38,39] T. Sakaguchi,[8,50] M. Sakai,[32] S. Sakai,[48] V. Samsonov,[37] L. Sanfratello,[33] R. Santo,[30] H. D. Sato,[24,38] S. Sato,[5,48] S. Sawada,[20] Y. Schutz,[45] V. Semenov,[15] R. Seto,[6] M. R. Shaw,[1,27] T. K. Shea,[5] T.-A. Shibata,[47,38] K. Shigaki,[14,20] T. Shiina,[27] C. L. Silva,[41] D. Silvermyr,[27,29] K. S. Sim,[22] C. P. Singh,[3] V. Singh,[3] M. Sivertz,[5] A. Soldatov,[15] R. A. Soltz,[26] W. E. Sondheim,[27] S. P. Sorensen,[46] I. V. Sourikova,[5] F. Staley,[10] P. W. Stankus,[35] E. Stenlund,[29] M. Stepanov,[34] A. Ster,[21] S. P. Stoll,[5] T. Sugitate,[14] J. P. Sullivan,[27] E. M. Takagui,[41] A. Taketani,[38,39] M. Tamai,[50] K. H. Tanaka,[20] Y. Tanaka,[32] K. Tanida,[38] M. J. Tannenbaum,[5] P. Tarján,[11] J. D. Tepe,[1,27] T. L. Thomas,[33] J. Tojo,[24,38] H. Torii,[24,38] R. S. Towell,[1] I. Tserruya,[51] H. Tsuruoka,[48] S. K. Tuli,[3] H. Tydesjö,[29] N. Tyurin,[15] H. W. van Hecke,[27] J. Velkovska,[5,44] M. Velkovsky,[44] L. Villatte,[46] A. A. Vinogradov,[23] M. A. Volkov,[23] E. Vznuzdaev,[37] X. R. Wang,[13] Y. Watanabe,[38,39] S. N. White,[5] F. K. Wohn,[16] C. L. Woody,[5] W. Xie,[6] Y. Yang,[7] A. Yanovich,[15] S. Yokkaichi,[38,39] G. R. Young,[35] I. E. Yushmanov,[23] W. A. Zajc,[9,†] C. Zhang,[9] S. Zhou,[7] S. J. Zhou,[51] and L. Zolin[17]

(PHENIX Collaboration)

[1]*Abilene Christian University, Abilene, Texas 79699, USA*
[2]*Institute of Physics, Academia Sinica, Taipei 11529, Taiwan*
[3]*Department of Physics, Banaras Hindu University, Varanasi 221005, India*
[4]*Bhabha Atomic Research Centre, Bombay 400 085, India*
[5]*Brookhaven National Laboratory, Upton, New York 11973-5000, USA*
[6]*University of California—Riverside, Riverside, California 92521, USA*
[7]*China Institute of Atomic Energy (CIAE), Beijing, People's Republic of China*
[8]*Center for Nuclear Study, Graduate School of Science, University of Tokyo, 7-3-1 Hongo, Bunkyo, Tokyo 113-0033, Japan*
[9]*Columbia University, New York, New York 10027, USA and Nevis Laboratories, Irvington, New York 10533, USA*
[10]*Dapnia, CEA Saclay, F-91191 Gif-sur-Yvette, France*
[11]*Debrecen University, H-4010 Debrecen, Egyetem tér 1, Hungary*
[12]*Florida State University, Tallahassee, Florida 32306, USA*
[13]*Georgia State University, Atlanta, Georgia 30303, USA*
[14]*Hiroshima University, Kagamiyama, Higashi-Hiroshima 739-8526, Japan*
[15]*Institute for High Energy Physics (IHEP), Protvino, Russia*

0556-2813/2004/69(3)/034909(32)/$22.50

[16]*Iowa State University, Ames, Iowa 50011, USA*
[17]*Joint Institute for Nuclear Research, 141980 Dubna, Moscow Region, Russia*
[18]*KAERI, Cyclotron Application Laboratory, Seoul, South Korea*
[19]*Kangnung National University, Kangnung 210-702, South Korea*
[20]*KEK, High Energy Accelerator Research Organization, Tsukuba-shi, Ibaraki-ken 305-0801, Japan*
[21]*KFKI Research Institute for Particle and Nuclear Physics (RMKI), H-1525 Budapest 114, P. O. Box 49, Hungary*
[22]*Korea University, Seoul 136-701, Korea*
[23]*Russian Research Center "Kurchatov Institute," Moscow, Russia*
[24]*Kyoto University, Kyoto 606, Japan*
[25]*Laboratoire Leprince-Ringuet, Ecole Polytechnique, CNRS-IN2P3, Route de Saclay, F-91128 Palaiseau, France*
[26]*Lawrence Livermore National Laboratory, Livermore, California 94550, USA*
[27]*Los Alamos National Laboratory, Los Alamos, New Mexico 87545, USA*
[28]*LPC, Université Blaise Pascal, CNRS-IN2P3, Clermont-Fd, 63177 Aubiere Cedex, France*
[29]*Department of Physics, Lund University, Box 118, SE-221 00 Lund, Sweden*
[30]*Institut fuer Kernphysik, University of Muenster, D-48149 Muenster, Germany*
[31]*Myongji University, Yongin, Kyonggido 449-728, Korea*
[32]*Nagasaki Institute of Applied Science, Nagasaki-shi, Nagasaki 851-0193, Japan*
[33]*University of New Mexico, Albuquerque, New Mexico 87131, USA*
[34]*New Mexico State University, Las Cruces, New Mexico 88003, USA*
[35]*Oak Ridge National Laboratory, Oak Ridge, Tennessee 37831, USA*
[36]*IPN-Orsay, Universite Paris Sud, CNRS-IN2P3, BP1, F-91406 Orsay, France*
[37]*PNPI, Petersburg Nuclear Physics Institute, Gatchina, Russia*
[38]*RIKEN (The Institute of Physical and Chemical Research), Wako, Saitama 351-0198, Japan*
[39]*RIKEN BNL Research Center, Brookhaven National Laboratory, Upton, New York 11973-5000, USA*
[40]*St. Petersburg State Technical University, St. Petersburg, Russia*
[41]*Universidade de São Paulo, Instituto de Física, Caixa Postal 66318, São Paulo CEP05315-970, Brazil*
[42]*System Electronics Laboratory, Seoul National University, Seoul, South Korea*
[43]*Chemistry Department, Stony Brook University, SUNY, Stony Brook, New York 11794-3400, USA*
[44]*Department of Physics and Astronomy, Stony Brook University, SUNY, Stony Brook, New York 11794, USA*
[45]*SUBATECH (Ecole des Mines de Nantes, CNRS-IN2P3, Université de Nantes), BP 20722, 44307 Nantes, France*
[46]*University of Tennessee, Knoxville, Tennessee 37996, USA*
[47]*Department of Physics, Tokyo Institute of Technology, Tokyo 152-8551, Japan*
[48]*Institute of Physics, University of Tsukuba, Tsukuba, Ibaraki 305, Japan*
[49]*Vanderbilt University, Nashville, Tennessee 37235, USA*
[50]*Waseda University, Advanced Research Institute for Science and Engineering, 17 Kikui-cho, Shinjuku-ku, Tokyo 162-0044, Japan*
[51]*Weizmann Institute, Rehovot 76100, Israel*
[52]*Yonsei University, IPAP, Seoul 120-749, Korea*

(Received 28 July 2003; published 29 March 2004)

The centrality dependence of transverse momentum distributions and yields for $\pi^{\pm}, K^{\pm}, p$, and $\bar{p}$ in Au+Au collisions at $\sqrt{s_{NN}}$=200 GeV at midrapidity are measured by the PHENIX experiment at the Relativistic Heavy Ion Collider. We observe a clear particle mass dependence of the shapes of transverse momentum spectra in central collisions below $\sim$2 GeV/c in p_T. Both mean transverse momenta and particle yields per participant pair increase from peripheral to midcentral and saturate at the most central collisions for all particle species. We also measure particle ratios of π^-/π^+, K^-/K^+, $\bar{p}/p$, K/π, p/π, and $\bar{p}/\pi$ as a function of p_T and collision centrality. The ratios of equal mass particle yields are independent of p_T and centrality within the experimental uncertainties. In central collisions at intermediate transverse momenta $\sim$1.5–4.5 GeV/c, proton and antiproton yields constitute a significant fraction of the charged hadron production and show a scaling behavior different from that of pions.

DOI: 10.1103/PhysRevC.69.034909 PACS number(s): 25.75.Dw

*Deceased.
†PHENIX spokesperson.
Email address: zajc@nevis.columbia.edu

I. INTRODUCTION

The motivation for ultrarelativistic heavy-ion experiments at the Relativistic Heavy Ion Collider (RHIC) at Brookhaven National Laboratory is the study of nuclear matter at extremely high temperature and energy density with the hope of creating and detecting deconfined matter consisting of quarks and gluons—the quark gluon plasma (QGP). Lattice QCD calculations [1] predict that the transition to a deconfined state occurs at a critical temperature $T_c \approx 170$ MeV and an energy density $\epsilon \approx 2$ GeV/fm^3. Based on the Bjorken estimation [2] and the measurement of transverse energy (E_T) in Au+Au collisions at $\sqrt{s_{NN}}=130$ GeV [3] and 200 GeV, the spatial energy density in central Au+Au collisions at RHIC is believed to be high enough to create such deconfined matter in a laboratory [3].

The hot and dense matter produced in relativistic heavy-ion collisions may evolve through the following scenario: preequilibrium, thermal (or chemical) equilibrium of partons, possible formation of QGP or a QGP-hadron gas mixed state, a gas of hot interacting hadrons, and finally, a freeze-out state when the produced hadrons no longer strongly interact with each other. Since produced hadrons carry information about the collision dynamics and the entire space-time evolution of the system from the initial to the final stage of collisions, a precise measure of the transverse momentum (p_T) distributions and yields of identified hadrons as a function of collision geometry is essential for the understanding of the dynamics and properties of the created matter.

In the low p_T region (<2 GeV/c), hydrodynamic models [4,5] that include radial flow successfully describe the measured p_T distributions in Au+Au collisions at $\sqrt{s_{NN}}$ =130 GeV [6–8]. The p_T spectra of identified charged hadrons below $p_T \approx 2$ GeV/c in central collisions have been well reproduced by two simple parameters: transverse flow velocity β_T and freeze-out temperature T_{fo} [8] under the assumption of thermalization with longitudinal and transverse flow [4]. The particle production in this p_T region is considered to be dominated by secondary interactions among produced hadrons and participating nucleons in the reaction zone. Another model which successfully describes the particle abundances at low p_T is the statistical thermal model [9]. Particle ratios have been shown to be well reproduced by two parameters: a baryon chemical potential μ_B and a chemical freeze-out temperature T_{ch}. It is found that there is an overall good agreement between measured particle ratios at $\sqrt{s_{NN}}=130$ GeV Au+Au and the thermal model calculations [10,11].

On the other hand, at high p_T ($\geqslant 4$ GeV/c) the dominant particle production mechanism is the hard scattering described by perturbative quantum chromodynamics (pQCD), which produces particles from the fragmentation of energetic partons. One of the most interesting observations at RHIC is that the yield of high p_T neutral pions and nonidentified charged hadrons in central Au+Au collisions at RHIC are below the expectation of the scaling with the number of nucleon-nucleon binary collisions, N_{coll} [12–14]. This effect could be a consequence of the energy loss suffered by partons moving through deconfined matter [15,16]. It has also been observed that the yield of neutral pions is more strongly suppressed than that for nonidentified charged hadrons [12] in central Au+Au collisions at RHIC. Another interesting feature is that the proton and antiproton yields in central events are comparable to that of pions at $p_T \approx 2$ GeV/c [6], differing from the expectation of pQCD. These observations suggest that a detailed study of particle composition at intermediate $p_T (\approx 2-4$ GeV/$c)$ is very important to understand hadron production and collision dynamics at RHIC.

The PHENIX experiment [17] has a unique hadron identification capability in a broad momentum range. Pions and kaons are identified up to 3 GeV/c and 2 GeV/c in p_T, respectively, and protons and antiprotons can be identified up to 4.5 GeV/c by using a high resolution time-of-flight detector [18]. Neutral pions are reconstructed via $\pi^0 \to \gamma\gamma$ up to $p_T \approx 10$ GeV/c through an invariant mass analysis of γ pairs detected in an electromagnetic calorimeter [19] with wide azimuthal coverage. During the measurements of Au+Au collisions at $\sqrt{s_{NN}}=200$ GeV in year 2001 at RHIC, the PHENIX experiment accumulated enough events to address the above issues at intermediate p_T as well as the particle production at low p_T with precise centrality dependences. In this paper, we present the centrality dependence of p_T spectra, $\langle p_T \rangle$, yields, and ratios for $\pi^{\pm}$, $K^{\pm}$, p, and $\bar{p}$, in Au+Au collisions at $\sqrt{s_{NN}}=200$ GeV at midrapidity measured by the PHENIX experiment. We also present results on the scaling behavior of charged hadrons compared with results of π^0 measurements [14], which have been published separately.

The paper is organized as follows. Section II describes the PHENIX detector used in this analysis. In Sec. III the analysis details including event selection, track selection, particle identification, and corrections applied to the data are described. The systematic errors on the measurements are also discussed in this section. For the experimental results, centrality dependence of p_T spectra for identified charged particles is presented in Sec. IV A, and transverse mass spectra are given in Sec. IV B. Particle yields and mean transverse momenta as a function of centrality are presented in Sec. IV C. In Sec. IV D the systematic study of particle ratios as a function p_T and centrality is presented. Section IV E studies the scaling behavior of identified charged hadrons. A summary is given in Sec. V.

II. PHENIX DETECTOR

The PHENIX experiment is composed of two central arms, two forward muon arms, and three global detectors. The east and west central arms are placed at zero rapidity and designed to detect electrons, photons, and charged hadrons. The north and south forward muon arms have full azimuthal coverage and are designed to detect muons. The global detectors measure the start time, vertex, and multiplicity of the interactions. The following sections describe the parts of the detector that are used in the present analysis. A detailed description of the complete detector can be found elsewhere [17–22].

A. Global detectors

In order to characterize the centrality of Au+Au collisions, zero-degree calorimeters (ZDCs) [21] and beam-beam counters (BBCs) [20] are employed. The zero-degree calorimeters are small hadronic calorimeters which measure the energy carried by spectator neutrons. They are placed 18 m upstream and downstream of the interaction point along the beam line. Each ZDC consists of three modules. Each module has a depth of two hadronic interaction lengths and is read out by a single photomultiplier tube (PMT). Both time and amplitude are digitized for each PMT along with the analog sum of the three PMT signals for each ZDC.

Two sets of beam-beam counters are placed 1.44 m from the nominal interaction point along the beam line (one on each side). Each counter consists of 64 Čerenkov telescopes, arranged radially around the beam line. The BBC measures the number of charged particles in the pseudorapidity region $3.0<|\eta|<3.9$. The correlation between BBC charge sum and ZDC total energy is used for centrality determination. The BBC also provides a collision vertex position and start time information for time-of-flight measurement.

B. Central arm detectors

Charged particles are tracked using the central arm spectrometers [22]. The spectrometer on the east side of the PHENIX detector (east arm) contains the following subsystems used in this analysis: drift chamber (DC), pad chamber (PC), and time-of-flight (TOF).

The drift chambers are the closest tracking detectors to the beam line—at a radial distance of 2.2 m. They measure charged particle trajectories in the azimuthal direction to determine the transverse momentum of each particle. By combining the polar angle information from the first layer of the PC with the transverse momentum, the total momentum p is determined. The momentum resolution is $\delta p/p \simeq 0.7\% \oplus 1.0\% \times p(\mathrm{GeV}/c)$, where the first term is due to the multiple scattering before the DC and the second term is the angular resolution of the DC. The momentum scale is known to 0.7%, from the reconstructed proton mass using the TOF.

The pad chambers are multiwire proportional chambers that form three separate layers of the central tracking system. The first pad chamber layer (PC1) is located at the radial outer edge of each drift chamber at a distance of 2.49 m, while the third layer (PC3) is 4.98 m from the interaction point. The second layer (PC2) is located at a radial distance of 4.19 m in the west arm only. PC1 and the DC, along with the vertex position measured by the BBC, are used in the global track reconstruction to determine the polar angle of each charged track.

The time-of-flight detector serves as the primary particle identification device for charged hadrons by measuring the stop time. The start time is given by the BBC. The TOF wall is located at a radial distance of 5.06 m from the interaction point in the east central arm. This contains 960 scintillator slats oriented along the azimuthal direction. It is designed to cover $|\eta|<0.35$ and $\Delta\phi=45°$ in azimuthal angle. The intrinsic timing resolution is $\sigma \simeq 115$ ps, which allows for a 3σ π/K separation up to $p_T \simeq 2.5$ GeV/c, and 3σ K/p separation up to $p_T \simeq 4$ GeV/c.

III. DATA ANALYSIS

In this section, we describe the event and track selection, charged particle identification and various corrections, including geometrical acceptance, particle decay, multiple scattering and absorption effects, detector occupancy corrections, and weak decay contributions from Λ and $\bar{\Lambda}$ to proton and antiproton spectra. The estimations of systematic uncertainties on the measurements are addressed at the end of this section.

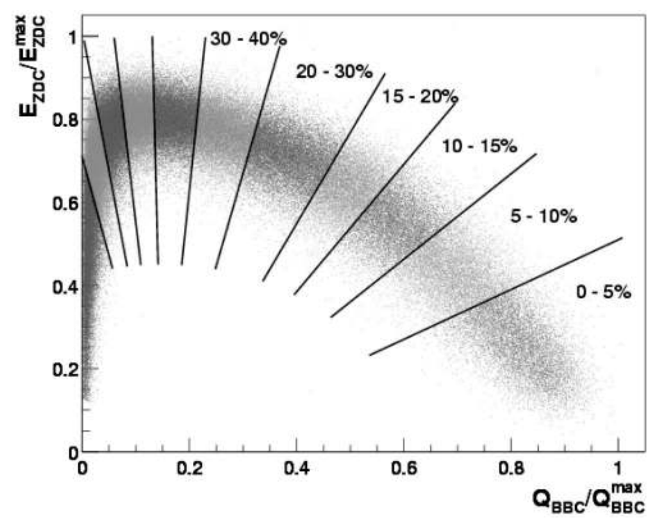

FIG. 1. BBC vs ZDC analog response. The lines represent the centrality cut boundaries.

A. Event selection

For the present analysis, we use the PHENIX minimum bias trigger events, which are determined by a coincidence between north and south BBC signals. We also require a collision vertex within ±30 cm from the center of the spectrometer. The collision vertex resolution determined by the BBC is about 6 mm in Au+Au collisions in minimum bias events [20]. The PHENIX minimum bias trigger events include $92.2^{+2.5}_{-3.0}\%$ of the 6.9 b Au+Au total inelastic cross section [14]. Figure 1 shows the correlation between the BBC charge sum and ZDC total energy for Au+Au at $\sqrt{s_{NN}}$ =200 GeV. The lines on the plot indicate the centrality definition in the analysis. For the centrality determination, these events are subdivided into 11 bins using the BBC and ZDC correlation: 0–5%, 5–10%, 10–15%, 15–20%, 20–30%, …, 70–80%, and 80–92%. Due to the statistical limitations in the peripheral events, we also use the 60–92% centrality bin as the most peripheral bin. After event selection, we analyze 2.02×10^7 minimum bias events, which represents ~140 times more events than used in our published Au+Au data at 130 GeV [6,8]. Based on a Glauber model calculation [8,14] we use two global quantities to characterize the event centrality: the average number of participants $\langle N_{part}\rangle$ and the average number of collisions $\langle N_{coll}\rangle$ associated with each centrality bin (Table I).

B. Track selection

Charged particle tracks are reconstructed by the DC based on a combinatorial Hough transform [25]—which gives the angle of the track in the main bend plane. The main bend

TABLE I. The average nuclear overlap function ($\langle T_{\mathrm{AuAu}}\rangle$), the number of nucleon-nucleon binary collisions ($\langle N_{coll}\rangle$), and the number of participant nucleons ($\langle N_{part}\rangle$) obtained from a Glauber Monte Carlo [8,14] correlated with the BBC and ZDC response for Au+Au at $\sqrt{s_{NN}}$=200 GeV as a function of centrality. Centrality is expressed as percentiles of σ_{AuAu}=6.9 b with 0% representing the most central collisions. The last line refers to minimum bias collisions.

Centrality	$\langle T_{\mathrm{AuAu}}\rangle$ (mb^{-1})	$\langle N_{coll}\rangle$	$\langle N_{part}\rangle$
0–5%	25.37±1.77	1065.4±105.3	351.4±2.9
0–10%	22.75±1.56	955.4±93.6	325.2±3.3
5–10%	20.13±1.36	845.4±82.1	299.0±3.8
10–15%	16.01±1.15	672.4±66.8	253.9±4.3
10–20%	14.35±1.00	602.6±59.3	234.6±4.7
15–20%	12.68±0.86	532.7±52.1	215.3±5.3
20–30%	8.90±0.72	373.8±39.6	166.6±5.4
30–40%	5.23±0.44	219.8±22.6	114.2±4.4
40–50%	2.86±0.28	120.3±13.7	74.4±3.8
50–60%	1.45±0.23	61.0±9.9	45.5±3.3
60–70%	0.68±0.18	28.5±7.6	25.7±3.8
60–80%	0.49±0.14	20.4±5.9	19.5±3.3
60–92%	0.35±0.10	14.5±4.0	14.5±2.5
70–80%	0.30±0.10	12.4±4.2	13.4±3.0
70–92%	0.20±0.06	8.3±2.4	9.5±1.9
80–92%	0.12±0.03	4.9±1.2	6.3±1.2
min. bias	6.14±0.45	257.8±25.4	109.1±4.1

plane is perpendicular to the beam axis (azimuthal direction). PC1 is used to measure the position of the hit in the longitudinal direction (along the beam axis). When combined with the location of the collision vertex along the beam axis (from the BBC), the PC1 hit gives the polar angle of the track. Only tracks with valid information from both the DC and PC1 are used in the analysis. In order to associate a track with a hit on the TOF, the track is projected to its expected hit location on the TOF. Tracks are required to have a hit on the TOF within $\pm 2\sigma$ of the expected hit location in both the azimuthal and beam directions. Finally, a cut on the energy loss in the TOF scintillator is applied to each track. This β-dependent energy loss cut is based on a parametrization of the Bethe-Bloch formula, i.e., $dE/dx \approx \beta^{-5/3}$, where $\beta = L/(ct_{\mathrm{TOF}})$, L is the path length of the track trajectory from the collision vertex to the hit position of the TOF wall, t_{TOF} is the time of flight, and c is the speed of light. The flight path length is calculated from a fit to the reconstructed track trajectory. The background due to random association of DC/PC1 tracks with TOF hits is reduced to a negligible level when the mass cut used for particle identification is applied (described in the following) section.

C. Particle identification

The charged particle identification (PID) is performed by using the combination of three measurements: time of flight from the BBC and TOF, momentum from the DC, and flight path length from the collision vertex point to the hit position on the TOF wall. The square of the mass is derived from the following formula:

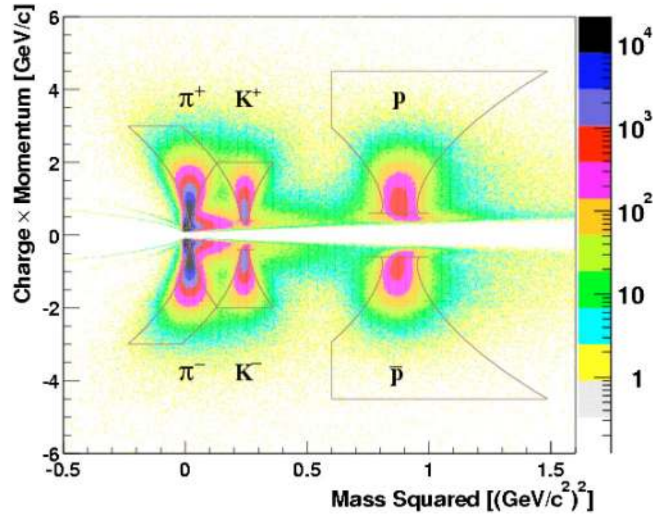

FIG. 2. (Color online) Mass-squared vs momentum multiplied by charge distribution in Au+Au collisions at $\sqrt{s_{NN}}$=200 GeV. The lines indicate the PID cut boundaries for pions, kaons, and protons (antiprotons) from left to right, respectively.

$$m^2 = \frac{p^2}{c^2}\left[\left(\frac{t_{\mathrm{TOF}}}{L/c}\right)^2 - 1\right], \tag{1}$$

where p is the momentum, t_{TOF} is the time of flight, L is a flight path length, and c is the speed of light. The charged particle identification is performed using cuts in m^2 and momentum space.

In Fig. 2, a plot of m^2 versus momentum multiplied by charge is shown together with applied PID cuts as solid curves. We use 2σ standard deviation PID cuts in m^2 and momentum space for each particle species. The PID cut is based on a parametrization of the measured m^2 width as a function of momentum,

$$\sigma_{m^2}^2 = \frac{\sigma_\alpha^2}{K_1^2}(4m^4p^2) + \frac{\sigma_{ms}^2}{K_1^2}\left[4m^4\left(1+\frac{m^2}{p^2}\right)\right] + \frac{\sigma_t^2c^2}{L^2}[4p^2(m^2+p^2)], \tag{2}$$

where σ_α is the angular resolution, σ_{ms} is the multiple scattering term, σ_t is the overall time-of-flight resolution, m is the centroid of m^2 distribution for each particle species, and K_1 is a magnetic field integral constant term of 87.0 mrad GeV. The parameters for PID are σ_α =0.835 mrad, σ_{ms}=0.86 mrad GeV, and σ_t=120 ps. Through improvements in alignment and calibrations, the momentum resolution is improved over the 130 GeV data [8]. The centrality dependence of the width and the mean position of the m^2 distribution has also been checked. There is no clear difference seen between central and peripheral collisions. For pion identification above 2 GeV/c, we apply an asymmetric PID cut to reduce kaon contamination of the pions. As shown by the lines in Fig. 2, the overlap region which is within the 2σ cuts for both pions and kaons is excluded. For kaons, the upper momentum cutoff is 2 GeV/c since the pion contamination level for kaons is $\approx$10% at that momentum. The upper momentum cutoff on the pions is p_T=3 GeV/c—where the kaon contamination reaches $\approx$10%. The contamination of protons by kaons reaches about 5% at 4 GeV/c. Electron (positron) and decay muon background at very low p_T (<0.3 GeV/c) are well separated from the pion mass-squared peak. The contamination background on each particle species is not subtracted in the analysis. For protons, the upper momentum cutoff is set at 4.5 GeV/c due to statistical limitations and background at high p_T. An additional cut on m^2 for protons and antiprotons, $m^2 > 0.6$ (GeV/c^2)^2, is introduced to reduce background. The lower momentum cutoffs are 0.2 GeV/c for pions, 0.4 GeV/c for kaons, and 0.6 GeV/c for p and $\bar{p}$. This cutoff value for p and $\bar{p}$ is larger than those for pions and kaons due to the large energy loss effect.

D. Acceptance, decay, and multiple scattering corrections

In order to correct for (1) the geometrical acceptance, (2) in-flight decay for pions and kaons, (3) the effect of multiple scattering, and (4) nuclear interactions with materials in the detector (including antiproton absorption), we use PISA (PHENIX Integrated Simulation Application), a GEANT [26] based Monte Carlo (MC) simulation program of the PHENIX detector. The single-particle tracks are passed from GEANT through the PHENIX event reconstruction software [25]. In this simulation, the BBC, TOF, and DC detector responses are tuned to match the real data. For example, dead areas of DC and TOF are included, and momentum and time-of-flight resolution are tuned. The track association to TOF in both azimuth (ϕ) and along the beam axis (z) as a function of momentum and the PID cut boundaries are parametrized to match the real data. A fiducial cut is applied to choose identical active areas on the TOF in both the simulation and data. We generate 1×10^7 single-particle events for each particle species ($\pi^\pm$, $K^\pm$, p, and $\bar{p}$) with low p_T enhanced (<2 GeV/c)+flat p_T distributions for high p_T (2–4 GeV/c for pions and kaons, 2–8 GeV/c for p and $\bar{p}$). [1] The efficiencies are determined in each p_T bin by dividing the reconstructed output by the generated input as expressed as follows:

$$\epsilon_{\rm acc}(j,p_T) = \frac{\text{No. of reconstructed MC tracks}}{\text{No. of generated MC tracks}}, \qquad (3)$$

where j is the particle species. The resulting correction factors ($1/\epsilon_{\rm acc}$) are applied to the data in each p_T bin and for each individual particle species.

[1]Due to the good momentum resolution at the high p_T region, the momentum smearing effect for a steeply falling spectrum is <1% at p_T=5 GeV/c. The flat p_T distribution up to 5 GeV/c can be used to obtain the correction factors.

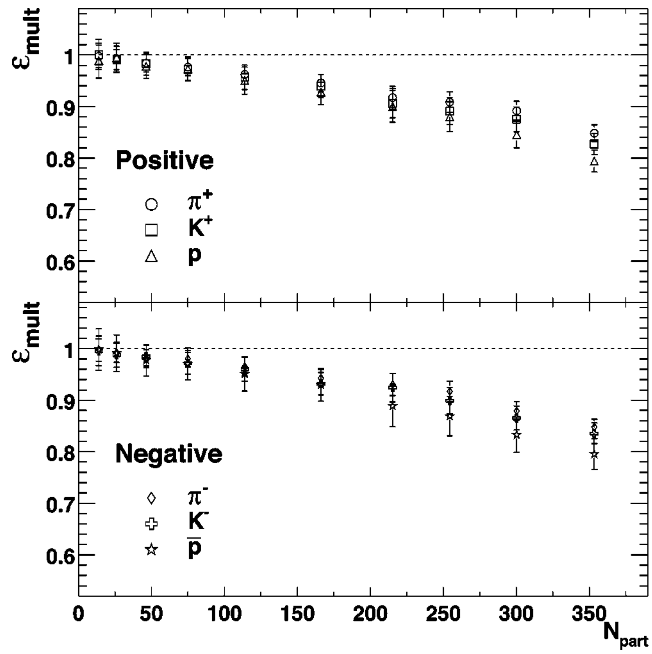

FIG. 3. Track reconstruction efficiency ($\epsilon_{\rm mult}$) as a function of centrality. The error bars on the plot represent the systematic errors.

E. Detector occupancy correction

Due to the high multiplicity environment in heavy ion collisions, which causes high occupancy and multiple hits on a detector cell such as scintillator slats of the TOF, it is expected that the track reconstruction efficiency in central events is lower than that in peripheral events. The typical occupancy at TOF is less than 10% in the most central Au+Au collisions. To correct for this effect, we merge single particle simulated events with real events and calculate the track reconstruction efficiency for each simulated track as follows:

$$\epsilon_{\rm mult}(i,j) = \frac{\text{No. of reconstructed embedded tracks}}{\text{No. of embedded tracks}}, \qquad (4)$$

where i is the centrality bins and j is the particle species. This study has been performed for each particle species and each centrality bin. The track reconstruction efficiencies are factorized (into independent terms depending on centrality and p_T) for $p_T > 0.4$ GeV/c, since there is no p_T dependence in the efficiencies above that p_T. Figure 3 shows the dependence of track reconstruction efficiency for $\pi^\pm$, $K^\pm$, p, and $\bar{p}$ as a function of centrality expressed as N_{part}. The efficiency in the most central 0–5% events is about 80% for protons ($\bar{p}$), 83% for kaons, and 85% for pions. Slower particles are more likely lost due to high occupancy in the TOF because the system responds to the earliest hit. For the most peripheral 80–92% events, the efficiency for detector occupancy effect is $\approx$99% for all particle species. The factors are applied to the spectra for each particle species and centrality bin. Systematic uncertainties on detector occupancy corrections ($1/\epsilon_{\rm mult}$) are less than 3%.

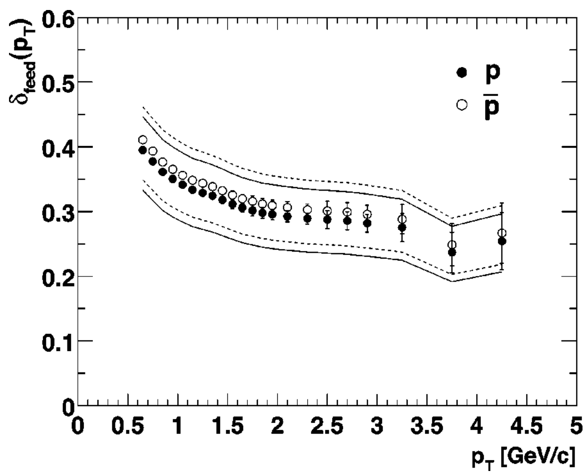

FIG. 4. The fractional contribution of protons ($\bar{p}$) from Λ ($\bar{\Lambda}$) decays in all measured protons ($\bar{p}$), $\delta_{\text{feed}}(p_T)$, as a function of p_T. The solid (dashed) lines represent the systematic errors for protons ($\bar{p}$). The error bars are statistical errors.

F. Weak decay correction

Protons and antiprotons from weak decays (e.g., from Λ and $\bar{\Lambda}$) can be reconstructed as tracks in the PHENIX spectrometer. The proton and antiproton spectra are corrected to remove the feed-down contribution from weak decays using a HIJING [27] simulation. HIJING output has been tuned to reproduce the measured particle ratios of Λ/p and $\bar{\Lambda}/\bar{p}$ along with their p_T dependencies in $\sqrt{s_{NN}}=130$ GeV Au+Au collisions [28] which include contribution from Ξ and Σ^0. Corrections for feed-down from $\Sigma^{\pm}$ are not applied, as these yields were not measured. About 2×10^6 central HIJING events (impact parameter $b=0-3$ fm) covering the TOF acceptance have been generated and processed through the PHENIX reconstruction software. To calculate the feed-down corrections, the $\bar{p}/p$ and $\bar{\Lambda}/\Lambda$ yield ratios were assumed to be independent of p_T and centrality. The systematic error due to the feed-down correction is estimated at 6% by varying the Λ/p and $\bar{\Lambda}/\bar{p}$ ratios within the systematic errors of the $\sqrt{s_{NN}}=130$ GeV Au+Au measurement [28] (±24%) and assuming m_T scaling at high p_T. This uncertainty could be larger if the Λ/p and $\bar{\Lambda}/\bar{p}$ ratios change significantly with p_T and beam energy. The fractional contribution to the p ($\bar{p}$) yield from Λ ($\bar{\Lambda}$), $\delta_{\text{feed}}(p_T)$, is shown in Fig. 4. The solid (dashed) lines represent the systematic errors for protons ($\bar{p}$). The obtained factor is about 40% below 1 GeV/c and 30% at 4 GeV/c. We multiply the proton and antiproton spectra by the factor C_{feed} for all centrality bins as a function of p_T:

$$C_{\text{feed}}(j,p_T) = 1 - \delta_{\text{feed}}(j,p_T), \tag{5}$$

where $j=p,\bar{p}$.

G. Invariant yield

Applying the data cuts and corrections discussed above, the final invariant yield for each particle species and centrality bin are derived using the following equation:

$$\frac{1}{2\pi p_T}\frac{d^2N}{dp_T dy} = \frac{1}{2\pi p_T}\frac{1}{N_{evt}(i)}C_{ij}(p_T)\frac{N_j(i,p_T)}{\Delta p_T \Delta y}, \tag{6}$$

where y is rapidity, $N_{evt}(i)$ is the number of events in each centrality bin $i, C_{ij}(p_T)$ is the total correction factor, and $N_j(i,p_T)$ is the number of counts in each centrality bin i, particle species j, and p_T. The total correction factor is composed of

$$C_{ij}(p_T) = \frac{1}{\epsilon_{\text{acc}}(j,p_T)}\frac{1}{\epsilon_{\text{mult}}(i,j)}C_{\text{feed}}(j,p_T). \tag{7}$$

H. Systematic uncertainties

To estimate systematic uncertainties on the p_T distribution and particle ratios, various sets of p_T spectra and particle ratios were made by changing the cut parameters including the fiducial cut, PID cut, and track association windows slightly from what was used in the analysis. For each of these spectra and ratios using modified cuts, the same changes in the cuts were made in the Monte Carlo analysis. The absolutely normalized spectra with different cut conditions are divided by the spectra with the baseline cut conditions, resulting in uncertainties associated with each cut condition as a function of p_T. The various uncertainties are added in quadrature. Three different centrality bins (minimum bias, central 0–5%, and peripheral 60–92%) are used to study the centrality dependence of systematic errors. The same procedure has been applied for the following particle ratios: π^-/π^+, K^-/K^+, $\bar{p}/p$, K/π, p/π^+, and $\bar{p}/\pi^-$.

TABLE II. Systematic errors on the p_T spectra for central events. All errors are given in percent.

	π^+	π^-	K^+	K^-	p		$\bar{p}$	
p_T range (GeV/c)	0.2–3.0	0.2–3.0	0.4–2.0	0.4–2.0	0.6–3.0	3.0–4.5	0.6–3.0	3.0–4.5
Cuts	6.2	6.2	11.2	9.5	6.6	11.6	6.6	11.6
Momentum scale	3	3	3	3	3	3	3	3
Occupancy correction	2	2	3	3	3	3	3	3
Feed-down correction					6.0	6.0	6.0	6.0
Total	7.2	7.2	12.0	10.4	9.9	13.7	9.9	9.9

TABLE III. Systematic errors on central-to-peripheral ratio (R_{CP}). All errors are given in percent.

Source	$(\pi^+ + \pi^-)/2$	$(K^+ + K^-)/2$	$(p+\bar{p})/2$
Occupancy correction (central)	2	3	3
Occupancy correction (peripheral)	2	3	3
$\langle T_{\mathrm{AuAu}}\rangle$ (0–10%)	6.9	6.9	6.9
$\langle T_{\mathrm{AuAu}}\rangle$ (60–92%)	28.6	28.6	28.6
Total	29.5	29.7	29.7

Table II shows the systematic errors of the p_T spectra for central collisions. The systematic uncertainty on the absolute value of momentum (momentum scale) is estimated as 3% in the measured p_T range by comparing the known proton mass to the value measured as protons in real data. It is found that the total systematic error on the p_T spectra is 8–14% in both central and peripheral collisions. For the particle ratios, the typical systematic error is about 6% for all particle species. The dominant source of uncertainties on the central-to-peripheral ratio scaled by N_{coll} (R_{CP}) are the systematic errors on the nuclear overlap function, T_{AuAu} (see Table III). The systematic errors on dN/dy and $\langle p_T\rangle$ are discussed in Sec. IV C together with the procedure for the determination of these quantities.

IV. RESULTS

In this section, the p_T and transverse mass spectra and yields of identified charged hadrons as a function of centrality are shown. Also a systematic study of particle ratios in Au+Au collisions at $\sqrt{s_{NN}}$=200 GeV at midrapidity is presented.

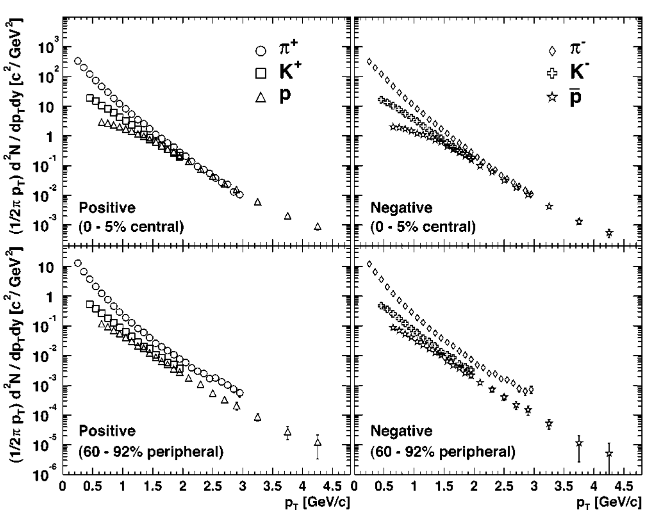

FIG. 5. Transverse momentum distributions for pions, kaons, protons, and antiprotons in Au+Au collisions at $\sqrt{s_{NN}}$=200 GeV. The top two figures show p_T spectra for the most central 0–5% collisions. The bottom two are for the most peripheral 60–92% collisions. The error bars are statistical only. The Λ ($\bar{\Lambda}$) feed-down corrections for protons (antiprotons) have been applied.

A. Transverse momentum distributions

Figure 5 shows the p_T distributions for pions, kaons, protons, and antiprotons. The top two plots are for the most central 0–5% collisions, and the bottom two are for the most peripheral 60–92% collisions. The spectra for positive particles are presented on the left, and those for negative particles on the right. For p_T<1.5 GeV/c in central events, the data show a clear mass dependence in the shapes of the spectra. The p and $\bar{p}$ spectra have a shoulder-arm shape, the pion spectra have a concave shape, and the kaons fall exponentially. On the other hand, in the peripheral events, the mass dependences of the p_T spectra are less pronounced and the p_T spectra are more nearly parallel to each other. Another notable observation is that at p_T above ≈2.0 GeV/c in central events, the p and $\bar{p}$ yields become comparable to the pion yields, which is also observed in 130 GeV Au+Au collisions [6]. This observation shows that a significant fraction of the total particle yield at p_T≈2.0–4.5 GeV/c in Au+Au central collisions consists of p and $\bar{p}$.

These high statistics Au+Au data at $\sqrt{s_{NN}}$=200 GeV allow us to perform a detailed study of the centrality dependence of the p_T spectra. In this analysis, we use the 11 centrality bins described in Sec. III A as well as the combined peripheral bin (60–92%) for each particle species. Figure 6 shows the centrality dependence of the p_T spectrum for π^+ (left) and π^- (right). For clarity, the data points are scaled

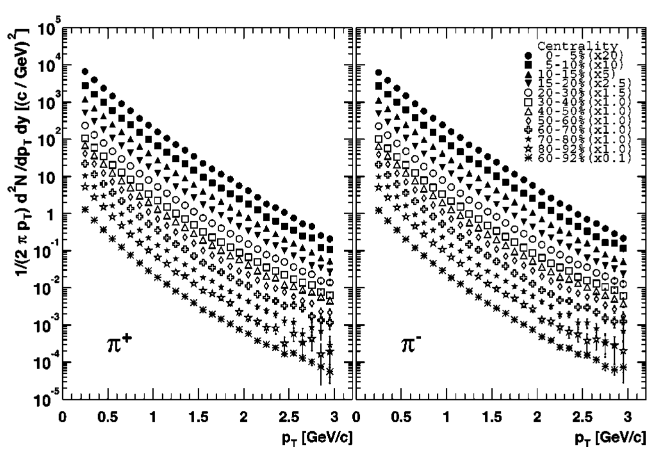

FIG. 6. Centrality dependence of the p_T distribution for π^+ (left) and π^- (right) in Au+Au collisions at $\sqrt{s_{NN}}$=200 GeV. The different symbols correspond to different centrality bins. The error bars are statistical only. For clarity, the data points are scaled vertically as quoted in the figure.

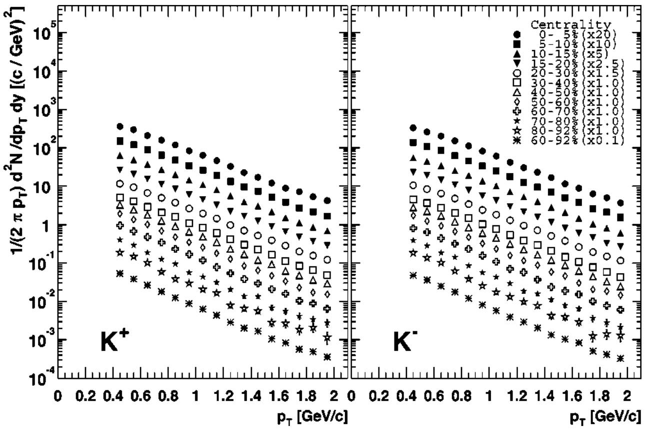

FIG. 7. Centrality dependence of the p_T distribution for K^+ (left) and K^- (right) in Au+Au collisions at $\sqrt{s_{NN}}$=200 GeV. The different symbols correspond to different centrality bins. The error bars are statistical only. For clarity, the data points are scaled vertically as quoted in the figure.

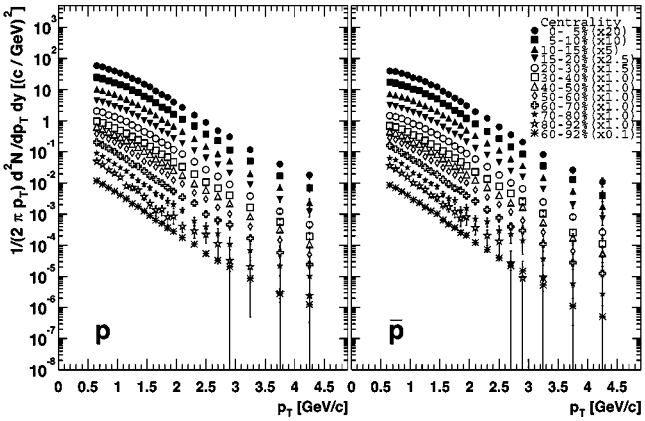

FIG. 8. Centrality dependence of the p_T distribution for protons (left) and antiprotons (right) in Au+Au collisions at $\sqrt{s_{NN}}$ =200 GeV. The different symbols correspond to different centrality bins. The error bars are statistical only. Feed-down corrections for Λ ($\bar{\Lambda}$) decaying into proton ($\bar{p}$) have been applied. For clarity, the data points are scaled vertically as quoted in the figure.

vertically as quoted in the figures. The error bars are statistical only. The pion spectra show an approximately power-law shape for all centrality bins. The spectra become steeper (fall faster with increasing p_T) for more peripheral collisions.

Figure 7 shows similar plots for kaons. The data can be well approximated by an exponential function in p_T for all centralities. Finally, the centrality dependence of the p_T spectra for protons (left) and antiprotons (right) is shown in Fig. 8. As in Fig. 5, both p and $\bar{p}$ spectra show a strong centrality dependence below 1.5 GeV/c, i.e., they develop a shoulder at low p_T and the spectra flatten (fall more slowly with increasing p_T) with increasing collision centrality.

Up to p_T=1.5–2 GeV/c, it has been found that hydrodynamic models can reproduce the data well for $\pi^{\pm}$, $K^{\pm}$, p, and $\bar{p}$ spectra at 130 GeV [8], and also the preliminary data at 200 GeV in Au+Au collisions (e.g., Refs. [5,29]). These models assume thermal equilibrium and that the created particles are affected by a common transverse flow velocity β_T and freeze-out (stop interacting) at a temperature T_{fo} with a fixed initial condition governed by the equation of state (EOS) of matter. There are several types of hydrodynamic calculations, e.g., (1) a conventional hydrodynamic fit to the experimental data with two free parameters, β_T and T_{fo} [30], (2) a combination of hydrodynamics and a hadronic cascade model [5], (3) transverse and longitudinal flow with simultaneous chemical and thermal freeze-outs within the statistical thermal model [31], (4) requiring the early thermalization with a QGP type EOS [32]. Despite the differences between the hydrodynamic models, all models are in qualitative agreement with the identified single-particle spectra in central collisions at low p_T as seen in Ref. [8]. However, they fail to reproduce the peripheral spectra above $p_T \simeq 1$ GeV/c and their applicability in the high p_T region (>2 GeV/c) is limited. Comparison with the detailed centrality dependence of hadron spectra presented here would shed light on further understanding of the EOS, chemical properties in the model, and the freeze-out conditions at RHIC.

B. Transverse mass distributions

In order to quantify the observed particle mass dependence of the p_T spectra shape and their centrality dependence, the transverse mass spectra for identified charged hadrons are presented here. From former studies at lower beam energies, it is known that the invariant differential cross sections in $p+p$, $p+A$, and $A+A$ collisions generally show a shape of an exponential in $m_T - m_0$, where m_0 is particle mass, and $m_T = \sqrt{p_T^2 + m_0^2}$ is transverse mass. For an m_T spectrum with an exponential shape, one can parametrize it as follows:

$$\frac{d^2N}{2\pi m_T dm_T dy} = \frac{1}{2\pi T(T+m_0)} A \exp\left(-\frac{m_T - m_0}{T}\right), \quad (8)$$

where T is referred to as the inverse slope parameter, and A is a normalization parameter which contains information on dN/dy. In Fig. 9, m_T distributions for $\pi^{\pm}$, $K^{\pm}$, p, and $\bar{p}$ for central 0–5% (top panels), midcentral 40–50% (middle panels), and peripheral 60–92% (bottom panels) collisions are shown. The spectra for positive particles are on the left and for negative particles are on the right. The solid lines overlaid on each spectra are the fit results using Eq. (8). The error bars are statistical only. As seen in Fig. 9, all the m_T spectra display an exponential shape in the low m_T region. However, at higher m_T, the spectra become less steep, which corresponds to a power-law behavior in p_T. Thus, the inverse slope parameter in Eq. (8) depends on the fitting range. In this analysis, the fits cover the range 0.2–1.0 GeV/c^2 for pions and 0.1–1.0 GeV/c^2 for kaons, protons, and antiprotons in $m_T - m_0$. The low m_T region ($m_T - m_0 < 0.2$ GeV/c^2) for pions is excluded from the fit to eliminate the contributions from resonance decays. The inverse slope parameters for each particle species in the three centrality bins are summarized in Fig. 10 and in Table IV. The inverse slope parameters increase with increasing particle mass in all centrality bins. This

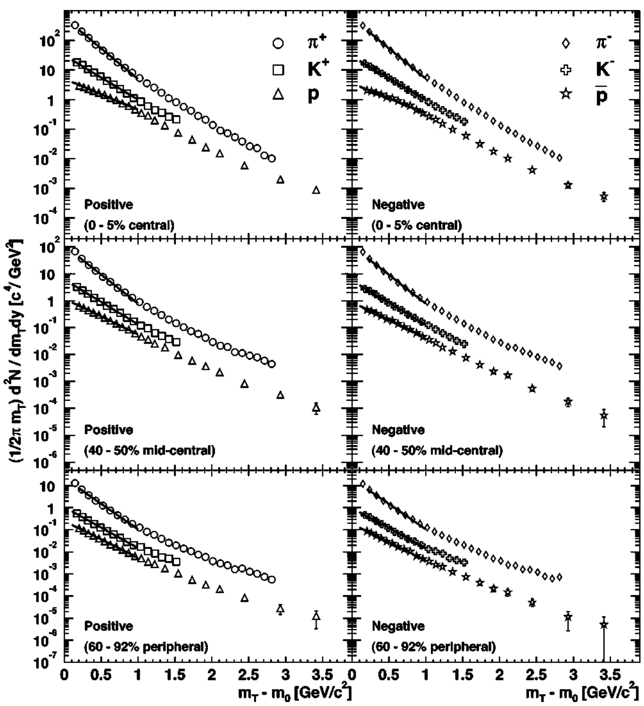

FIG. 9. Transverse mass distributions for $\pi^{\pm}$, $K^{\pm}$, protons, and antiprotons for central 0–5% (top panels), midcentral 40–50% (middle panels), and peripheral 60–92% (bottom panels) in Au+Au collisions at $\sqrt{s_{NN}}$=200 GeV. The lines on each spectra are the fitted results using m_T exponential function. The fit ranges are 0.2–1.0 GeV/c^2 for pions and 0.1–1.0 GeV/c^2 for kaons, protons, and antiprotons in m_T-m_0. The error bars are statistical errors only.

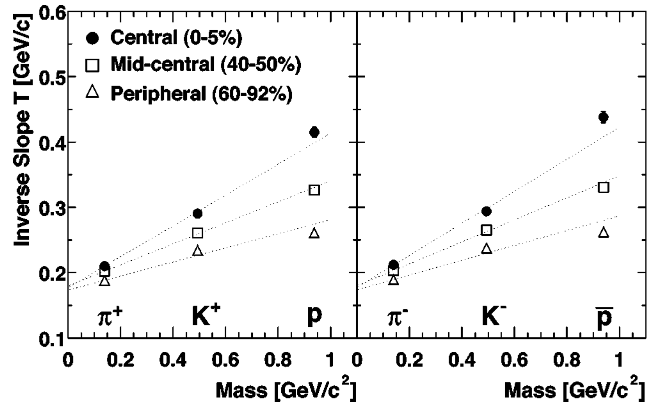

FIG. 10. Mass and centrality dependence of inverse slope parameters T in m_T spectra for positive (left) and negative (right) particles in Au+Au collisions at $\sqrt{s_{NN}}$=200 GeV. The fit ranges are 0.2–1.0 GeV/c^2 for pions and 0.1–1.0 GeV/c^2 for kaons, protons, and antiprotons in m_T-m_0. The dotted lines represent a linear fit of the results from each centrality bin as a function of mass using Eq. (9).

increase for central collisions is more rapid for heavier particles.

Such a behavior was derived, under certain conditions, by Schnedermann *et al.* [33] for central collisions and by Csörgő *et al.* [34] for noncentral heavy-ion collisions:

$$T = T_0 + m\langle u_t\rangle^2. \tag{9}$$

Here T_0 is a freeze-out temperature and $\langle u_t\rangle$ is a measure of the strength of the (average radial) transverse flow. The dotted lines in Fig. 10 represent a linear fit of the results from each centrality bin as a function of mass using Eq. (9). The fit parameters for positive and negative particles are shown in Table IV. It indicates, that the linear extrapolation of the slope parameter $T(m)$ to zero mass has the same intercept parameters T_0 in all the centrality classes, indicating that the freeze-out temperature is approximately independent of the centrality. On the other hand, $\langle u_t\rangle$, the strength of the average transverse flow is increasing with increasing centrality, supporting the hydrodynamic picture.

Motivated by the idea of a color glass condensate, the authors of Ref. [35] argued that the m_T spectra (not m_T-m_0) of identified hadrons at RHIC energy follow a generalized scaling law for all centrality classes when the proton (kaon) spectrum is multiplied by a factor of 0.5 (2.0). The 200 GeV Au+Au pion and kaon spectra seem to follow this m_T scaling, but proton and antiproton spectra are below it by a factor of ~2 for all centralities. Since p and $\bar{p}$ spectra presented here are corrected for weak decays from Λ and $\bar{\Lambda}$, the model also needs to study the feed-down effect to conclude that a universal m_T scaling law is seen at RHIC.

C. Mean transverse momentum and particle yields versus N_{part}

By integrating a measured p_T spectrum over p_T, one can determine the mean transverse momentum $\langle p_T\rangle$ and particle yield per unit rapidity, dN/dy, for each particle species. The procedure to determine the mean p_T and dN/dy is described below.

TABLE IV. (Top) Inverse slope parameters for π, K, p, and $\bar{p}$ for the 0–5%, 40–50%, and 60–92% centrality bins, in units of MeV/c^2. The errors are statistical only. (Bottom) The extracted fit parameters of the freeze-out temperature T_0 in units of MeV/c^2 and the measure of the strength of the average radial transverse flow ($\langle u_t\rangle$) using Eq. (9). The fit results shown here are for positive and negative particles, as denoted in the superscripts, and for three different centrality bins.

Particle	0–5%	40–50%	60–92%
π^+	210.2±0.8	201.9±0.8	187.8±0.7
π^-	211.9±0.7	203.0±0.7	189.2±0.7
K^+	290.2±2.2	260.6±2.4	233.9±2.6
K^-	293.8±2.2	265.1±2.3	237.4±2.6
p	414.8±7.5	326.3±5.9	260.7±5.4
$\bar{p}$	437.9±8.5	330.5±6.4	262.1±5.9
Fit parameter	0–5%	40–50%	60–92%
$T_0^{(+)}$	177.0±1.2	179.5±1.2	173.1±1.2
$T_0^{(-)}$	177.3±1.2	179.6±1.2	173.7±1.1
$\langle u_t\rangle^{(+)}$	0.48±0.07	0.40±0.07	0.32±0.07
$\langle u_t\rangle^{(-)}$	0.49±0.07	0.41±0.07	0.33±0.07

TABLE V. Systematic errors on dN/dy for central 0–5% (top) and peripheral 60–92% (bottom) collisions. All errors are given in percent.

Source	π^+	π^-	K^+	K^-	p	$\bar{p}$
			Central 0–5%			
Cuts+occupancy	6.5	6.5	11.6	10.0	7.2	7.2
Extrapolation	5.4	4.8	5.7	5.6	9.6	9.2
Contamination background	<1	<1	<1	<1	<1	<1
Feed-down					8.0	8.0
Total	8.4	8.0	12.9	11.4	14.4	14.4
			Peripheral 60–92%			
Cuts+occupancy	6.5	6.5	8.3	7.2	8.3	8.3
Extrapolation	8.4	8.0	7.4	7.5	13.6	13.6
Contamination background	<1	<1	<1	<1	<1	<1
Feed-down					8.0	8.0
Total	10.6	10.3	11.1	10.3	17.8	17.8

(1) Determine dN/dy and $\langle p_T \rangle$ by integrating over the measured p_T range from the data.

(2) Fit several appropriate functional forms (detailed below) to the p_T spectra. Note that all of the fits are reasonable approximations to the data. Integrate from zero to the first data point and from the last data point to infinity.

(3) Sum the data yield and the two functional yield pieces together to get dN/dy and $\langle p_T \rangle$ in each functional form.

(4) Take the average between the upper and lower bounds from the different functional forms to obtain the final dN/dy and $\langle p_T \rangle$. The statistical uncertainties are determined from the data. The systematic errors from the extrapolation of yield are defined as half of the difference between the upper and lower bounds.

(5) Determine the final systematic errors on dN/dy and $\langle p_T \rangle$ for each centrality bin by taking the quadrature sum of the extrapolation errors, errors associated with cuts, detector occupancy corrections (for dN/dy), and feed-down corrections (for p and $\bar{p}$).

For the extrapolation of dN/dy and $\langle p_T \rangle$, the following functional forms are used for different particle species: a power-law function and a p_T exponential for pions, a p_T exponential and an m_T exponential for kaons, and a Boltzmann function, p_T exponential, and m_T exponential for protons and antiprotons. The effects of contamination background at high-p_T region for both dN/dy and $\langle p_T \rangle$ are estimated as less than 1% for all particle species. The overall systematic uncertainties on both dN/dy and $\langle p_T \rangle$ are about 10–15%. See Table V for the systematic errors of dN/dy and Table VI for those of $\langle p_T \rangle$.

In Fig. 11, the centrality dependence of $\langle p_T \rangle$ for $\pi^\pm$, $K^\pm$, p, and $\bar{p}$ is shown. The error bars in the figure represent the

TABLE VI. Systematic errors on $\langle p_T \rangle$ for central 0–5 % (top) and peripheral 60–92% (bottom) collisions. All errors are given in percent.

Source	π^+	π^-	K^+	K^-	p	$\bar{p}$
			Central 0–5%			
Cuts	6.2	6.2	11.2	9.5	6.6	6.6
Extrapolation	3.9	3.5	3.5	3.3	6.2	5.9
Contamination background	<1	<1	<1	<1	<1	<1
Feed-down					1.0	1.0
Total	7.3	7.1	13.5	10.0	9.1	8.9
			Peripheral 60–92%			
Cuts	6.2	6.2	7.7	6.6	7.7	7.7
Extrapolation	5.4	5.3	4.6	4.4	8.6	8.6
Contamination background	<1	<1	<1	<1	<1	<1
Feed-down					1.0	1.0
Total	8.2	8.1	8.9	7.9	11.5	11.5

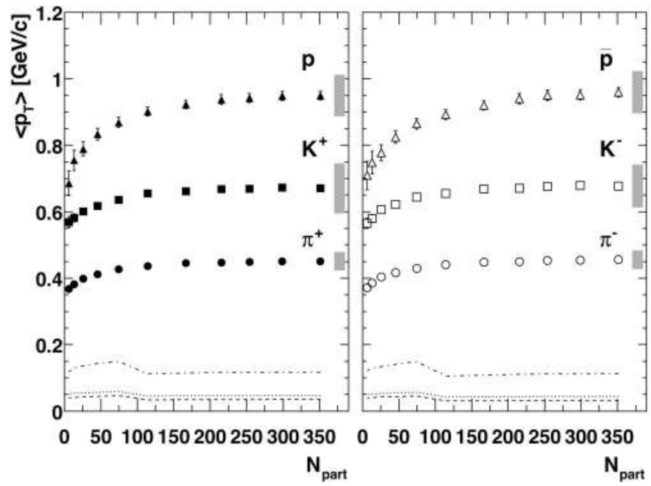

FIG. 11. Mean transverse momentum as a function of N_{part} for pions, kaons, protons, and antiprotons in Au+Au collisions at $\sqrt{s_{NN}}$=200 GeV. The left (right) panel shows the $\langle p_T\rangle$ for positive (negative) particles. The error bars are statistical errors. The systematic errors from cut conditions are shown as shaded boxes on the right for each particle species. The systematic errors from extrapolations, which are scaled by a factor of 2 for clarity, are shown in the bottom for protons and antiprotons (dashed-dot lines), kaons (dotted lines), and pions (dashed lines).

statistical errors. The systematic errors from cut conditions are shown as shaded boxes on the right for each particle species. The systematic errors from extrapolations, which are scaled by a factor of 2 for clarity, are shown in the bottom for each particle species. The data are also summarized in Table VII. It is found that $\langle p_T\rangle$ for all particle species increases from the most peripheral to midcentral collisions, and appears to saturate from the midcentral to central collisions (although the $\langle p_T\rangle$ values for p and $\bar{p}$ may continue to rise). It should be noted that while the total systematic errors on $\langle p_T\rangle$ listed in Table VI is large, the trend shown in the figure is significant. One of the main sources of the uncertainty is the yield extrapolation in unmeasured p_T range (e.g., $p_T<0.6$ GeV/c for protons and antiprotons). These system-

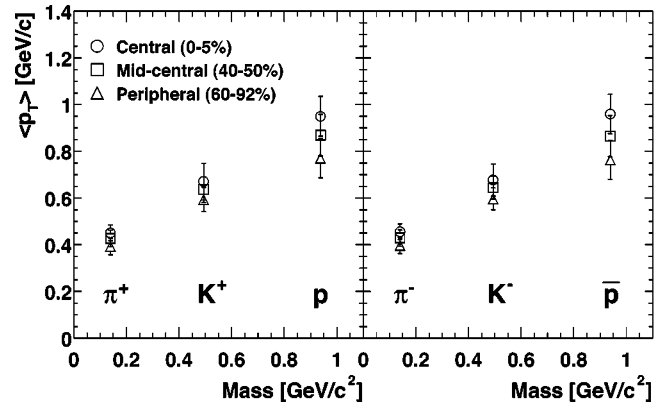

FIG. 12. Mean transverse momentum versus particle mass for central 0–5%, midcentral 40–50%, and peripheral 60–92% in Au+Au collisions at $\sqrt{s_{NN}}$=200 GeV. The left (right) panel shows the $\langle p_T\rangle$ for positive (negative) particles. The error bars represent the total systematic errors. The statistical errors are negligible.

atic errors are correlated, and therefore move the curve up and down simultaneously. In Fig. 12, the particle mass and centrality dependence of $\langle p_T\rangle$ are shown. The data presented here are the $\langle p_T\rangle$ for the 0–5%, 40–50% and 60–92% centrality bins. Figure 12 is similar to Fig. 10, which shows the inverse slope parameters, in that the $\langle p_T\rangle$ increases with particle mass and with centrality. This is qualitatively consistent with the hydrodynamic expansion picture [29,33,34].

Figure 13 shows the centrality dependence of dN/dy per participant pair (0.5 N_{part}). The data are summarized in Table VIII. The error bars on each point represent the quadratic sum of the statistical errors and systematic errors from cut conditions. The statistical errors are negligible. The lines represent the effect of the systematic error on N_{part} which affects all curves in the same way. The data indicate that dN/dy per participant pair increases for all particle species with N_{part} up to ≈100, and saturates from the midcentral to the most central collisions. From dN/dy for protons and antiprotons, we obtain the net proton number at midrapidity for the most central 0–5% collisions, $dN/dy|_p - dN/dy|_{\bar{p}}$=18.47−13.52

TABLE VII. Centrality dependence of $\langle p_T\rangle$ for $\pi^\pm$, $K^\pm$, p, and $\bar{p}$ in MeV/c. The errors are systematic only. The statistical errors are negligible.

N_{part}	π^+	π^-	K^+	K^-	p	$\bar{p}$
351.4	451±33	455±32	670±78	677±68	949±85	959±84
299.0	450±33	454±33	672±78	679±68	948±84	951±83
253.9	448±33	453±33	668±78	676±68	942±84	950±83
215.3	447±34	449±33	667±78	670±67	937±84	940±83
166.6	444±35	447±34	661±77	668±67	923±85	920±83
114.2	436±35	440±35	655±77	654±66	901±83	892±82
74.4	426±35	429±35	636±54	644±48	868±88	864±88
45.5	412±35	416±34	617±53	621±47	833±86	824±86
25.7	398±34	403±33	600±52	606±46	788±84	777±83
13.4	381±32	385±32	581±51	579±46	755±82	747±80
6.3	367±30	371±30	568±51	565±45	685±78	708±81

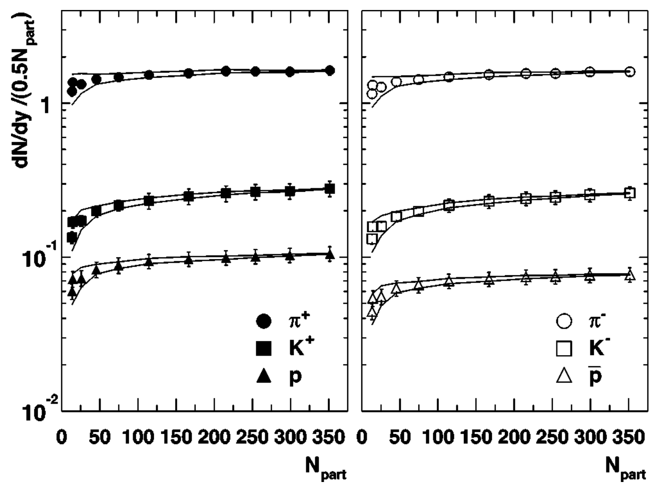

FIG. 13. Particle yield per unit rapidity (dN/dy) per participant pair ($0.5N_{part}$) as a function of N_{part} for pions, kaons, protons, and antiprotons in Au+Au collisions at $\sqrt{s_{NN}}$=200 GeV. The left (right) panel shows the dN/dy for positive (negative) particles. The error bars represent the quadratic sum of statistical errors and systematic errors from cut conditions. The lines represent the effect of the systematic error on N_{part} which affects all curves in the same way.

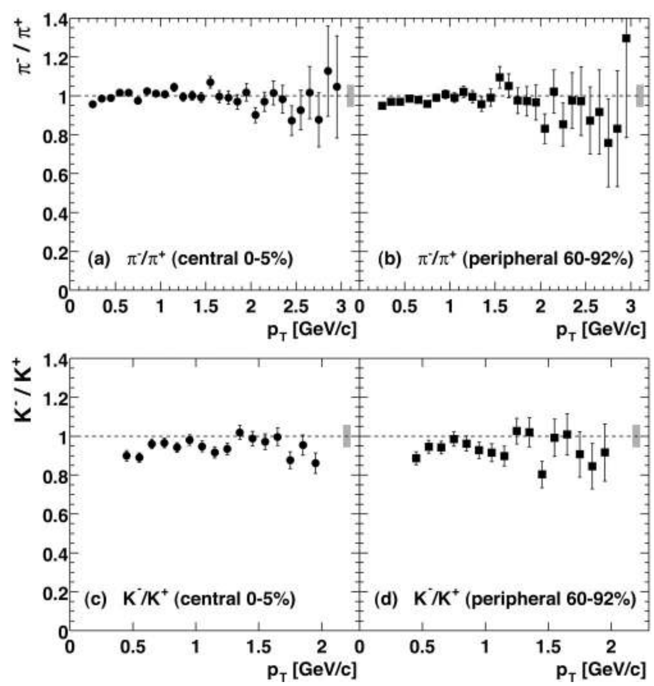

FIG. 14. Particle ratios of (a) π^-/π^+ for central 0–5%, (b) π^-/π^+ for peripheral 60–92%, (c) K^-/K^+ for central 0–5%, and (d) K^-/K^+ for peripheral 60–92% in Au+Au collisions at $\sqrt{s_{NN}}$ =200 GeV. The error bars indicate the statistical errors and shaded boxes around unity on each panel indicate the systematic errors.

=4.95±2.74, which is consistent with the preliminary result at 200 GeV Au+Au (midrapidity) reported by the BRAHMS Collaboration [36].

D. Particle ratios

The ratios of π^-/π^+, K^-/K^+, $p/\bar{p}$, K/π, p/π, and $\bar{p}/\pi$ measured as a function of p_T and centrality at $\sqrt{s_{NN}}$ =200 GeV in Au+Au collisions are presented here.

1. Particle Ratios versus p_T

Figure 14 shows the particle ratios of (a) π^-/π^+ for central 0–5%, (b) π^-/π^+ for peripheral 60–92%, (c) K^-/K^+ for central 0–5%, and (d) K^-/K^+ for peripheral 60–92%. Similar plots for the $\bar{p}/p$ ratios are shown in Fig. 15. The error bars represent statistical errors and the shaded boxes on each panel represent the systematic errors. For each of these particle species and centralities, the particle ratios are constant within the experimental errors over the measured p_T range. Similar centrality and p_T dependences are observed in 130 GeV Au+Au data [8,37–42] and previously published 200 GeV Au+Au data [43,44].

To investigate the p_T dependence of the $\bar{p}/p$ ratio in detail, it is shown in Fig. 16 for minimum bias events with two theoretical calculations: a pQCD calculation (dashed line) and a baryon junction model with jet-quenching [46] (solid line). The baryon junction calculation agrees well with the measured $\bar{p}/p$ ratio over the measured p_T range within the experimental uncertainties, while the pQCD calculation does not explain the constant $\bar{p}/p$ ratio over the wide p_T range.

TABLE VIII. Centrality dependence of dN/dy for $\pi^\pm$, $K^\pm$, p, and $\bar{p}$. The errors are systematic only. The statistical errors are negligible.

N_{part}	π^+	π^-	K^+	K^-	p	$\bar{p}$
351.4	286.4±24.2	281.8±22.8	48.9±6.3	45.7±5.2	18.4±2.6	13.5±1.8
299.0	239.6±20.5	238.9±19.8	40.1±5.1	37.8±4.3	15.3±2.1	11.4±1.5
253.9	204.6±18.0	198.2±16.7	33.7±4.3	31.1±3.5	12.8±1.8	9.5±1.3
215.3	173.8±15.6	167.4±14.4	27.9±3.6	25.8±2.9	10.6±1.5	7.9±1.1
166.6	130.3±12.4	127.3±11.6	20.6±2.6	19.1±2.2	8.1±1.1	5.9±0.8
114.2	87.0±8.6	84.4±8.0	13.2±1.7	12.3±1.4	5.3±0.7	3.9±0.5
74.4	54.9±5.6	52.9±5.2	8.0±0.8	7.4±0.6	3.2±0.5	2.4±0.3
45.5	32.4±3.4	31.3±3.1	4.5±0.4	4.1±0.4	1.8±0.3	1.4±0.2
25.7	17.0±1.8	16.3±1.6	2.2±0.2	2.0±0.1	0.93±0.15	0.71±0.12
13.4	7.9±0.8	7.7±0.7	0.89±0.09	0.88±0.09	0.40±0.07	0.29±0.05
6.3	4.0±0.4	3.9±0.3	0.44±0.04	0.42±0.04	0.21±0.04	0.15±0.02

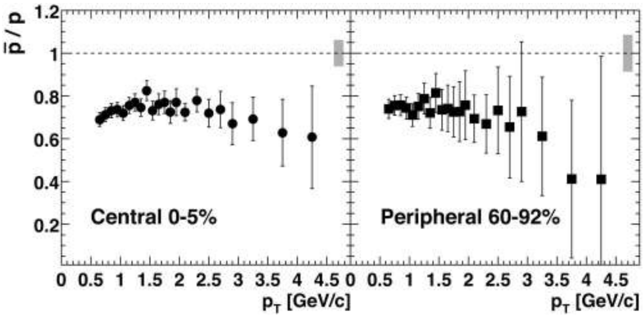

FIG. 15. Ratio of $\bar{p}/p$ as a function of p_T for central 0–5% (left) and peripheral 60–92% (right) in Au+Au collisions at $\sqrt{s_{NN}}$ =200 GeV. The error bars indicate the statistical errors and shaded boxes around unity on each panel indicate the systematic errors.

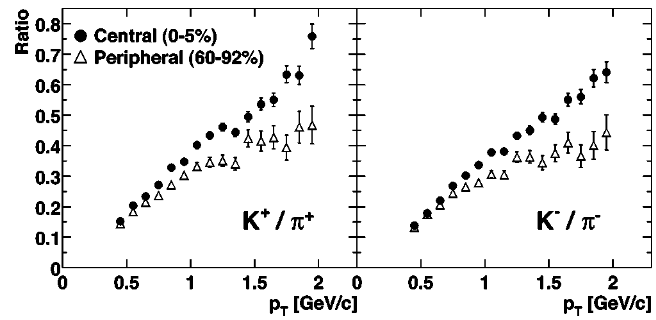

FIG. 17. K/π ratios as a function of p_T for central 0–5% and peripheral 60–92% in Au+Au collisions at $\sqrt{s_{NN}}$=200 GeV. The left is for K^+/π^+ and the right is for K^-/π^-. The error bars indicate the statistical errors.

The statistical thermal model (discussed in more detail later in this section) predicted [10] a baryon chemical potential of μ_B=29 MeV and a freeze-out temperature of T_{ch} =177 MeV for central Au+Au collisions at 200 GeV. From these, the expected $\bar{p}/p$ ratio is $e^{-2\mu_B/T_{ch}}$=0.72, which agrees with our data (0.73). The parton recombination model [45] also reproduces the $\bar{p}/p$ ratio and its flat p_T dependence. The $\bar{p}/p$ ratio in this model is 0.72 since the statistical thermal model is used.

In Fig. 17, the p_T dependence of the K/π ratio is shown for the most central 0–5% and the most peripheral 60–92% centrality bins. The K^+/π^+ (K^-/π^-) ratios are shown on the left (right). Both ratios increase with p_T and the increase is faster in central collisions than in peripheral ones.

In Fig. 18, the p/π and $\bar{p}/\pi$ ratios are shown as a function of p_T for the 0–10%, 20–30% and 60–92% centrality bins. In this figure, the results of p/π^0 and $\bar{p}/\pi^0$ [14] are presented above 1.5 GeV/c and overlaid on the results of p/π^+ and $\bar{p}/\pi^-$, respectively. The absolutely normalized p_T spectra of

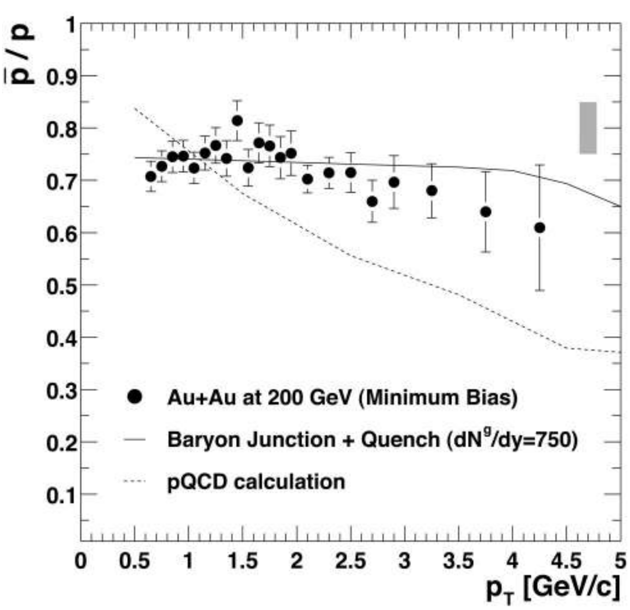

FIG. 16. $\bar{p}/p$ ratios as a function of p_T for minimum bias events in Au+Au at $\sqrt{s_{NN}}$=200 GeV. The error bars indicate the statistical errors and shaded box on the right indicates the systematic errors. Two theoretical calculations are shown: baryon junction model (solid line) and pQCD calculation (dashed line) taken from Ref. [46].

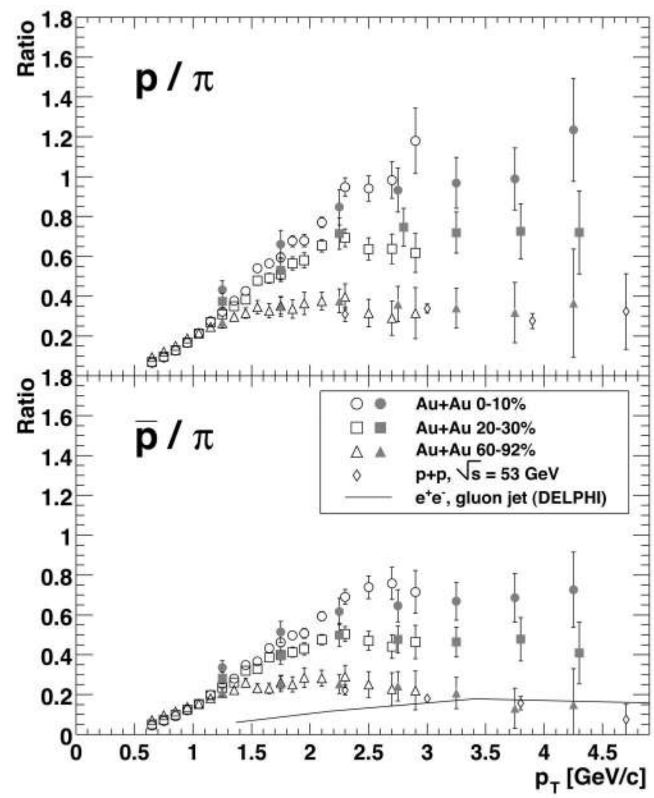

FIG. 18. Proton/pion (top) and antiproton/pion (bottom) ratios for central 0–10%, midcentral 20–30%, and peripheral 60–92% in Au+Au collisions at $\sqrt{s_{NN}}$=200 GeV. Open (filled) points are for charged (neutral) pions. The data at $\sqrt{s}$=53 GeV $p+p$ collisions [47] are also shown. The solid line is the $(\bar{p}+p)/(\pi^++\pi^-)$ ratio measured in gluon jets [48].

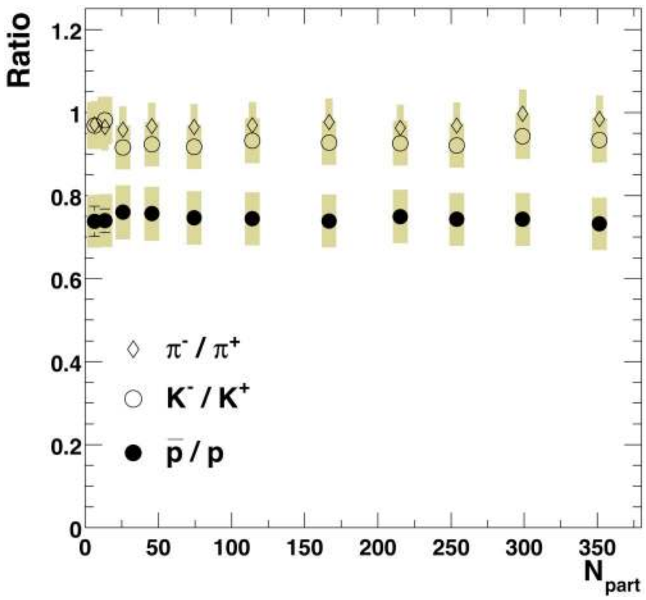

FIG. 19. (Color online) Centrality dependence of particle ratios for π^-/π^+,K^-/K^+, and $\bar{p}/p$ in Au+Au collisions at $\sqrt{s_{NN}}$ =200 GeV. The error bars indicate the statistical errors. The shaded boxes on each data point are the systematic errors.

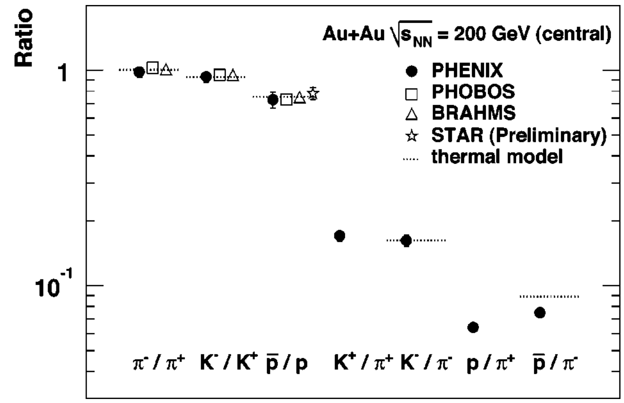

FIG. 20. Comparison of PHENIX particle ratios with those of PHOBOS [44], BRAHMS [43], and STAR (preliminary) [51] results in Au+Au central collisions at $\sqrt{s_{NN}}$=200 GeV at midrapidity. The thermal model prediction [10] for 200 GeV Au+Au central collisions are also shown as dotted lines. The error bars on data indicate the systematic errors.

charged and neutral pions agree within 5–15%. The error bars on the PHENIX data points in the figure show the quadratic sum of the statistical errors and the point-to-point systematic errors. There is an additional normalization uncertainty of 8% for p/π^+, $\bar{p}/\pi^-$ and 12% for p/π^0, $\bar{p}/\pi^0$ [the quadratic sum of the systematic errors on p (or $\bar{p}$) normalization and p_T independent systematic errors from π^0 [23]], which may shift the data up or down for all three centrality bins together, but does not affect their shape. The ratios increase rapidly at low p_T, but saturate at different values of p_T which increase from peripheral to central collisions. In central collisions, the yields of both protons and antiprotons are comparable to that of pions for $p_T > 2$ GeV/c. For comparison, the corresponding ratios for $p_T > 2$ GeV/c observed in $p+p$ collisions at lower energies [47], and in gluon jets produced in $e^+ + e^-$ collisions [48], are also shown. Within the uncertainties those ratios are compatible with the peripheral Au+Au results. In hard-scattering processes described by pQCD, the p/π and $\bar{p}/\pi$ ratios at high p_T are determined by the fragmentation of energetic partons, independent of the initial colliding system, which is seen as agreement between $p+p$ and $e^+ + e^-$ collisions. Thus, the clear increase in the p/π ($\bar{p}/\pi$) ratios at high p_T from $p+p$ and peripheral to the midcentral and to the central Au+Au collisions requires ingredients other than pQCD.

The first observation of the enhancement of protons and antiprotons compared to pions in the intermediate p_T region was in the 130 GeV Au+Au data [6]. The data inspired several new theoretical interpretations and models. Hydrodynamics calculations [32] predict that the $\bar{p}/\pi$ ratio at high p_T exceeds unity for central collisions. The expected $\bar{p}/\pi$ ratio in the thermal model at fixed and sufficiently large p_T is determined by $2e^{-\mu_B/T_{ch}} \approx 1.7$ using T_{ch}=1.77 MeV and μ_B =29 MeV [10] for 200 GeV Au+Au central collisions. Due to the strong radial flow effect at RHIC at relativistic transverse momenta ($p_T \gg m$), all hadron spectra have a similar shape. The hydrodynamic model thus explains the excess of $\bar{p}/\pi$ in central collisions at intermediate p_T. However, the hydrodynamic model [49] predicts no or very little dependence on the centrality, which clearly disagrees with the present data. This model predicts, within 10%, the same p_T dependence of p/π ($\bar{p}/\pi$) for all centrality bins.

Recently, two new models have been proposed to explain the experimental results on the p_T dependence of p/π and $\bar{p}/\pi$ ratios. One model is the parton recombination and fragmentation model [45] and the other model is the baryon junction model [50]. Both models explain qualitatively the observed feature of p/π enhancement in central collisions, and their centrality dependencies. Furthermore, both theoretical models predict that this baryon enhancement is limited to $p_T < 5$–6 GeV/c. This will be discussed in Sec. IV E in detail.

2. Particle ratio versus N_{part}

Figure 19 shows the centrality dependence of particle ratios for π^-/π^+, K^-/K^+, and $\bar{p}/p$. The ratios presented here are derived from the integrated yields over p_T (i.e., dN/dy). The shaded boxes on each data point indicate the systematic errors. Within uncertainties, the ratios are all independent of N_{part} over the measured range. Figure 20 shows a comparison of the PHENIX particle ratios with those from PHOBOS [44], BRAHMS [43], and STAR (preliminary) [51] in Au +Au central collisions at $\sqrt{s_{NN}}$=200 GeV at midrapidity. The PHENIX antiparticle-to-particle ratios are consistent with other experimental results within the systematic uncertainties.

Figure 21 shows the centrality dependence of K/π and p/π ratios. Both K^+/π^+ and K^-/π^- ratios increase rapidly

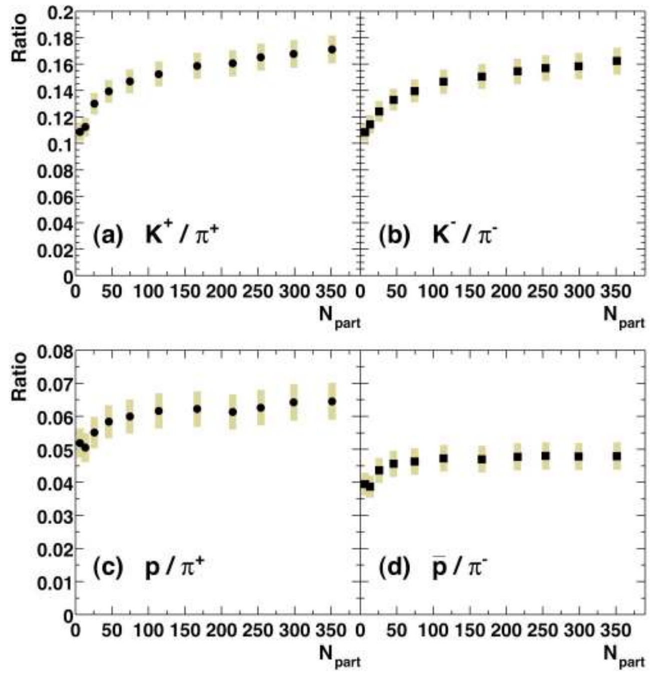

FIG. 21. (Color online) Centrality dependence of particle ratios for (a) K^+/π^+, (b) K^-/π^-, (c) p/π^+, and (d) $\bar{p}/\pi^-$ in Au+Au collisions at $\sqrt{s_{NN}}=200$ GeV. The error bars indicate the statistical errors. The shaded boxes on each data point are the systematic errors.

for peripheral collisions ($N_{part}<100$), and then saturate or rise slowly from the midcentral to the most central collisions. The p/π^+ and $\bar{p}/\pi^-$ ratios increase for peripheral collisions ($N_{part}<50$) and saturate from midcentral to central collisions—similar to the centrality dependence of K/π ratio (but possibly flatter).

Within the framework of the statistical thermal model [9] in a grand canonical ensemble with baryon number, strangeness, and charge conservation [10], particle ratios measured at $\sqrt{s_{NN}}=130$ GeV at midrapidity have been analyzed with the extracted chemical freeze-out temperature T_{ch}

TABLE IX. Comparison between the data for the 0–5% central collisions and the thermal model prediction at $\sqrt{s_{NN}}=200$ GeV with $T_{ch}=177$ MeV and $\mu_B=29$ MeV [10].

Particles	Ratio±stat.±sys.	Thermal model
π^-/π^+	$0.984\pm0.004\pm0.057$	1.004
K^-/K^+	$0.933\pm0.007\pm0.054$	0.932
$\bar{p}/p$	$0.731\pm0.011\pm0.062$	
$\bar{p}/p$ (Inclusive)	$0.747\pm0.007\pm0.046$	0.752
K^+/π^+	$0.171\pm0.001\pm0.010$	
K^-/π^-	$0.162\pm0.001\pm0.010$	0.147
p/π^+	$0.064\pm0.001\pm0.003$	
p/π^+ (Inclusive)	$0.099\pm0.001\pm0.006$	
$\bar{p}/\pi^-$	$0.047\pm0.001\pm0.002$	
$\bar{p}/\pi^-$ (Inclusive)	$0.075\pm0.001\pm0.004$	0.089

$=174\pm7$ MeV and baryon chemical potential $\mu_B=46\pm5$ MeV. A set of chemical parameters at $\sqrt{s_{NN}}=200$ GeV in Au+Au were also predicted by using a phenomenological parametrization of the energy dependence of μ_B. The predictions were $\mu_B=29\pm8$ MeV and $T_{ch}=177\pm7$ MeV at $\sqrt{s_{NN}}=200$ GeV. The comparison between the PHENIX data at 200 GeV for 0–5% central and the thermal model prediction is shown in Table IX and Fig. 20. There is a good agreement between data and the model. The thermal model calculation was performed by assuming a 50% reconstruction efficiency of all weakly decaying baryons in Ref. [10]. However, our results have been corrected to remove these contributions. Therefore, Table IX includes $\bar{p}/p$ and $\bar{p}/\pi^-$ ratios with and without Λ ($\bar{\Lambda}$) feed-down corrections to the proton and antiproton spectra. The ratios without the Λ ($\bar{\Lambda}$) feed-down correction are labeled "inclusive." The small μ_B is qualitatively consistent with our measurement of the number of net protons (≈5) in central Au+Au collisions at $\sqrt{s_{NN}}=200$ GeV at midrapidity.

E. Binary collision scaling of p_T spectra

One of the most striking features in Au+Au collisions at RHIC is that π^0 and nonidentified hadron yields at $p_T>2$ GeV/c in central collisions are suppressed with respect to the number of nucleon-nucleon binary collisions (N_{coll}) scaled by $p+p$ and peripheral Au+Au results [12–14]. Moreover, the suppression of π^0 is stronger than that for nonidentified charged hadrons [12], and the yields of protons and antiprotons in central collisions are comparable to that of pions around $p_T=2$ GeV/c [6]. The enhancement of the p/π ($\bar{p}/\pi$) ratio in central collisions at intermediate p_T (2.0–4.5 GeV/c), which was presented in the preceding section, is consistent with the above observations. These results show the significant contributions of proton and antiproton yields to the total particle composition at this intermediate p_T region. We present here the N_{coll} scaling behavior for charged pions, kaons, and protons (antiprotons) in order to quantify the particle composition at intermediate p_T.

Figure 22 shows the p_T spectra scaled by the averaged number of binary collisions, $\langle N_{coll}\rangle$, for $(\pi^++\pi^-)/2$, $(K^++K^-)/2$, and $(p+\bar{p})/2$ in three centrality bins: central 0–10%, midcentral 40–50%, and peripheral 60–92%. For $(p+\bar{p})/2$ in the range of $p_T=1.5$–4.5 GeV/c, it is clearly seen that the spectra are on top of each other. This indicates that proton and antiproton production at high p_T scales with the number of binary collisions. On the other hand, at p_T below 1.5 GeV/c, different shapes for different centrality bins are observed, which indicates a strong contribution from radial flow. The scaling behavior of the kaons seems to be similar to protons, but this is not conclusive due to our PID limitations. For pions, the N_{coll} scaled yield in central events is suppressed compared to that for peripheral events at $p_T>2$ GeV/c, which is consistent with the results in the π^0 spectra [12,14].

Figure 23 shows the central (0–10%) to peripheral (60–92%) ratio for N_{coll} scaled p_T spectra ($R_{\rm CP}$: the nuclear modification factor) of $(\bar{p}+p)/2$, kaons, charged pions, and π^0. In this paper we define $R_{\rm CP}$ as

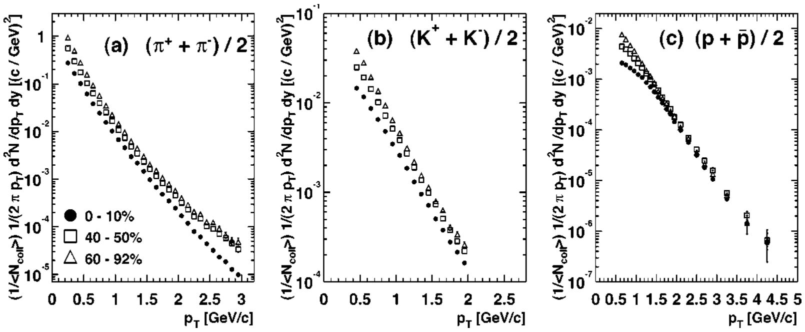

FIG. 22. p_T spectra scaled by the averaged number of binary collisions for averaged charged (a) pions, (b) kaons, and (c) $(p+\bar{p})/2$ in three different centrality bins: central 0–10%, midcentral 40–50%, and peripheral 60–92% in Au+Au collisions at $\sqrt{s_{NN}}$=200 GeV. The error bars are statistical only. Note the different horizontal and vertical scales on the three plots.

$$R_{\rm CP} = \frac{{\rm Yield}^{0-10\%}/\langle N_{coll}{}^{0-10\%}\rangle}{{\rm Yield}^{60-92\%}/\langle N_{coll}{}^{60-92\%}\rangle}. \qquad (10)$$

The peripheral 60–92% Au+Au spectrum is used as an approximation of the yields in $p+p$ collisions, based on the experimental fact that the peripheral spectra scale with N_{coll} by using the yields in $p+p$ collisions measured by PHENIX [14,24]. Thus the meaning of the $R_{\rm CP}$ is expected to be the same as $R_{\rm AA}$ used in our previous publications [12–14]. The lines in Fig. 23 indicate the expectations of N_{part} (dotted) and N_{coll} (dashed) scaling. The shaded bars at the end of each line represent the systematic error associated with the determination of these quantities for central and peripheral events. The error bars on charged particles are statistical errors only, and those for π^0 are the quadratic sum of the statistical errors and the point-to-point systematic errors. The data show that $(\bar{p}+p)/2$ reaches unity for $p_T \gtrsim 1.5$ GeV/c, consistent with N_{coll} scaling. The data for kaons also show the N_{coll} scaling behavior around 1.5–2.0 GeV/c, but the behavior is weaker than for protons. As with neutral pions [14], charged pions are also suppressed at 2–3 GeV/c with respect to peripheral Au+Au collisions.

Motivated by the observation that the $(\bar{p}+p)/2$ spectra scale with N_{coll} above p_T=1.5 GeV/c, the ratio of the integrated yield between central and peripheral events (scaled by the corresponding N_{coll}) above p_T=1.5 GeV/c are shown in Fig. 24 as a function of N_{part}. The p_T ranges for the integration are 1.5–4.5 GeV/c for $(\bar{p}+p)/2$, 1.5–2.0 GeV/c for kaons, and 1.5–3.0 GeV/c for charged pions. The data points are normalized to the most peripheral data point. The shaded boxes in the figure indicate the systematic errors, which include the normalization errors on the p_T spectra, the errors on the detector occupancy corrections, and the uncertainties of the $\langle T_{\rm AuAu}\rangle$ determination for the numerator only. Only at the most peripheral data point, the uncertainty on the denominator $\langle T^{60-92\%}_{\rm AuAu}\rangle$ is also added. The figure shows that $(\bar{p}+p)/2$ scales with N_{coll} for all centrality bins, while the data for charged pions show a decrease with N_{part}. The kaon data points are between the charged pions and the $(\bar{p}+p)/2$ spectra.

The standard picture of hadron production at high momentum is the fragmentation of energetic partons. While the observed suppression of the π^0 yield at high p_T in central collisions may be attributed to the energy loss of partons during their propagation through the hot and dense matter

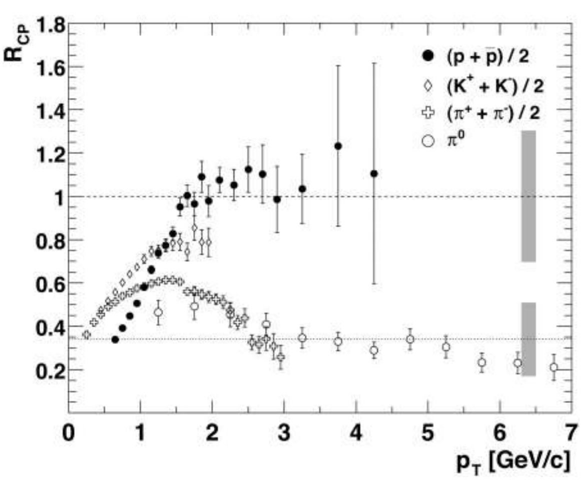

FIG. 23. Central (0–10%) to peripheral (60–92%) ratios of binary-collision-scaled p_T spectra, R_{CP}, as a function of p_T for $(\bar{p}+p)/2$, charged kaons, charged pions, and π^0 [14] in Au+Au collisions at $\sqrt{s_{NN}}$=200 GeV. The lines indicate the expectations of N_{part} (dotted) and N_{coll} (dashed) scaling, the shaded bars represent the systematic errors on these quantities.

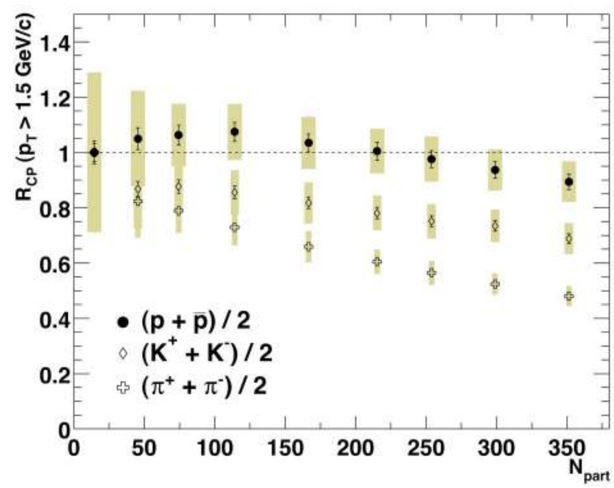

FIG. 24. (Color online) Centrality dependence of integrated R_{CP} above 1.5 GeV/c normalized to the most peripheral 60–92% value. The data show R_{CP} for $(\bar{p}+p)/2$, charged kaons, and charged pions in Au+Au collisions at $\sqrt{s_{NN}}$=200 GeV. The error bars are statistical only. The shaded boxes represent the systematic errors (see text for details).

created in the collisions, i.e., jet quenching [15,16], it is a theoretical challenge to explain the absence of suppression for baryons up to 4.5 GeV/c for all centralities along with the enhancement of the p/π ratio at p_T=2–4 GeV/c for central collisions.

It has been recently proposed that such observations can be explained by the dominance of parton recombination at intermediate p_T, rather than by fragmentation [45]. The competition between recombination and fragmentation of partons may explain the observed features. The model predicts that the effect is limited to $p_T<5$ GeV/c, beyond which fragmentation becomes the dominant production mechanism for all particle species.

Another possible explanation is the baryon junction model [50]. It invokes a topological gluon configuration with jet quenching. With pion production above 2 GeV/c suppressed by jet quenching, gluon junctions produce copious baryons at intermediate p_T, thus leading to the enhancement of baryons in this p_T region. The model reproduces the baryon-to-meson ratio and its centrality dependence qualitatively [52].

Both theoretical models predict that baryon enhancement is limited to $p_T<5$–6 GeV/c, which is unfortunately beyond our current PID capability. However, it is possible to test the two predictions indirectly by using the nonidentified charged hadrons to neutral pion ratio (h/π^0) as a measure of the baryon content at high p_T, as published in Ref. [23]. The results support the limited behavior of baryon enhancement up to 5 GeV/c in p_T. Similar trends are observed in Λ, K_S^0, and $K^{\pm}$ measurements by the STAR Collaboration [53].

On the other hand, it is also possible that nuclear effects, such as the "Cronin effect" [54,55], attributed to initial state multiple scattering (p_T broadening) [56], contribute to the observed species dependence. At center-of-mass energies up to $\sqrt{s}$=38.8 GeV, a nuclear enhancement beyond N_{coll} scaling has been observed for π, K, p, and their antiparticles in $p+A$ collisions. The effect is stronger for protons and antiprotons than for pions, which leads to an enhancement of the p/π and $\bar{p}/\pi$ ratios compared to $p+p$ collisions. In proton-tungsten reactions, the increase is a factor of $\sim$2 in the range $3<p_T<6$ GeV. For pions, theoretical calculations at RHIC energies [57] predict a reduced strength of the Cronin effect compared to lower energies, although no prediction exists for protons. New data from d+Au collisions at $\sqrt{s_{NN}}$=200 GeV will help to clarify this issue.

V. SUMMARY AND CONCLUSION

In summary, we present the centrality dependence of identified charged hadron spectra and yields for $\pi^{\pm}$, $K^{\pm}$, p and $\bar{p}$ in Au+Au collisions at $\sqrt{s_{NN}}$=200 GeV at midrapidity. In central events, the low p_T region ($\leqslant$2.0 GeV/c) of the p_T spectra show a clear particle mass dependence in their shapes, namely, p and $\bar{p}$ spectra have a shoulder-arm shape while the pion spectra have a concave shape. The spectra can be well fit with an exponential function in m_T at the region below 1.0 GeV/c^2 in m_T-m_0. The resulting inverse slope parameters show clear particle mass and centrality dependences that increase with particle mass and centrality. These observations are consistent with the hydrodynamic radial flow picture. Moreover, at around p_T=2.0 GeV/c in central events, the p and $\bar{p}$ yields are comparable to the pion yields. Here, baryons comprise a significant fraction of the hadron yield in this intermediate p_T range. The $\langle p_T\rangle$ and dN/dy per participant pair increase from peripheral to midcentral collisions and saturate for the most central collisions for all particle species. The net proton number in Au+Au central collisions at $\sqrt{s_{NN}}$=200 GeV is $\sim$5 at midrapidity.

The particle ratios of π^-/π^+, K^-/K^+, $p/\bar{p}$, K/π, p/π, and $\bar{p}/\pi$ as a function of p_T and centrality have been measured. Particle ratios in central Au+Au collisions are well reproduced by the statistical thermal model with a baryon chemical potential of μ_B=29 MeV and a chemical freeze-out temperature of T_{ch}=177 MeV. Regardless of the particle species and centrality, it is found that ratios for equal mass particles are constant as a function of p_T, within the systematic uncertainties in the measured p_T range. On the other hand, both K/π and p/π ($\bar{p}/\pi$) ratios increase as a function of p_T. This increase with p_T is stronger for central than for peripheral events. The p/π and $\bar{p}/\pi$ ratios in central events both increase with p_T up to 3 GeV/c and approach unity at $p_T \approx 2$ GeV/c. However, in peripheral collisions these ratios saturate at the value of 0.3–0.4 around p_T=1.5 GeV/c. The observed centrality dependence of p/π and $\bar{p}/\pi$ ratios in intermediate p_T region is not explained by the hydrodynamic model alone, but both the parton recombination model and the baryon junction model qualitatively agree with data.

The scaling behavior of identified charged hadrons is compared with results for neutral pions. In the N_{coll} scaled p_T spectra for $(p+\bar{p})/2$, the spectra scale with N_{coll} from p_T =1.5 to 4.5 GeV/c. The central-to-peripheral ratio R_{CP} approaches unity for $(\bar{p}+p)/2$ from p_T=1.5 up to 4.5 GeV/c. Meanwhile, charged and neutral pions are suppressed. The ratio of integrated R_{CP} from p_T=1.5 to 4.5 GeV/c exhibits an N_{coll} scaling behavior for all centrality bins in the $(\bar{p}+p)/2$ data, which is in contrast to the stronger pion suppression that increases with centrality.

ACKNOWLEDGMENTS

We thank the staff of the Collider-Accelerator and Physics Departments at Brookhaven National Laboratory and the staff of the other PHENIX participating institutions for their vital contributions. We acknowledge support from the Department of Energy, Office of Science, Nuclear Physics Division, the National Science Foundation, Abilene Christian University Research Council, Research Foundation of SUNY, and Dean of the College of Arts and Sciences, Vanderbilt University (USA), Ministry of Education, Culture, Sports, Science, and Technology and the Japan Society for the Promotion of Science (Japan), Conselho Nacional de Desenvolvimento Científico e Tecnológico and Fundação de Amparo à Pesquisa do Estado de São Paulo (Brazil), Natural Science Foundation of China (People's Republic of China), Centre National de la Recherche Scientifique, Commissariat à l'Énergie Atomique, Institut National de Physique Nucléaire et de Physique des Particules, and Institut National de Physique Nucléaire et de Physique des Particules (France), Bundesministerium fuer Bildung und Forschung, Deutscher Akademischer Austausch Dienst, and Alexander von Humboldt Stiftung (Germany), Hungarian National Science Fund, OTKA (Hungary), Department of Atomic Energy and Department of Science and Technology (India), Israel Science Foundation (Israel), Korea Research Foundation and Center for High Energy Physics (Korea), Russian Ministry of Industry, Science and Tekhnologies, Russian Academy of Science, Russian Ministry of Atomic Energy (Russia), VR and the Wallenberg Foundation (Sweden), the U.S. Civilian Research and Development Foundation for the Independent States of the Former Soviet Union, the US-Hungarian NSF-OTKA-MTA, the US-Israel Binational Science Foundation, and the Fifth European Union TMR Marie-Curie Programme.

APPENDIX: TABLE OF INVARIANT YIELDS

The invariant yields for $\pi^{\pm}$, $K^{\pm}$, p, and $\bar{p}$ in Au+Au collisions at $\sqrt{s_{NN}}$=200 GeV at midrapidity are tabulated in Tables X–XXIX. The data presented here are for the minimum bias events and each centrality bin (0–5%, 5–10%, 10–15%, 15–20%, 20–30%,…, 70–80%, 80–92%, and 60–92%). Errors are statistical only.

TABLE X. Invariant yields for π^{+} at midrapidity in the minimum bias, 0–5%, 5–10%, and 10–15% centrality bins, normalized to unit rapidity. Errors are statistical only.

p_T (GeV/c)	Minimum bias	0–5%	5–10%	10–15%
0.25	$1.07\times10^{2}\pm8.8\times10^{-1}$	$3.29\times10^{2}\pm2.7\times10^{0}$	$2.76\times10^{2}\pm2.3\times10^{0}$	$2.39\times10^{2}\pm2.0\times10^{0}$
0.35	$6.06\times10^{1}\pm5.0\times10^{-1}$	$1.97\times10^{2}\pm1.6\times10^{0}$	$1.64\times10^{2}\pm1.4\times10^{0}$	$1.39\times10^{2}\pm1.2\times10^{0}$
0.45	$3.63\times10^{1}\pm3.1\times10^{-1}$	$1.20\times10^{2}\pm1.1\times10^{0}$	$9.93\times10^{1}\pm8.7\times10^{-1}$	$8.41\times10^{1}\pm7.4\times10^{-1}$
0.55	$2.18\times10^{1}\pm2.0\times10^{-1}$	$7.26\times10^{1}\pm6.7\times10^{-1}$	$6.02\times10^{1}\pm5.6\times10^{-1}$	$5.08\times10^{1}\pm4.7\times10^{-1}$
0.65	$1.34\times10^{1}\pm1.3\times10^{-1}$	$4.49\times10^{1}\pm4.5\times10^{-1}$	$3.74\times10^{1}\pm3.8\times10^{-1}$	$3.16\times10^{1}\pm3.2\times10^{-1}$
0.75	$8.71\times10^{0}\pm9.5\times10^{-2}$	$2.93\times10^{1}\pm3.3\times10^{-1}$	$2.43\times10^{1}\pm2.7\times10^{-1}$	$2.05\times10^{1}\pm2.3\times10^{-1}$
0.85	$5.41\times10^{0}\pm6.3\times10^{-2}$	$1.82\times10^{1}\pm2.2\times10^{-1}$	$1.53\times10^{1}\pm1.8\times10^{-1}$	$1.29\times10^{1}\pm1.6\times10^{-1}$
0.95	$3.59\times10^{0}\pm4.5\times10^{-2}$	$1.21\times10^{1}\pm1.6\times10^{-1}$	$1.01\times10^{1}\pm1.3\times10^{-1}$	$8.56\times10^{0}\pm1.1\times10^{-1}$
1.05	$2.35\times10^{0}\pm3.1\times10^{-2}$	$7.96\times10^{0}\pm1.1\times10^{-1}$	$6.56\times10^{0}\pm9.3\times10^{-2}$	$5.56\times10^{0}\pm8.0\times10^{-2}$
1.15	$1.58\times10^{0}\pm2.2\times10^{-2}$	$5.32\times10^{0}\pm8.0\times10^{-2}$	$4.47\times10^{0}\pm6.8\times10^{-2}$	$3.72\times10^{0}\pm5.7\times10^{-2}$
1.25	$1.05\times10^{0}\pm1.5\times10^{-2}$	$3.55\times10^{0}\pm5.7\times10^{-2}$	$2.99\times10^{0}\pm4.9\times10^{-2}$	$2.51\times10^{0}\pm4.2\times10^{-2}$
1.35	$7.59\times10^{-1}\pm1.2\times10^{-2}$	$2.55\times10^{0}\pm4.5\times10^{-2}$	$2.15\times10^{0}\pm3.9\times10^{-2}$	$1.81\times10^{0}\pm3.3\times10^{-2}$
1.45	$5.16\times10^{-1}\pm8.3\times10^{-3}$	$1.72\times10^{0}\pm3.3\times10^{-2}$	$1.45\times10^{0}\pm2.8\times10^{-2}$	$1.23\times10^{0}\pm2.5\times10^{-2}$
1.55	$3.37\times10^{-1}\pm5.6\times10^{-3}$	$1.13\times10^{0}\pm2.3\times10^{-2}$	$9.36\times10^{-1}\pm2.0\times10^{-2}$	$7.93\times10^{-1}\pm1.7\times10^{-2}$
1.65	$2.44\times10^{-1}\pm4.2\times10^{-3}$	$8.05\times10^{-1}\pm1.8\times10^{-2}$	$6.68\times10^{-1}\pm1.6\times10^{-2}$	$5.78\times10^{-1}\pm1.4\times10^{-2}$
1.75	$1.77\times10^{-1}\pm3.3\times10^{-3}$	$5.70\times10^{-1}\pm1.4\times10^{-2}$	$4.84\times10^{-1}\pm1.3\times10^{-2}$	$4.19\times10^{-1}\pm1.1\times10^{-2}$
1.85	$1.27\times10^{-1}\pm2.4\times10^{-3}$	$4.18\times10^{-1}\pm1.2\times10^{-2}$	$3.42\times10^{-1}\pm1.0\times10^{-2}$	$2.99\times10^{-1}\pm9.1\times10^{-3}$
1.95	$9.01\times10^{-2}\pm1.9\times10^{-3}$	$2.80\times10^{-1}\pm9.0\times10^{-3}$	$2.50\times10^{-1}\pm8.3\times10^{-3}$	$2.07\times10^{-1}\pm7.3\times10^{-3}$
2.05	$6.68\times10^{-2}\pm1.2\times10^{-3}$	$2.09\times10^{-1}\pm6.1\times10^{-3}$	$1.82\times10^{-1}\pm5.6\times10^{-3}$	$1.56\times10^{-1}\pm5.0\times10^{-3}$
2.15	$4.71\times10^{-2}\pm8.9\times10^{-4}$	$1.36\times10^{-1}\pm4.8\times10^{-3}$	$1.27\times10^{-1}\pm4.6\times10^{-3}$	$1.05\times10^{-1}\pm4.1\times10^{-3}$
2.25	$3.27\times10^{-2}\pm6.8\times10^{-4}$	$9.10\times10^{-2}\pm3.8\times10^{-3}$	$8.06\times10^{-2}\pm3.5\times10^{-3}$	$8.05\times10^{-2}\pm3.5\times10^{-3}$
2.35	$2.60\times10^{-2}\pm6.2\times10^{-4}$	$7.20\times10^{-2}\pm3.6\times10^{-3}$	$6.28\times10^{-2}\pm3.3\times10^{-3}$	$5.78\times10^{-2}\pm3.1\times10^{-3}$
2.45	$1.94\times10^{-2}\pm5.3\times10^{-4}$	$5.40\times10^{-2}\pm3.2\times10^{-3}$	$4.57\times10^{-2}\pm2.9\times10^{-3}$	$4.06\times10^{-2}\pm2.7\times10^{-3}$
2.55	$1.49\times10^{-2}\pm4.7\times10^{-4}$	$3.78\times10^{-2}\pm2.8\times10^{-3}$	$3.59\times10^{-2}\pm2.7\times10^{-3}$	$3.18\times10^{-2}\pm2.5\times10^{-3}$
2.65	$1.13\times10^{-2}\pm4.2\times10^{-4}$	$2.65\times10^{-2}\pm2.5\times10^{-3}$	$2.50\times10^{-2}\pm2.4\times10^{-3}$	$2.44\times10^{-2}\pm2.3\times10^{-3}$
2.75	$9.30\times10^{-3}\pm4.0\times10^{-4}$	$2.27\times10^{-2}\pm2.5\times10^{-3}$	$2.19\times10^{-2}\pm2.4\times10^{-3}$	$1.83\times10^{-2}\pm2.1\times10^{-3}$
2.85	$6.20\times10^{-3}\pm3.2\times10^{-4}$	$1.28\times10^{-2}\pm1.9\times10^{-3}$	$1.21\times10^{-2}\pm1.8\times10^{-3}$	$1.30\times10^{-2}\pm1.8\times10^{-3}$
2.95	$5.17\times10^{-3}\pm3.1\times10^{-4}$	$1.03\times10^{-2}\pm1.8\times10^{-3}$	$1.08\times10^{-2}\pm1.8\times10^{-3}$	$1.04\times10^{-2}\pm1.8\times10^{-3}$

TABLE XI. Invariant yields for π^{+} at midrapidity in 15–20%, 20–30%, 30–40%, and 40–50% centrality bins, normalized to unit rapidity. Errors are statistical only.

p_T (GeV/c)	15–20%	20–30%	30–40%	40–50%
0.25	$2.04\times10^{2}\pm1.7\times10^{0}$	$1.57\times10^{2}\pm1.3\times10^{0}$	$1.07\times10^{2}\pm8.9\times10^{-1}$	$6.84\times10^{1}\pm5.7\times10^{-1}$
0.35	$1.18\times10^{2}\pm9.9\times10^{-1}$	$8.82\times10^{1}\pm7.4\times10^{-1}$	$5.86\times10^{1}\pm4.9\times10^{-1}$	$3.67\times10^{1}\pm3.1\times10^{-1}$
0.45	$7.09\times10^{1}\pm6.2\times10^{-1}$	$5.27\times10^{1}\pm4.6\times10^{-1}$	$3.46\times10^{1}\pm3.0\times10^{-1}$	$2.15\times10^{1}\pm1.9\times10^{-1}$
0.55	$4.28\times10^{1}\pm4.0\times10^{-1}$	$3.17\times10^{1}\pm2.9\times10^{-1}$	$2.06\times10^{1}\pm1.9\times10^{-1}$	$1.26\times10^{1}\pm1.2\times10^{-1}$
0.65	$2.65\times10^{1}\pm2.7\times10^{-1}$	$1.95\times10^{1}\pm2.0\times10^{-1}$	$1.26\times10^{1}\pm1.3\times10^{-1}$	$7.66\times10^{0}\pm8.0\times10^{-2}$
0.75	$1.73\times10^{1}\pm2.0\times10^{-1}$	$1.27\times10^{1}\pm1.4\times10^{-1}$	$8.29\times10^{0}\pm9.4\times10^{-2}$	$4.99\times10^{0}\pm5.8\times10^{-2}$
0.85	$1.07\times10^{1}\pm1.3\times10^{-1}$	$7.94\times10^{0}\pm9.5\times10^{-2}$	$5.10\times10^{0}\pm6.3\times10^{-2}$	$3.04\times10^{0}\pm3.9\times10^{-2}$
0.95	$7.12\times10^{0}\pm9.6\times10^{-2}$	$5.31\times10^{0}\pm7.0\times10^{-2}$	$3.38\times10^{0}\pm4.6\times10^{-2}$	$2.02\times10^{0}\pm2.9\times10^{-2}$
1.05	$4.77\times10^{0}\pm6.9\times10^{-2}$	$3.49\times10^{0}\pm4.9\times10^{-2}$	$2.22\times10^{0}\pm3.2\times10^{-2}$	$1.30\times10^{0}\pm2.0\times10^{-2}$
1.15	$3.16\times10^{0}\pm5.0\times10^{-2}$	$2.34\times10^{0}\pm3.5\times10^{-2}$	$1.50\times10^{0}\pm2.4\times10^{-2}$	$8.78\times10^{-1}\pm1.5\times10^{-2}$
1.25	$2.10\times10^{0}\pm3.6\times10^{-2}$	$1.56\times10^{0}\pm2.5\times10^{-2}$	$9.99\times10^{-1}\pm1.7\times10^{-2}$	$5.98\times10^{-1}\pm1.1\times10^{-2}$
1.35	$1.52\times10^{0}\pm2.9\times10^{-2}$	$1.12\times10^{0}\pm2.0\times10^{-2}$	$7.17\times10^{-1}\pm1.4\times10^{-2}$	$4.26\times10^{-1}\pm9.0\times10^{-3}$
1.45	$1.05\times10^{0}\pm2.2\times10^{-2}$	$7.57\times10^{-1}\pm1.5\times10^{-2}$	$4.98\times10^{-1}\pm1.0\times10^{-2}$	$2.91\times10^{-1}\pm6.9\times10^{-3}$
1.55	$6.78\times10^{-1}\pm1.5\times10^{-2}$	$5.07\times10^{-1}\pm1.0\times10^{-2}$	$3.24\times10^{-1}\pm7.4\times10^{-3}$	$1.97\times10^{-1}\pm5.2\times10^{-3}$
1.65	$4.93\times10^{-1}\pm1.2\times10^{-2}$	$3.67\times10^{-1}\pm8.3\times10^{-3}$	$2.31\times10^{-1}\pm5.9\times10^{-3}$	$1.42\times10^{-1}\pm4.2\times10^{-3}$
1.75	$3.60\times10^{-1}\pm1.0\times10^{-2}$	$2.67\times10^{-1}\pm6.7\times10^{-3}$	$1.69\times10^{-1}\pm4.9\times10^{-3}$	$1.03\times10^{-1}\pm3.5\times10^{-3}$
1.85	$2.56\times10^{-1}\pm8.2\times10^{-3}$	$1.92\times10^{-1}\pm5.3\times10^{-3}$	$1.22\times10^{-1}\pm3.9\times10^{-3}$	$7.29\times10^{-2}\pm2.8\times10^{-3}$
1.95	$1.78\times10^{-1}\pm6.6\times10^{-3}$	$1.38\times10^{-1}\pm4.3\times10^{-3}$	$8.80\times10^{-2}\pm3.3\times10^{-3}$	$5.80\times10^{-2}\pm2.5\times10^{-3}$
2.05	$1.35\times10^{-1}\pm4.6\times10^{-3}$	$1.00\times10^{-1}\pm2.9\times10^{-3}$	$6.67\times10^{-2}\pm2.3\times10^{-3}$	$4.13\times10^{-2}\pm1.7\times10^{-3}$
2.15	$1.02\times10^{-1}\pm4.0\times10^{-3}$	$7.41\times10^{-2}\pm2.4\times10^{-3}$	$4.90\times10^{-2}\pm1.9\times10^{-3}$	$2.92\times10^{-2}\pm1.4\times10^{-3}$
2.25	$6.65\times10^{-2}\pm3.1\times10^{-3}$	$5.16\times10^{-2}\pm2.0\times10^{-3}$	$3.58\times10^{-2}\pm1.6\times10^{-3}$	$2.09\times10^{-2}\pm1.2\times10^{-3}$
2.35	$5.43\times10^{-2}\pm3.0\times10^{-3}$	$4.12\times10^{-2}\pm1.9\times10^{-3}$	$2.84\times10^{-2}\pm1.5\times10^{-3}$	$1.87\times10^{-2}\pm1.2\times10^{-3}$
2.45	$3.97\times10^{-2}\pm2.6\times10^{-3}$	$3.28\times10^{-2}\pm1.7\times10^{-3}$	$2.27\times10^{-2}\pm1.4\times10^{-3}$	$1.21\times10^{-2}\pm9.8\times10^{-4}$
2.55	$2.88\times10^{-2}\pm2.4\times10^{-3}$	$2.41\times10^{-2}\pm1.5\times10^{-3}$	$1.70\times10^{-2}\pm1.3\times10^{-3}$	$1.11\times10^{-2}\pm1.0\times10^{-3}$
2.65	$2.21\times10^{-2}\pm2.2\times10^{-3}$	$1.85\times10^{-2}\pm1.4\times10^{-3}$	$1.40\times10^{-2}\pm1.2\times10^{-3}$	$8.92\times10^{-3}\pm9.5\times10^{-4}$
2.75	$1.58\times10^{-2}\pm2.0\times10^{-3}$	$1.55\times10^{-2}\pm1.4\times10^{-3}$	$1.20\times10^{-2}\pm1.2\times10^{-3}$	$7.80\times10^{-3}\pm9.5\times10^{-4}$
2.85	$1.37\times10^{-2}\pm1.9\times10^{-3}$	$1.03\times10^{-2}\pm1.1\times10^{-3}$	$7.69\times10^{-3}\pm9.7\times10^{-4}$	$5.80\times10^{-3}\pm8.3\times10^{-4}$
2.95	$1.08\times10^{-2}\pm1.8\times10^{-3}$	$9.32\times10^{-3}\pm1.2\times10^{-3}$	$6.39\times10^{-3}\pm9.6\times10^{-4}$	$4.49\times10^{-3}\pm7.9\times10^{-4}$

TABLE XII. Invariant yields for π^+ at midrapidity in 50–60%, 60–70%, 70–80%, and 80–92% centrality bins, normalized to unit rapidity. Errors are statistical only.

p_T(GeV/c)	50–60%	60–70%	70–80%	80–92%
0.25	$4.10\times10^{1}\pm3.4\times10^{-1}$	$2.19\times10^{1}\pm1.9\times10^{-1}$	$1.03\times10^{1}\pm9.2\times10^{-2}$	$5.20\times10^{0}\pm5.0\times10^{-2}$
0.35	$2.17\times10^{1}\pm1.9\times10^{-1}$	$1.13\times10^{1}\pm1.0\times10^{-1}$	$5.27\times10^{0}\pm5.0\times10^{-2}$	$2.75\times10^{0}\pm2.8\times10^{-2}$
0.45	$1.24\times10^{1}\pm1.1\times10^{-1}$	$6.37\times10^{0}\pm6.0\times10^{-2}$	$2.95\times10^{0}\pm3.1\times10^{-2}$	$1.49\times10^{0}\pm1.8\times10^{-2}$
0.55	$7.20\times10^{0}\pm7.0\times10^{-2}$	$3.65\times10^{0}\pm3.8\times10^{-2}$	$1.62\times10^{0}\pm1.9\times10^{-2}$	$8.20\times10^{-1}\pm1.1\times10^{-2}$
0.65	$4.33\times10^{0}\pm4.7\times10^{-2}$	$2.18\times10^{0}\pm2.6\times10^{-2}$	$9.63\times10^{-1}\pm1.3\times10^{-2}$	$4.72\times10^{-1}\pm8.1\times10^{-3}$
0.75	$2.78\times10^{0}\pm3.4\times10^{-2}$	$1.36\times10^{0}\pm1.9\times10^{-2}$	$5.91\times10^{-1}\pm9.9\times10^{-3}$	$2.69\times10^{-1}\pm5.9\times10^{-3}$
0.85	$1.67\times10^{0}\pm2.3\times10^{-2}$	$8.36\times10^{-1}\pm1.3\times10^{-2}$	$3.53\times10^{-1}\pm7.1\times10^{-3}$	$1.63\times10^{-1}\pm4.4\times10^{-3}$
0.95	$1.11\times10^{0}\pm1.7\times10^{-2}$	$5.29\times10^{-1}\pm9.6\times10^{-3}$	$2.22\times10^{-1}\pm5.4\times10^{-3}$	$1.02\times10^{-1}\pm3.4\times10^{-3}$
1.05	$7.11\times10^{-1}\pm1.2\times10^{-2}$	$3.51\times10^{-1}\pm7.3\times10^{-3}$	$1.41\times10^{-1}\pm4.1\times10^{-3}$	$6.51\times10^{-2}\pm2.6\times10^{-3}$
1.15	$4.71\times10^{-1}\pm9.2\times10^{-3}$	$2.21\times10^{-1}\pm5.4\times10^{-3}$	$1.01\times10^{-1}\pm3.4\times10^{-3}$	$4.48\times10^{-2}\pm2.2\times10^{-3}$
1.25	$3.14\times10^{-1}\pm6.9\times10^{-3}$	$1.51\times10^{-1}\pm4.3\times10^{-3}$	$6.06\times10^{-2}\pm2.5\times10^{-3}$	$2.63\times10^{-2}\pm1.6\times10^{-3}$
1.35	$2.31\times10^{-1}\pm5.8\times10^{-3}$	$1.10\times10^{-1}\pm3.6\times10^{-3}$	$4.25\times10^{-2}\pm2.1\times10^{-3}$	$2.07\times10^{-2}\pm1.5\times10^{-3}$
1.45	$1.59\times10^{-1}\pm4.6\times10^{-3}$	$7.17\times10^{-2}\pm2.8\times10^{-3}$	$3.04\times10^{-2}\pm1.8\times10^{-3}$	$1.30\times10^{-2}\pm1.1\times10^{-3}$
1.55	$1.02\times10^{-1}\pm3.4\times10^{-3}$	$4.72\times10^{-2}\pm2.2\times10^{-3}$	$1.89\times10^{-2}\pm1.3\times10^{-3}$	$8.48\times10^{-3}\pm8.8\times10^{-4}$
1.65	$7.47\times10^{-2}\pm2.8\times10^{-3}$	$3.50\times10^{-2}\pm1.8\times10^{-3}$	$1.52\times10^{-2}\pm1.2\times10^{-3}$	$7.00\times10^{-3}\pm8.1\times10^{-4}$
1.75	$5.60\times10^{-2}\pm2.4\times10^{-3}$	$2.63\times10^{-2}\pm1.6\times10^{-3}$	$1.03\times10^{-2}\pm1.0\times10^{-3}$	$5.37\times10^{-3}\pm7.1\times10^{-4}$
1.85	$3.80\times10^{-2}\pm2.0\times10^{-3}$	$1.92\times10^{-2}\pm1.3\times10^{-3}$	$8.04\times10^{-3}\pm8.7\times10^{-4}$	$3.87\times10^{-3}\pm6.0\times10^{-4}$
1.95	$2.86\times10^{-2}\pm1.7\times10^{-3}$	$1.41\times10^{-2}\pm1.2\times10^{-3}$	$6.06\times10^{-3}\pm7.6\times10^{-4}$	$2.26\times10^{-3}\pm4.6\times10^{-4}$
2.05	$2.26\times10^{-2}\pm1.2\times10^{-3}$	$1.12\times10^{-2}\pm8.4\times10^{-4}$	$4.34\times10^{-3}\pm5.3\times10^{-4}$	$1.56\times10^{-3}\pm3.1\times10^{-4}$
2.15	$1.60\times10^{-2}\pm1.0\times10^{-3}$	$6.73\times10^{-3}\pm6.6\times10^{-4}$	$3.09\times10^{-3}\pm4.5\times10^{-4}$	$1.23\times10^{-3}\pm2.8\times10^{-4}$
2.25	$1.13\times10^{-2}\pm8.6\times10^{-4}$	$5.46\times10^{-3}\pm5.9\times10^{-4}$	$2.43\times10^{-3}\pm4.0\times10^{-4}$	$8.48\times10^{-4}\pm2.3\times10^{-4}$
2.35	$9.73\times10^{-3}\pm8.5\times10^{-4}$	$4.42\times10^{-3}\pm5.7\times10^{-4}$	$1.98\times10^{-3}\pm3.9\times10^{-4}$	$8.16\times10^{-4}\pm2.5\times10^{-4}$
2.45	$7.73\times10^{-3}\pm7.8\times10^{-4}$	$3.27\times10^{-3}\pm5.0\times10^{-4}$	$1.30\times10^{-3}\pm3.2\times10^{-4}$	$3.19\times10^{-4}\pm1.6\times10^{-4}$
2.55	$5.77\times10^{-3}\pm7.2\times10^{-4}$	$3.38\times10^{-3}\pm5.5\times10^{-4}$	$1.17\times10^{-3}\pm3.3\times10^{-4}$	$5.92\times10^{-4}\pm2.3\times10^{-4}$
2.65	$4.48\times10^{-3}\pm6.7\times10^{-4}$	$2.82\times10^{-3}\pm5.2\times10^{-4}$	$5.70\times10^{-4}\pm2.4\times10^{-4}$	$3.37\times10^{-4}\pm1.8\times10^{-4}$
2.75	$3.84\times10^{-3}\pm6.7\times10^{-4}$	$1.72\times10^{-3}\pm4.4\times10^{-4}$	$8.51\times10^{-4}\pm3.2\times10^{-4}$	$4.22\times10^{-4}\pm2.2\times10^{-4}$
2.85	$2.30\times10^{-3}\pm5.2\times10^{-4}$	$1.35\times10^{-3}\pm4.0\times10^{-4}$	$6.79\times10^{-4}\pm2.9\times10^{-4}$	$1.65\times10^{-4}\pm1.4\times10^{-4}$
2.95	$2.16\times10^{-3}\pm5.5\times10^{-4}$	$1.16\times10^{-3}\pm4.0\times10^{-4}$	$2.88\times10^{-4}\pm2.0\times10^{-4}$	$1.90\times10^{-4}\pm1.6\times10^{-4}$

TABLE XIII. Invariant yields for π^- at midrapidity in the minimum bias, 0–5%, 5–10%, and 10–15% centrality bins, normalized to unit rapidity. Errors are statistical only.

p_T (GeV/c)	Minimum bias	0–5%	5–10%	10–15%
0.25	$1.02\times10^{2}\pm7.9\times10^{-1}$	$3.15\times10^{2}\pm2.4\times10^{0}$	$2.71\times10^{2}\pm2.1\times10^{0}$	$2.27\times10^{2}\pm1.8\times10^{0}$
0.35	$5.92\times10^{1}\pm4.6\times10^{-1}$	$1.94\times10^{2}\pm1.5\times10^{0}$	$1.64\times10^{2}\pm1.3\times10^{0}$	$1.35\times10^{2}\pm1.1\times10^{0}$
0.45	$3.56\times10^{1}\pm2.9\times10^{-1}$	$1.19\times10^{2}\pm9.8\times10^{-1}$	$9.93\times10^{1}\pm8.2\times10^{-1}$	$8.18\times10^{1}\pm6.8\times10^{-1}$
0.55	$2.18\times10^{1}\pm1.9\times10^{-1}$	$7.37\times10^{1}\pm6.5\times10^{-1}$	$6.17\times10^{1}\pm5.4\times10^{-1}$	$5.04\times10^{1}\pm4.5\times10^{-1}$
0.65	$1.34\times10^{1}\pm1.2\times10^{-1}$	$4.57\times10^{1}\pm4.3\times10^{-1}$	$3.82\times10^{1}\pm3.6\times10^{-1}$	$3.15\times10^{1}\pm3.0\times10^{-1}$
0.75	$8.36\times10^{0}\pm8.2\times10^{-2}$	$2.86\times10^{1}\pm2.9\times10^{-1}$	$2.40\times10^{1}\pm2.4\times10^{-1}$	$1.96\times10^{1}\pm2.0\times10^{-1}$
0.85	$5.44\times10^{0}\pm5.7\times10^{-2}$	$1.86\times10^{1}\pm2.0\times10^{-1}$	$1.56\times10^{1}\pm1.7\times10^{-1}$	$1.28\times10^{1}\pm1.4\times10^{-1}$
0.95	$3.58\times10^{0}\pm4.1\times10^{-2}$	$1.22\times10^{1}\pm1.4\times10^{-1}$	$1.02\times10^{1}\pm1.2\times10^{-1}$	$8.47\times10^{0}\pm1.0\times10^{-1}$
1.05	$2.35\times10^{0}\pm2.8\times10^{-2}$	$8.02\times10^{0}\pm1.0\times10^{-1}$	$6.75\times10^{0}\pm8.7\times10^{-2}$	$5.57\times10^{0}\pm7.2\times10^{-2}$
1.15	$1.62\times10^{0}\pm2.1\times10^{-2}$	$5.55\times10^{0}\pm7.7\times10^{-2}$	$4.64\times10^{0}\pm6.5\times10^{-2}$	$3.83\times10^{0}\pm5.5\times10^{-2}$
1.25	$1.04\times10^{0}\pm1.4\times10^{-2}$	$3.53\times10^{0}\pm5.2\times10^{-2}$	$2.94\times10^{0}\pm4.4\times10^{-2}$	$2.46\times10^{0}\pm3.8\times10^{-2}$
1.35	$7.54\times10^{-1}\pm1.1\times10^{-2}$	$2.55\times10^{0}\pm4.1\times10^{-2}$	$2.19\times10^{0}\pm3.6\times10^{-2}$	$1.80\times10^{0}\pm3.0\times10^{-2}$
1.45	$5.07\times10^{-1}\pm7.6\times10^{-3}$	$1.71\times10^{0}\pm3.0\times10^{-2}$	$1.48\times10^{0}\pm2.7\times10^{-2}$	$1.22\times10^{0}\pm2.2\times10^{-2}$
1.55	$3.61\times10^{-1}\pm5.7\times10^{-3}$	$1.20\times10^{0}\pm2.3\times10^{-2}$	$1.02\times10^{0}\pm2.0\times10^{-2}$	$8.63\times10^{-1}\pm1.8\times10^{-2}$
1.65	$2.46\times10^{-1}\pm4.0\times10^{-3}$	$8.02\times10^{-1}\pm1.7\times10^{-2}$	$6.94\times10^{-1}\pm1.5\times10^{-2}$	$5.86\times10^{-1}\pm1.3\times10^{-2}$
1.75	$1.73\times10^{-1}\pm3.0\times10^{-3}$	$5.65\times10^{-1}\pm1.3\times10^{-2}$	$4.91\times10^{-1}\pm1.2\times10^{-2}$	$4.10\times10^{-1}\pm1.0\times10^{-2}$
1.85	$1.25\times10^{-1}\pm2.3\times10^{-3}$	$4.05\times10^{-1}\pm1.1\times10^{-2}$	$3.48\times10^{-1}\pm9.6\times10^{-3}$	$3.00\times10^{-1}\pm8.5\times10^{-3}$
1.95	$8.97\times10^{-2}\pm1.8\times10^{-3}$	$2.85\times10^{-1}\pm8.8\times10^{-3}$	$2.53\times10^{-1}\pm8.1\times10^{-3}$	$2.12\times10^{-1}\pm7.1\times10^{-3}$
2.05	$6.10\times10^{-2}\pm1.1\times10^{-3}$	$1.89\times10^{-1}\pm5.8\times10^{-3}$	$1.64\times10^{-1}\pm5.4\times10^{-3}$	$1.42\times10^{-1}\pm4.8\times10^{-3}$
2.15	$4.43\times10^{-2}\pm8.7\times10^{-4}$	$1.32\times10^{-1}\pm4.8\times10^{-3}$	$1.20\times10^{-1}\pm4.5\times10^{-3}$	$1.01\times10^{-1}\pm4.0\times10^{-3}$
2.25	$3.20\times10^{-2}\pm7.0\times10^{-4}$	$9.24\times10^{-2}\pm4.0\times10^{-3}$	$8.31\times10^{-2}\pm3.8\times10^{-3}$	$7.21\times10^{-2}\pm3.4\times10^{-3}$
2.35	$2.52\times10^{-2}\pm6.3\times10^{-4}$	$7.07\times10^{-2}\pm3.7\times10^{-3}$	$6.29\times10^{-2}\pm3.5\times10^{-3}$	$5.95\times10^{-2}\pm3.3\times10^{-3}$
2.45	$1.79\times10^{-2}\pm5.1\times10^{-4}$	$4.71\times10^{-2}\pm3.0\times10^{-3}$	$4.47\times10^{-2}\pm2.9\times10^{-3}$	$3.97\times10^{-2}\pm2.7\times10^{-3}$
2.55	$1.41\times10^{-2}\pm4.8\times10^{-4}$	$3.50\times10^{-2}\pm2.8\times10^{-3}$	$3.33\times10^{-2}\pm2.7\times10^{-3}$	$3.28\times10^{-2}\pm2.7\times10^{-3}$
2.65	$1.06\times10^{-2}\pm4.1\times10^{-4}$	$2.69\times10^{-2}\pm2.5\times10^{-3}$	$2.36\times10^{-2}\pm2.3\times10^{-3}$	$2.22\times10^{-2}\pm2.2\times10^{-3}$
2.75	$8.05\times10^{-3}\pm3.7\times10^{-4}$	$1.99\times10^{-2}\pm2.3\times10^{-3}$	$1.67\times10^{-2}\pm2.1\times10^{-3}$	$1.61\times10^{-2}\pm2.0\times10^{-3}$
2.85	$6.45\times10^{-3}\pm3.5\times10^{-4}$	$1.45\times10^{-2}\pm2.1\times10^{-3}$	$1.63\times10^{-2}\pm2.2\times10^{-3}$	$1.21\times10^{-2}\pm1.9\times10^{-3}$
2.95	$4.95\times10^{-3}\pm3.2\times10^{-4}$	$1.08\times10^{-2}\pm1.9\times10^{-3}$	$1.16\times10^{-2}\pm2.0\times10^{-3}$	$1.03\times10^{-2}\pm1.8\times10^{-3}$

TABLE XIV. Invariant yields for π^- at midrapidity in 15–20%, 20–30%, 30–40%, and 40–50% centrality bins, normalized to unit rapidity. Errors are statistical only.

p_T (GeV/c)	15–20%	20–30%	30–40%	40–50%
0.25	$1.95\times10^{2}\pm1.5\times10^{0}$	$1.51\times10^{2}\pm1.2\times10^{0}$	$1.02\times10^{2}\pm7.9\times10^{-1}$	$6.53\times10^{1}\pm5.1\times10^{-1}$
0.35	$1.13\times10^{2}\pm9.0\times10^{-1}$	$8.62\times10^{1}\pm6.8\times10^{-1}$	$5.68\times10^{1}\pm4.5\times10^{-1}$	$3.56\times10^{1}\pm2.8\times10^{-1}$
0.45	$6.86\times10^{1}\pm5.7\times10^{-1}$	$5.18\times10^{1}\pm4.3\times10^{-1}$	$3.36\times10^{1}\pm2.8\times10^{-1}$	$2.08\times10^{1}\pm1.7\times10^{-1}$
0.55	$4.22\times10^{1}\pm3.7\times10^{-1}$	$3.17\times10^{1}\pm2.8\times10^{-1}$	$2.04\times10^{1}\pm1.8\times10^{-1}$	$1.24\times10^{1}\pm1.1\times10^{-1}$
0.65	$2.61\times10^{1}\pm2.5\times10^{-1}$	$1.95\times10^{1}\pm1.8\times10^{-1}$	$1.26\times10^{1}\pm1.2\times10^{-1}$	$7.57\times10^{0}\pm7.4\times10^{-2}$
0.75	$1.63\times10^{1}\pm1.7\times10^{-1}$	$1.22\times10^{1}\pm1.2\times10^{-1}$	$7.81\times10^{0}\pm8.0\times10^{-2}$	$4.67\times10^{0}\pm4.9\times10^{-2}$
0.85	$1.06\times10^{1}\pm1.2\times10^{-1}$	$7.96\times10^{0}\pm8.7\times10^{-2}$	$5.06\times10^{0}\pm5.7\times10^{-2}$	$3.04\times10^{0}\pm3.5\times10^{-2}$
0.95	$7.01\times10^{0}\pm8.6\times10^{-2}$	$5.31\times10^{0}\pm6.3\times10^{-2}$	$3.37\times10^{0}\pm4.1\times10^{-2}$	$1.99\times10^{0}\pm2.6\times10^{-2}$
1.05	$4.68\times10^{0}\pm6.2\times10^{-2}$	$3.45\times10^{0}\pm4.4\times10^{-2}$	$2.18\times10^{0}\pm2.9\times10^{-2}$	$1.30\times10^{0}\pm1.8\times10^{-2}$
1.15	$3.19\times10^{0}\pm4.6\times10^{-2}$	$2.36\times10^{0}\pm3.3\times10^{-2}$	$1.52\times10^{0}\pm2.2\times10^{-2}$	$8.96\times10^{-1}\pm1.4\times10^{-2}$
1.25	$2.05\times10^{0}\pm3.2\times10^{-2}$	$1.55\times10^{0}\pm2.3\times10^{-2}$	$9.75\times10^{-1}\pm1.5\times10^{-2}$	$5.68\times10^{-1}\pm9.8\times10^{-3}$
1.35	$1.49\times10^{0}\pm2.6\times10^{-2}$	$1.10\times10^{0}\pm1.8\times10^{-2}$	$7.11\times10^{-1}\pm1.2\times10^{-2}$	$4.18\times10^{-1}\pm8.2\times10^{-3}$
1.45	$9.90\times10^{-1}\pm1.9\times10^{-2}$	$7.55\times10^{-1}\pm1.3\times10^{-2}$	$4.76\times10^{-1}\pm9.2\times10^{-3}$	$2.75\times10^{-1}\pm6.1\times10^{-3}$
1.55	$7.11\times10^{-1}\pm1.5\times10^{-2}$	$5.41\times10^{-1}\pm1.1\times10^{-2}$	$3.42\times10^{-1}\pm7.4\times10^{-3}$	$2.01\times10^{-1}\pm5.0\times10^{-3}$
1.65	$4.85\times10^{-1}\pm1.2\times10^{-2}$	$3.71\times10^{-1}\pm7.9\times10^{-3}$	$2.37\times10^{-1}\pm5.7\times10^{-3}$	$1.40\times10^{-1}\pm3.9\times10^{-3}$
1.75	$3.43\times10^{-1}\pm9.2\times10^{-3}$	$2.56\times10^{-1}\pm6.1\times10^{-3}$	$1.68\times10^{-1}\pm4.5\times10^{-3}$	$9.60\times10^{-2}\pm3.1\times10^{-3}$
1.85	$2.38\times10^{-1}\pm7.3\times10^{-3}$	$1.93\times10^{-1}\pm5.0\times10^{-3}$	$1.20\times10^{-1}\pm3.7\times10^{-3}$	$7.36\times10^{-2}\pm2.7\times10^{-3}$
1.95	$1.74\times10^{-1}\pm6.2\times10^{-3}$	$1.36\times10^{-1}\pm4.1\times10^{-3}$	$8.73\times10^{-2}\pm3.1\times10^{-3}$	$5.34\times10^{-2}\pm2.3\times10^{-3}$
2.05	$1.16\times10^{-1}\pm4.2\times10^{-3}$	$9.65\times10^{-2}\pm2.9\times10^{-3}$	$6.46\times10^{-2}\pm2.2\times10^{-3}$	$3.64\times10^{-2}\pm1.6\times10^{-3}$
2.15	$8.98\times10^{-2}\pm3.7\times10^{-3}$	$6.97\times10^{-2}\pm2.4\times10^{-3}$	$4.55\times10^{-2}\pm1.9\times10^{-3}$	$2.72\times10^{-2}\pm1.4\times10^{-3}$
2.25	$6.55\times10^{-2}\pm3.2\times10^{-3}$	$5.15\times10^{-2}\pm2.1\times10^{-3}$	$3.60\times10^{-2}\pm1.7\times10^{-3}$	$1.95\times10^{-2}\pm1.2\times10^{-3}$
2.35	$5.02\times10^{-2}\pm2.9\times10^{-3}$	$3.83\times10^{-2}\pm1.9\times10^{-3}$	$2.83\times10^{-2}\pm1.6\times10^{-3}$	$1.76\times10^{-2}\pm1.2\times10^{-3}$
2.45	$3.62\times10^{-2}\pm2.5\times10^{-3}$	$2.84\times10^{-2}\pm1.6\times10^{-3}$	$1.94\times10^{-2}\pm1.3\times10^{-3}$	$1.33\times10^{-2}\pm1.0\times10^{-3}$
2.55	$2.55\times10^{-2}\pm2.3\times10^{-3}$	$2.37\times10^{-2}\pm1.6\times10^{-3}$	$1.57\times10^{-2}\pm1.3\times10^{-3}$	$1.06\times10^{-2}\pm1.0\times10^{-3}$
2.65	$2.01\times10^{-2}\pm2.1\times10^{-3}$	$1.68\times10^{-2}\pm1.4\times10^{-3}$	$1.30\times10^{-2}\pm1.2\times10^{-3}$	$8.20\times10^{-3}\pm9.1\times10^{-4}$
2.75	$1.57\times10^{-2}\pm1.9\times10^{-3}$	$1.35\times10^{-2}\pm1.3\times10^{-3}$	$1.06\times10^{-2}\pm1.1\times10^{-3}$	$6.35\times10^{-3}\pm8.5\times10^{-4}$
2.85	$1.30\times10^{-2}\pm1.9\times10^{-3}$	$1.03\times10^{-2}\pm1.2\times10^{-3}$	$8.61\times10^{-3}\pm1.1\times10^{-3}$	$5.10\times10^{-3}\pm8.3\times10^{-4}$
2.95	$9.44\times10^{-3}\pm1.7\times10^{-3}$	$8.45\times10^{-3}\pm1.2\times10^{-3}$	$6.16\times10^{-3}\pm9.8\times10^{-4}$	$3.72\times10^{-3}\pm7.5\times10^{-4}$

TABLE XV. Invariant yields for π^- at midrapidity in 50–60%, 60–70%, 70–80%, and 80–92% centrality bins, normalized to unit rapidity. Errors are statistical only.

p_T (GeV/c)	50–60%	60–70%	70–80%	80–92%
0.25	$3.92\times10^{1}\pm3.1\times10^{-1}$	$2.07\times10^{1}\pm1.7\times10^{-1}$	$9.77\times10^{0}\pm8.2\times10^{-2}$	$5.03\times10^{0}\pm4.5\times10^{-2}$
0.35	$2.10\times10^{1}\pm1.7\times10^{-1}$	$1.09\times10^{1}\pm9.0\times10^{-2}$	$5.19\times10^{0}\pm4.6\times10^{-2}$	$2.67\times10^{0}\pm2.6\times10^{-2}$
0.45	$1.21\times10^{1}\pm1.0\times10^{-1}$	$6.21\times10^{0}\pm5.5\times10^{-2}$	$2.84\times10^{0}\pm2.8\times10^{-2}$	$1.45\times10^{0}\pm1.6\times10^{-2}$
0.55	$7.13\times10^{0}\pm6.6\times10^{-2}$	$3.59\times10^{0}\pm3.5\times10^{-2}$	$1.62\times10^{0}\pm1.8\times10^{-2}$	$8.13\times10^{-1}\pm1.1\times10^{-2}$
0.65	$4.30\times10^{0}\pm4.4\times10^{-2}$	$2.16\times10^{0}\pm2.4\times10^{-2}$	$9.32\times10^{-1}\pm1.2\times10^{-2}$	$4.54\times10^{-1}\pm7.3\times10^{-3}$
0.75	$2.61\times10^{0}\pm2.9\times10^{-2}$	$1.30\times10^{0}\pm1.6\times10^{-2}$	$5.61\times10^{-1}\pm8.6\times10^{-3}$	$2.70\times10^{-1}\pm5.3\times10^{-3}$
0.85	$1.68\times10^{0}\pm2.1\times10^{-2}$	$8.30\times10^{-1}\pm1.2\times10^{-2}$	$3.52\times10^{-1}\pm6.4\times10^{-3}$	$1.59\times10^{-1}\pm3.9\times10^{-3}$
0.95	$1.10\times10^{0}\pm1.5\times10^{-2}$	$5.26\times10^{-1}\pm8.7\times10^{-3}$	$2.27\times10^{-1}\pm5.0\times10^{-3}$	$1.07\times10^{-1}\pm3.2\times10^{-3}$
1.05	$7.13\times10^{-1}\pm1.1\times10^{-2}$	$3.45\times10^{-1}\pm6.6\times10^{-3}$	$1.41\times10^{-1}\pm3.8\times10^{-3}$	$6.63\times10^{-2}\pm2.4\times10^{-3}$
1.15	$4.88\times10^{-1}\pm8.8\times10^{-3}$	$2.32\times10^{-1}\pm5.2\times10^{-3}$	$9.75\times10^{-2}\pm3.1\times10^{-3}$	$4.46\times10^{-2}\pm2.0\times10^{-3}$
1.25	$3.12\times10^{-1}\pm6.3\times10^{-3}$	$1.47\times10^{-1}\pm3.8\times10^{-3}$	$6.31\times10^{-2}\pm2.4\times10^{-3}$	$2.65\times10^{-2}\pm1.5\times10^{-3}$
1.35	$2.29\times10^{-1}\pm5.3\times10^{-3}$	$1.05\times10^{-1}\pm3.2\times10^{-3}$	$4.17\times10^{-2}\pm1.9\times10^{-3}$	$2.02\times10^{-2}\pm1.3\times10^{-3}$
1.45	$1.51\times10^{-1}\pm4.1\times10^{-3}$	$7.32\times10^{-2}\pm2.6\times10^{-3}$	$2.81\times10^{-2}\pm1.6\times10^{-3}$	$1.28\times10^{-2}\pm1.0\times10^{-3}$
1.55	$1.10\times10^{-1}\pm3.4\times10^{-3}$	$5.15\times10^{-2}\pm2.2\times10^{-3}$	$2.11\times10^{-2}\pm1.4\times10^{-3}$	$9.27\times10^{-3}\pm8.8\times10^{-4}$
1.65	$7.11\times10^{-2}\pm2.6\times10^{-3}$	$3.83\times10^{-2}\pm1.8\times10^{-3}$	$1.53\times10^{-2}\pm1.1\times10^{-3}$	$6.56\times10^{-3}\pm7.3\times10^{-4}$
1.75	$5.38\times10^{-2}\pm2.2\times10^{-3}$	$2.51\times10^{-2}\pm1.4\times10^{-3}$	$1.08\times10^{-2}\pm9.5\times10^{-4}$	$5.14\times10^{-3}\pm6.5\times10^{-4}$
1.85	$4.00\times10^{-2}\pm1.9\times10^{-3}$	$1.87\times10^{-2}\pm1.2\times10^{-3}$	$8.06\times10^{-3}\pm8.2\times10^{-4}$	$3.51\times10^{-3}\pm5.3\times10^{-4}$
1.95	$2.88\times10^{-2}\pm1.6\times10^{-3}$	$1.30\times10^{-2}\pm1.1\times10^{-3}$	$6.03\times10^{-3}\pm7.3\times10^{-4}$	$2.70\times10^{-3}\pm4.8\times10^{-4}$
2.05	$2.04\times10^{-2}\pm1.2\times10^{-3}$	$8.63\times10^{-3}\pm7.4\times10^{-4}$	$4.23\times10^{-3}\pm5.3\times10^{-4}$	$1.40\times10^{-3}\pm3.0\times10^{-4}$
2.15	$1.53\times10^{-2}\pm1.0\times10^{-3}$	$6.88\times10^{-3}\pm6.7\times10^{-4}$	$3.17\times10^{-3}\pm4.6\times10^{-4}$	$1.25\times10^{-3}\pm2.9\times10^{-4}$
2.25	$1.08\times10^{-2}\pm8.8\times10^{-4}$	$4.71\times10^{-3}\pm5.7\times10^{-4}$	$1.89\times10^{-3}\pm3.7\times10^{-4}$	$8.66\times10^{-4}\pm2.5\times10^{-4}$
2.35	$8.95\times10^{-3}\pm8.4\times10^{-4}$	$4.42\times10^{-3}\pm5.8\times10^{-4}$	$1.96\times10^{-3}\pm4.0\times10^{-4}$	$6.65\times10^{-4}\pm2.3\times10^{-4}$
2.45	$7.17\times10^{-3}\pm7.6\times10^{-4}$	$3.04\times10^{-3}\pm4.9\times10^{-4}$	$1.17\times10^{-3}\pm3.1\times10^{-4}$	$5.61\times10^{-4}\pm2.1\times10^{-4}$
2.55	$5.72\times10^{-3}\pm7.5\times10^{-4}$	$2.96\times10^{-3}\pm5.3\times10^{-4}$	$1.16\times10^{-3}\pm3.4\times10^{-4}$	$3.79\times10^{-4}\pm1.9\times10^{-4}$
2.65	$4.94\times10^{-3}\pm7.1\times10^{-4}$	$2.21\times10^{-3}\pm4.7\times10^{-4}$	$8.05\times10^{-4}\pm2.9\times10^{-4}$	$4.14\times10^{-4}\pm2.0\times10^{-4}$
2.75	$3.43\times10^{-3}\pm6.3\times10^{-4}$	$1.54\times10^{-3}\pm4.2\times10^{-4}$	$3.78\times10^{-4}\pm2.1\times10^{-4}$	$3.34\times10^{-4}\pm2.0\times10^{-4}$
2.85	$2.67\times10^{-3}\pm6.0\times10^{-4}$	$1.24\times10^{-3}\pm4.1\times10^{-4}$	$2.87\times10^{-4}\pm2.0\times10^{-4}$	$2.85\times10^{-4}\pm2.0\times10^{-4}$
2.95	$1.73\times10^{-3}\pm5.1\times10^{-4}$	$1.25\times10^{-3}\pm4.3\times10^{-4}$	$6.75\times10^{-4}\pm3.2\times10^{-4}$	$2.04\times10^{-4}\pm1.8\times10^{-4}$

TABLE XVI. Invariant yields for K^+ at midrapidity in the minimum bias, 0–5%, 5–10%, and 10–15% centrality bins, normalized to unit rapidity. Errors are statistical only.

p_T (GeV/c)	Minimum bias	0–5%	5–10%	10–15%
0.45	$5.46\times10^{0}\pm1.1\times10^{-1}$	$1.83\times10^{1}\pm3.9\times10^{-1}$	$1.50\times10^{1}\pm3.3\times10^{-1}$	$1.29\times10^{1}\pm2.8\times10^{-1}$
0.55	$4.28\times10^{0}\pm7.8\times10^{-2}$	$1.48\times10^{1}\pm2.9\times10^{-1}$	$1.20\times10^{1}\pm2.4\times10^{-1}$	$9.88\times10^{0}\pm2.0\times10^{-1}$
0.65	$3.11\times10^{0}\pm5.4\times10^{-2}$	$1.05\times10^{1}\pm2.0\times10^{-1}$	$8.75\times10^{0}\pm1.7\times10^{-1}$	$7.38\times10^{0}\pm1.4\times10^{-1}$
0.75	$2.27\times10^{0}\pm3.9\times10^{-2}$	$7.97\times10^{0}\pm1.5\times10^{-1}$	$6.48\times10^{0}\pm1.2\times10^{-1}$	$5.39\times10^{0}\pm1.0\times10^{-1}$
0.85	$1.69\times10^{0}\pm3.0\times10^{-2}$	$5.96\times10^{0}\pm1.2\times10^{-1}$	$4.81\times10^{0}\pm9.5\times10^{-2}$	$4.02\times10^{0}\pm8.1\times10^{-2}$
0.95	$1.20\times10^{0}\pm2.2\times10^{-2}$	$4.19\times10^{0}\pm8.5\times10^{-2}$	$3.47\times10^{0}\pm7.2\times10^{-2}$	$2.91\times10^{0}\pm6.1\times10^{-2}$
1.05	$9.06\times10^{-1}\pm1.7\times10^{-2}$	$3.20\times10^{0}\pm6.8\times10^{-2}$	$2.61\times10^{0}\pm5.7\times10^{-2}$	$2.21\times10^{0}\pm5.0\times10^{-2}$
1.15	$6.57\times10^{-1}\pm1.3\times10^{-2}$	$2.31\times10^{0}\pm5.2\times10^{-2}$	$1.91\times10^{0}\pm4.4\times10^{-2}$	$1.63\times10^{0}\pm3.9\times10^{-2}$
1.25	$4.55\times10^{-1}\pm8.9\times10^{-3}$	$1.64\times10^{0}\pm3.9\times10^{-2}$	$1.32\times10^{0}\pm3.3\times10^{-2}$	$1.14\times10^{0}\pm2.9\times10^{-2}$
1.35	$3.24\times10^{-1}\pm6.5\times10^{-3}$	$1.13\times10^{0}\pm2.9\times10^{-2}$	$9.63\times10^{-1}\pm2.5\times10^{-2}$	$7.88\times10^{-1}\pm2.2\times10^{-2}$
1.45	$2.43\times10^{-1}\pm5.1\times10^{-3}$	$8.52\times10^{-1}\pm2.4\times10^{-2}$	$7.33\times10^{-1}\pm2.1\times10^{-2}$	$6.05\times10^{-1}\pm1.8\times10^{-2}$
1.55	$1.76\times10^{-1}\pm3.8\times10^{-3}$	$6.03\times10^{-1}\pm1.8\times10^{-2}$	$5.16\times10^{-1}\pm1.6\times10^{-2}$	$4.33\times10^{-1}\pm1.4\times10^{-2}$
1.65	$1.27\times10^{-1}\pm2.9\times10^{-3}$	$4.43\times10^{-1}\pm1.5\times10^{-2}$	$3.84\times10^{-1}\pm1.3\times10^{-2}$	$3.04\times10^{-1}\pm1.1\times10^{-2}$
1.75	$9.47\times10^{-2}\pm2.3\times10^{-3}$	$3.61\times10^{-1}\pm1.3\times10^{-2}$	$2.76\times10^{-1}\pm1.1\times10^{-2}$	$2.28\times10^{-1}\pm9.3\times10^{-3}$
1.85	$7.24\times10^{-2}\pm1.8\times10^{-3}$	$2.64\times10^{-1}\pm1.0\times10^{-2}$	$2.17\times10^{-1}\pm9.0\times10^{-3}$	$1.72\times10^{-1}\pm7.7\times10^{-3}$
1.95	$5.67\times10^{-2}\pm1.5\times10^{-3}$	$2.12\times10^{-1}\pm9.1\times10^{-3}$	$1.67\times10^{-1}\pm7.8\times10^{-3}$	$1.37\times10^{-1}\pm6.9\times10^{-3}$

TABLE XVII. Invariant yields for K^+ at midrapidity in 15–20%, 20–30%, 30–40%, and 40–50% centrality bins, normalized to unit rapidity. Errors are statistical only.

p_T (GeV/c)	15–20%	20–30%	30–40%	40–50%
0.45	$1.04\times10^{1}\pm2.3\times10^{-1}$	$7.81\times10^{0}\pm1.7\times10^{-1}$	$5.11\times10^{0}\pm1.1\times10^{-1}$	$3.28\times10^{0}\pm7.8\times10^{-2}$
0.55	$8.30\times10^{0}\pm1.7\times10^{-1}$	$6.22\times10^{0}\pm1.2\times10^{-1}$	$4.06\times10^{0}\pm8.3\times10^{-2}$	$2.43\times10^{0}\pm5.3\times10^{-2}$
0.65	$6.20\times10^{0}\pm1.2\times10^{-1}$	$4.51\times10^{0}\pm8.5\times10^{-2}$	$2.89\times10^{0}\pm5.7\times10^{-2}$	$1.78\times10^{0}\pm3.8\times10^{-2}$
0.75	$4.46\times10^{0}\pm8.8\times10^{-2}$	$3.31\times10^{0}\pm6.2\times10^{-2}$	$2.07\times10^{0}\pm4.1\times10^{-2}$	$1.26\times10^{0}\pm2.7\times10^{-2}$
0.85	$3.36\times10^{0}\pm7.0\times10^{-2}$	$2.50\times10^{0}\pm4.9\times10^{-2}$	$1.60\times10^{0}\pm3.3\times10^{-2}$	$9.00\times10^{-1}\pm2.1\times10^{-2}$
0.95	$2.40\times10^{0}\pm5.2\times10^{-2}$	$1.74\times10^{0}\pm3.6\times10^{-2}$	$1.08\times10^{0}\pm2.4\times10^{-2}$	$6.46\times10^{-1}\pm1.6\times10^{-2}$
1.05	$1.81\times10^{0}\pm4.2\times10^{-2}$	$1.31\times10^{0}\pm2.8\times10^{-2}$	$8.42\times10^{-1}\pm2.0\times10^{-2}$	$4.82\times10^{-1}\pm1.3\times10^{-2}$
1.15	$1.29\times10^{0}\pm3.2\times10^{-2}$	$9.60\times10^{-1}\pm2.2\times10^{-2}$	$6.01\times10^{-1}\pm1.5\times10^{-2}$	$3.48\times10^{-1}\pm1.0\times10^{-2}$
1.25	$8.82\times10^{-1}\pm2.4\times10^{-2}$	$6.54\times10^{-1}\pm1.6\times10^{-2}$	$4.22\times10^{-1}\pm1.1\times10^{-2}$	$2.34\times10^{-1}\pm7.5\times10^{-3}$
1.35	$6.60\times10^{-1}\pm1.9\times10^{-2}$	$4.68\times10^{-1}\pm1.2\times10^{-2}$	$2.99\times10^{-1}\pm8.7\times10^{-3}$	$1.70\times10^{-1}\pm5.9\times10^{-3}$
1.45	$4.91\times10^{-1}\pm1.5\times10^{-2}$	$3.50\times10^{-1}\pm9.9\times10^{-3}$	$2.22\times10^{-1}\pm7.2\times10^{-3}$	$1.20\times10^{-1}\pm4.8\times10^{-3}$
1.55	$3.55\times10^{-1}\pm1.2\times10^{-2}$	$2.59\times10^{-1}\pm7.9\times10^{-3}$	$1.63\times10^{-1}\pm5.8\times10^{-3}$	$9.25\times10^{-2}\pm4.0\times10^{-3}$
1.65	$2.62\times10^{-1}\pm1.0\times10^{-2}$	$1.88\times10^{-1}\pm6.3\times10^{-3}$	$1.14\times10^{-1}\pm4.6\times10^{-3}$	$6.22\times10^{-2}\pm3.1\times10^{-3}$
1.75	$1.92\times10^{-1}\pm8.3\times10^{-3}$	$1.34\times10^{-1}\pm5.1\times10^{-3}$	$8.52\times10^{-2}\pm3.8\times10^{-3}$	$4.81\times10^{-2}\pm2.7\times10^{-3}$
1.85	$1.48\times10^{-1}\pm7.0\times10^{-3}$	$1.04\times10^{-1}\pm4.2\times10^{-3}$	$6.58\times10^{-2}\pm3.2\times10^{-3}$	$3.66\times10^{-2}\pm2.3\times10^{-3}$
1.95	$1.14\times10^{-1}\pm6.1\times10^{-3}$	$8.21\times10^{-2}\pm3.7\times10^{-3}$	$4.87\times10^{-2}\pm2.7\times10^{-3}$	$2.91\times10^{-2}\pm2.0\times10^{-3}$

TABLE XVIII. Invariant yields for K^+ at midrapidity in 50–60%, 60–70%, 70–80%, and 80–92% centrality bins, normalized to unit rapidity. Errors are statistical only.

p_T (GeV/c)	50–60%	60–70%	70–80%	80–92%
0.45	$1.93\times10^{0}\pm5.0\times10^{-2}$	$9.56\times10^{-1}\pm2.9\times10^{-2}$	$4.06\times10^{-1}\pm1.7\times10^{-2}$	$1.88\times10^{-1}\pm1.1\times10^{-2}$
0.55	$1.36\times10^{0}\pm3.3\times10^{-2}$	$6.72\times10^{-1}\pm2.0\times10^{-2}$	$2.89\times10^{-1}\pm1.2\times10^{-2}$	$1.48\times10^{-1}\pm7.8\times10^{-3}$
0.65	$1.01\times10^{0}\pm2.4\times10^{-2}$	$4.81\times10^{-1}\pm1.4\times10^{-2}$	$1.88\times10^{-1}\pm8.0\times10^{-3}$	$1.02\times10^{-1}\pm5.6\times10^{-3}$
0.75	$6.82\times10^{-1}\pm1.7\times10^{-2}$	$3.40\times10^{-1}\pm1.1\times10^{-2}$	$1.24\times10^{-1}\pm5.8\times10^{-3}$	$5.88\times10^{-2}\pm3.9\times10^{-3}$
0.85	$4.77\times10^{-1}\pm1.3\times10^{-2}$	$2.33\times10^{-1}\pm8.1\times10^{-3}$	$9.39\times10^{-2}\pm4.8\times10^{-3}$	$3.87\times10^{-2}\pm3.0\times10^{-3}$
0.95	$3.51\times10^{-1}\pm1.0\times10^{-2}$	$1.69\times10^{-1}\pm6.4\times10^{-3}$	$5.66\times10^{-2}\pm3.5\times10^{-3}$	$2.99\times10^{-2}\pm2.5\times10^{-3}$
1.05	$2.54\times10^{-1}\pm8.2\times10^{-3}$	$1.19\times10^{-1}\pm5.1\times10^{-3}$	$4.40\times10^{-2}\pm3.0\times10^{-3}$	$2.07\times10^{-2}\pm2.0\times10^{-3}$
1.15	$1.80\times10^{-1}\pm6.4\times10^{-3}$	$7.84\times10^{-2}\pm3.9\times10^{-3}$	$3.12\times10^{-2}\pm2.4\times10^{-3}$	$1.64\times10^{-2}\pm1.7\times10^{-3}$
1.25	$1.28\times10^{-1}\pm5.1\times10^{-3}$	$5.43\times10^{-2}\pm3.1\times10^{-3}$	$2.07\times10^{-2}\pm1.9\times10^{-3}$	$7.94\times10^{-3}\pm1.1\times10^{-3}$
1.35	$8.53\times10^{-2}\pm3.9\times10^{-3}$	$3.85\times10^{-2}\pm2.5\times10^{-3}$	$1.38\times10^{-2}\pm1.5\times10^{-3}$	$6.53\times10^{-3}\pm9.9\times10^{-4}$
1.45	$6.40\times10^{-2}\pm3.3\times10^{-3}$	$2.94\times10^{-2}\pm2.1\times10^{-3}$	$1.34\times10^{-2}\pm1.4\times10^{-3}$	$5.70\times10^{-3}\pm9.2\times10^{-4}$
1.55	$4.73\times10^{-2}\pm2.7\times10^{-3}$	$2.10\times10^{-2}\pm1.8\times10^{-3}$	$6.85\times10^{-3}\pm1.0\times10^{-3}$	$2.84\times10^{-3}\pm6.4\times10^{-4}$
1.65	$3.39\times10^{-2}\pm2.2\times10^{-3}$	$1.60\times10^{-2}\pm1.5\times10^{-3}$	$5.62\times10^{-3}\pm8.9\times10^{-4}$	$2.67\times10^{-3}\pm6.1\times10^{-4}$
1.75	$2.31\times10^{-2}\pm1.8\times10^{-3}$	$1.04\times10^{-2}\pm1.2\times10^{-3}$	$4.19\times10^{-3}\pm7.6\times10^{-4}$	$1.85\times10^{-3}\pm5.0\times10^{-4}$
1.85	$1.72\times10^{-2}\pm1.5\times10^{-3}$	$8.75\times10^{-3}\pm1.1\times10^{-3}$	$3.39\times10^{-3}\pm6.7\times10^{-4}$	$2.09\times10^{-3}\pm5.2\times10^{-4}$
1.95	$1.53\times10^{-2}\pm1.4\times10^{-3}$	$6.49\times10^{-3}\pm9.2\times10^{-4}$	$2.75\times10^{-3}\pm6.1\times10^{-4}$	$1.16\times10^{-3}\pm3.9\times10^{-4}$

TABLE XIX. Invariant yields for K^- at midrapidity in the minimum bias, 0–5%, 5–10%, and 10–15% centrality bins, normalized to unit rapidity. Errors are statistical only.

p_T (GeV/c)	Minimum bias	0–5%	5–10%	10–15%
0.45	$4.87\times10^{0}\pm9.3\times10^{-2}$	$1.64\times10^{1}\pm3.4\times10^{-1}$	$1.36\times10^{1}\pm2.8\times10^{-1}$	$1.12\times10^{1}\pm2.4\times10^{-1}$
0.55	$3.88\times10^{0}\pm6.7\times10^{-2}$	$1.31\times10^{1}\pm2.4\times10^{-1}$	$1.09\times10^{1}\pm2.0\times10^{-1}$	$8.91\times10^{0}\pm1.7\times10^{-1}$
0.65	$2.96\times10^{0}\pm4.9\times10^{-2}$	$1.01\times10^{1}\pm1.8\times10^{-1}$	$8.57\times10^{0}\pm1.5\times10^{-1}$	$6.94\times10^{0}\pm1.3\times10^{-1}$
0.75	$2.20\times10^{0}\pm3.6\times10^{-2}$	$7.69\times10^{0}\pm1.4\times10^{-1}$	$6.27\times10^{0}\pm1.1\times10^{-1}$	$5.14\times10^{0}\pm9.5\times10^{-2}$
0.85	$1.59\times10^{0}\pm2.6\times10^{-2}$	$5.61\times10^{0}\pm1.0\times10^{-1}$	$4.55\times10^{0}\pm8.4\times10^{-2}$	$3.82\times10^{0}\pm7.2\times10^{-2}$
0.95	$1.14\times10^{0}\pm1.9\times10^{-2}$	$4.11\times10^{0}\pm7.7\times10^{-2}$	$3.36\times10^{0}\pm6.5\times10^{-2}$	$2.76\times10^{0}\pm5.4\times10^{-2}$
1.05	$8.50\times10^{-1}\pm1.5\times10^{-2}$	$3.03\times10^{0}\pm6.0\times10^{-2}$	$2.53\times10^{0}\pm5.2\times10^{-2}$	$2.05\times10^{0}\pm4.3\times10^{-2}$
1.15	$5.96\times10^{-1}\pm1.0\times10^{-2}$	$2.11\times10^{0}\pm4.4\times10^{-2}$	$1.79\times10^{0}\pm3.8\times10^{-2}$	$1.44\times10^{0}\pm3.2\times10^{-2}$
1.25	$4.29\times10^{-1}\pm7.8\times10^{-3}$	$1.53\times10^{0}\pm3.4\times10^{-2}$	$1.25\times10^{0}\pm2.9\times10^{-2}$	$1.05\times10^{0}\pm2.5\times10^{-2}$
1.35	$3.23\times10^{-1}\pm6.2\times10^{-3}$	$1.15\times10^{0}\pm2.8\times10^{-2}$	$9.45\times10^{-1}\pm2.4\times10^{-2}$	$8.03\times10^{-1}\pm2.1\times10^{-2}$
1.45	$2.32\times10^{-1}\pm4.6\times10^{-3}$	$8.42\times10^{-1}\pm2.2\times10^{-2}$	$6.97\times10^{-1}\pm1.9\times10^{-2}$	$5.62\times10^{-1}\pm1.6\times10^{-2}$
1.55	$1.67\times10^{-1}\pm3.4\times10^{-3}$	$5.86\times10^{-1}\pm1.7\times10^{-2}$	$4.97\times10^{-1}\pm1.5\times10^{-2}$	$4.16\times10^{-1}\pm1.3\times10^{-2}$
1.65	$1.21\times10^{-1}\pm2.6\times10^{-3}$	$4.42\times10^{-1}\pm1.4\times10^{-2}$	$3.82\times10^{-1}\pm1.2\times10^{-2}$	$2.93\times10^{-1}\pm1.0\times10^{-2}$
1.75	$8.78\times10^{-2}\pm2.0\times10^{-3}$	$3.17\times10^{-1}\pm1.1\times10^{-2}$	$2.64\times10^{-1}\pm9.6\times10^{-3}$	$2.11\times10^{-1}\pm8.2\times10^{-3}$
1.85	$6.76\times10^{-2}\pm1.6\times10^{-3}$	$2.52\times10^{-1}\pm9.4\times10^{-3}$	$2.10\times10^{-1}\pm8.4\times10^{-3}$	$1.61\times10^{-1}\pm7.0\times10^{-3}$
1.95	$5.10\times10^{-2}\pm1.3\times10^{-3}$	$1.83\times10^{-1}\pm7.9\times10^{-3}$	$1.53\times10^{-1}\pm7.1\times10^{-3}$	$1.22\times10^{-1}\pm6.1\times10^{-3}$

TABLE XX. Invariant yields for K^- at midrapidity in 15–20%, 20–30%, 30–40%, and 40–50% centrality bins, normalized to unit rapidity. Errors are statistical only.

p_T (GeV/c)	15–20%	20–30%	30–40%	40–50%
0.45	$9.24\times10^{0}\pm2.0\times10^{-1}$	$7.05\times10^{0}\pm1.5\times10^{-1}$	$4.60\times10^{0}\pm9.9\times10^{-2}$	$2.79\times10^{0}\pm6.4\times10^{-2}$
0.55	$7.61\times10^{0}\pm1.5\times10^{-1}$	$5.62\times10^{0}\pm1.0\times10^{-1}$	$3.68\times10^{0}\pm7.1\times10^{-2}$	$2.25\times10^{0}\pm4.7\times10^{-2}$
0.65	$5.78\times10^{0}\pm1.1\times10^{-1}$	$4.29\times10^{0}\pm7.7\times10^{-2}$	$2.74\times10^{0}\pm5.1\times10^{-2}$	$1.69\times10^{0}\pm3.4\times10^{-2}$
0.75	$4.33\times10^{0}\pm8.1\times10^{-2}$	$3.22\times10^{0}\pm5.8\times10^{-2}$	$2.04\times10^{0}\pm3.8\times10^{-2}$	$1.19\times10^{0}\pm2.5\times10^{-2}$
0.85	$3.13\times10^{0}\pm6.0\times10^{-2}$	$2.29\times10^{0}\pm4.2\times10^{-2}$	$1.49\times10^{0}\pm2.9\times10^{-2}$	$8.47\times10^{-1}\pm1.8\times10^{-2}$
0.95	$2.23\times10^{0}\pm4.5\times10^{-2}$	$1.61\times10^{0}\pm3.1\times10^{-2}$	$1.04\times10^{0}\pm2.1\times10^{-2}$	$6.04\times10^{-1}\pm1.4\times10^{-2}$
1.05	$1.70\times10^{0}\pm3.7\times10^{-2}$	$1.21\times10^{0}\pm2.5\times10^{-2}$	$7.74\times10^{-1}\pm1.7\times10^{-2}$	$4.49\times10^{-1}\pm1.1\times10^{-2}$
1.15	$1.17\times10^{0}\pm2.7\times10^{-2}$	$8.78\times10^{-1}\pm1.9\times10^{-2}$	$5.39\times10^{-1}\pm1.3\times10^{-2}$	$3.11\times10^{-1}\pm8.4\times10^{-3}$
1.25	$8.58\times10^{-1}\pm2.1\times10^{-2}$	$6.29\times10^{-1}\pm1.4\times10^{-2}$	$3.87\times10^{-1}\pm9.9\times10^{-3}$	$2.25\times10^{-1}\pm6.8\times10^{-3}$
1.35	$6.26\times10^{-1}\pm1.7\times10^{-2}$	$4.76\times10^{-1}\pm1.2\times10^{-2}$	$2.97\times10^{-1}\pm8.3\times10^{-3}$	$1.64\times10^{-1}\pm5.5\times10^{-3}$
1.45	$4.56\times10^{-1}\pm1.4\times10^{-2}$	$3.41\times10^{-1}\pm9.2\times10^{-3}$	$2.09\times10^{-1}\pm6.5\times10^{-3}$	$1.21\times10^{-1}\pm4.5\times10^{-3}$
1.55	$3.25\times10^{-1}\pm1.1\times10^{-2}$	$2.50\times10^{-1}\pm7.3\times10^{-3}$	$1.43\times10^{-1}\pm5.0\times10^{-3}$	$8.71\times10^{-2}\pm3.7\times10^{-3}$
1.65	$2.36\times10^{-1}\pm8.9\times10^{-3}$	$1.72\times10^{-1}\pm5.7\times10^{-3}$	$1.07\times10^{-1}\pm4.2\times10^{-3}$	$6.17\times10^{-2}\pm3.0\times10^{-3}$
1.75	$1.83\times10^{-1}\pm7.4\times10^{-3}$	$1.29\times10^{-1}\pm4.6\times10^{-3}$	$7.79\times10^{-2}\pm3.4\times10^{-3}$	$4.42\times10^{-2}\pm2.4\times10^{-3}$
1.85	$1.29\times10^{-1}\pm6.0\times10^{-3}$	$1.01\times10^{-1}\pm4.0\times10^{-3}$	$5.84\times10^{-2}\pm2.8\times10^{-3}$	$3.24\times10^{-2}\pm2.0\times10^{-3}$
1.95	$1.05\times10^{-1}\pm5.5\times10^{-3}$	$7.67\times10^{-2}\pm3.4\times10^{-3}$	$4.31\times10^{-2}\pm2.4\times10^{-3}$	$2.46\times10^{-2}\pm1.8\times10^{-3}$

TABLE XXI. Invariant yields for K^- at midrapidity in 50–60%, 60–70%, 70–80%, and 80–92% centrality bins, normalized to unit rapidity. Errors are statistical only.

p_T (GeV/c)	50–60%	60–70%	70–80%	80–92%
0.45	$1.73\times10^{0}\pm4.3\times10^{-2}$	$8.11\times10^{-1}\pm2.5\times10^{-2}$	$3.89\times10^{-1}\pm1.6\times10^{-2}$	$1.82\times10^{-1}\pm9.9\times10^{-3}$
0.55	$1.25\times10^{0}\pm2.9\times10^{-2}$	$6.37\times10^{-1}\pm1.8\times10^{-2}$	$2.80\times10^{-1}\pm1.1\times10^{-2}$	$1.37\times10^{-1}\pm7.1\times10^{-3}$
0.65	$9.30\times10^{-1}\pm2.1\times10^{-2}$	$4.43\times10^{-1}\pm1.3\times10^{-2}$	$1.83\times10^{-1}\pm7.5\times10^{-3}$	$1.02\times10^{-1}\pm5.4\times10^{-3}$
0.75	$6.59\times10^{-1}\pm1.6\times10^{-2}$	$3.16\times10^{-1}\pm9.5\times10^{-3}$	$1.40\times10^{-1}\pm5.9\times10^{-3}$	$6.21\times10^{-2}\pm3.8\times10^{-3}$
0.85	$4.65\times10^{-1}\pm1.2\times10^{-2}$	$2.31\times10^{-1}\pm7.4\times10^{-3}$	$8.42\times10^{-2}\pm4.2\times10^{-3}$	$3.81\times10^{-2}\pm2.7\times10^{-3}$
0.95	$3.22\times10^{-1}\pm9.0\times10^{-3}$	$1.56\times10^{-1}\pm5.7\times10^{-3}$	$5.67\times10^{-2}\pm3.2\times10^{-3}$	$2.57\times10^{-2}\pm2.1\times10^{-3}$
1.05	$2.32\times10^{-1}\pm7.2\times10^{-3}$	$1.09\times10^{-1}\pm4.5\times10^{-3}$	$4.26\times10^{-2}\pm2.7\times10^{-3}$	$1.73\times10^{-2}\pm1.7\times10^{-3}$
1.15	$1.60\times10^{-1}\pm5.5\times10^{-3}$	$7.06\times10^{-2}\pm3.4\times10^{-3}$	$2.98\times10^{-2}\pm2.1\times10^{-3}$	$1.32\times10^{-2}\pm1.4\times10^{-3}$
1.25	$1.15\times10^{-1}\pm4.4\times10^{-3}$	$5.72\times10^{-2}\pm2.9\times10^{-3}$	$1.84\times10^{-2}\pm1.6\times10^{-3}$	$9.79\times10^{-3}\pm1.2\times10^{-3}$
1.35	$8.85\times10^{-2}\pm3.8\times10^{-3}$	$3.67\times10^{-2}\pm2.3\times10^{-3}$	$1.59\times10^{-2}\pm1.5\times10^{-3}$	$7.78\times10^{-3}\pm1.0\times10^{-3}$
1.45	$5.83\times10^{-2}\pm3.0\times10^{-3}$	$2.38\times10^{-2}\pm1.8\times10^{-3}$	$1.12\times10^{-2}\pm1.2\times10^{-3}$	$4.22\times10^{-3}\pm7.5\times10^{-4}$
1.55	$4.60\times10^{-2}\pm2.5\times10^{-3}$	$1.89\times10^{-2}\pm1.6\times10^{-3}$	$7.86\times10^{-3}\pm1.0\times10^{-3}$	$3.92\times10^{-3}\pm7.1\times10^{-4}$
1.65	$3.05\times10^{-2}\pm2.0\times10^{-3}$	$1.53\times10^{-2}\pm1.4\times10^{-3}$	$6.44\times10^{-3}\pm9.0\times10^{-4}$	$2.92\times10^{-3}\pm6.0\times10^{-4}$
1.75	$2.07\times10^{-2}\pm1.6\times10^{-3}$	$1.00\times10^{-2}\pm1.1\times10^{-3}$	$3.65\times10^{-3}\pm6.6\times10^{-4}$	$1.27\times10^{-3}\pm3.9\times10^{-4}$
1.85	$1.84\times10^{-2}\pm1.5\times10^{-3}$	$7.82\times10^{-3}\pm9.5\times10^{-4}$	$2.81\times10^{-3}\pm5.8\times10^{-4}$	$1.44\times10^{-3}\pm4.1\times10^{-4}$
1.95	$1.46\times10^{-2}\pm1.3\times10^{-3}$	$6.14\times10^{-3}\pm8.6\times10^{-4}$	$2.12\times10^{-3}\pm5.1\times10^{-4}$	$1.30\times10^{-3}\pm4.0\times10^{-4}$

TABLE XXII. Invariant yields for protons at midrapidity in the minimum bias, 0–5%, 5–10%, and 10–15% centrality bins, normalized to unit rapidity. Errors are statistical only.

p_T (GeV/c)	Minimum bias	0–5%	5–10%	10–15%
0.65	$9.51\times10^{-1}\pm2.7\times10^{-2}$	$2.90\times10^{0}\pm9.3\times10^{-2}$	$2.44\times10^{0}\pm8.0\times10^{-2}$	$2.09\times10^{0}\pm6.9\times10^{-2}$
0.75	$8.47\times10^{-1}\pm2.4\times10^{-2}$	$2.65\times10^{0}\pm8.5\times10^{-2}$	$2.24\times10^{0}\pm7.3\times10^{-2}$	$1.87\times10^{0}\pm6.2\times10^{-2}$
0.85	$7.08\times10^{-1}\pm2.0\times10^{-2}$	$2.28\times10^{0}\pm7.3\times10^{-2}$	$1.91\times10^{0}\pm6.3\times10^{-2}$	$1.60\times10^{0}\pm5.3\times10^{-2}$
0.95	$6.06\times10^{-1}\pm1.8\times10^{-2}$	$2.00\times10^{0}\pm6.6\times10^{-2}$	$1.66\times10^{0}\pm5.5\times10^{-2}$	$1.41\times10^{0}\pm4.8\times10^{-2}$
1.05	$5.05\times10^{-1}\pm1.5\times10^{-2}$	$1.68\times10^{0}\pm5.7\times10^{-2}$	$1.43\times10^{0}\pm4.9\times10^{-2}$	$1.16\times10^{0}\pm4.1\times10^{-2}$
1.15	$4.23\times10^{-1}\pm1.3\times10^{-2}$	$1.46\times10^{0}\pm5.1\times10^{-2}$	$1.22\times10^{0}\pm4.3\times10^{-2}$	$9.85\times10^{-1}\pm3.6\times10^{-2}$
1.25	$3.30\times10^{-1}\pm1.0\times10^{-2}$	$1.16\times10^{0}\pm4.2\times10^{-2}$	$9.51\times10^{-1}\pm3.5\times10^{-2}$	$7.92\times10^{-1}\pm3.0\times10^{-2}$
1.35	$2.71\times10^{-1}\pm8.8\times10^{-3}$	$9.72\times10^{-1}\pm3.7\times10^{-2}$	$7.96\times10^{-1}\pm3.1\times10^{-2}$	$6.55\times10^{-1}\pm2.6\times10^{-2}$
1.45	$2.04\times10^{-1}\pm6.7\times10^{-3}$	$7.42\times10^{-1}\pm2.9\times10^{-2}$	$6.09\times10^{-1}\pm2.5\times10^{-2}$	$5.07\times10^{-1}\pm2.1\times10^{-2}$
1.55	$1.68\times10^{-1}\pm5.8\times10^{-3}$	$6.05\times10^{-1}\pm2.5\times10^{-2}$	$5.08\times10^{-1}\pm2.2\times10^{-2}$	$4.21\times10^{-1}\pm1.9\times10^{-2}$
1.65	$1.25\times10^{-1}\pm4.4\times10^{-3}$	$4.55\times10^{-1}\pm2.0\times10^{-2}$	$3.77\times10^{-1}\pm1.7\times10^{-2}$	$3.02\times10^{-1}\pm1.4\times10^{-2}$
1.75	$9.38\times10^{-2}\pm3.4\times10^{-3}$	$3.51\times10^{-1}\pm1.6\times10^{-2}$	$2.76\times10^{-1}\pm1.4\times10^{-2}$	$2.29\times10^{-1}\pm1.2\times10^{-2}$
1.85	$7.50\times10^{-2}\pm2.8\times10^{-3}$	$2.85\times10^{-1}\pm1.4\times10^{-2}$	$2.28\times10^{-1}\pm1.2\times10^{-2}$	$1.79\times10^{-1}\pm1.0\times10^{-2}$
1.95	$5.37\times10^{-2}\pm2.1\times10^{-3}$	$1.99\times10^{-1}\pm1.1\times10^{-2}$	$1.61\times10^{-1}\pm9.3\times10^{-3}$	$1.36\times10^{-1}\pm8.2\times10^{-3}$
2.10	$3.71\times10^{-2}\pm9.4\times10^{-4}$	$1.35\times10^{-1}\pm5.0\times10^{-3}$	$1.12\times10^{-1}\pm4.4\times10^{-3}$	$9.18\times10^{-2}\pm3.8\times10^{-3}$
2.30	$2.15\times10^{-2}\pm5.9\times10^{-4}$	$7.69\times10^{-2}\pm3.5\times10^{-3}$	$6.73\times10^{-2}\pm3.2\times10^{-3}$	$5.39\times10^{-2}\pm2.7\times10^{-3}$
2.50	$1.21\times10^{-2}\pm4.2\times10^{-4}$	$4.39\times10^{-2}\pm2.5\times10^{-3}$	$3.67\times10^{-2}\pm2.2\times10^{-3}$	$3.05\times10^{-2}\pm2.0\times10^{-3}$
2.70	$7.26\times10^{-3}\pm2.8\times10^{-4}$	$2.44\times10^{-2}\pm1.8\times10^{-3}$	$2.27\times10^{-2}\pm1.7\times10^{-3}$	$1.78\times10^{-2}\pm1.5\times10^{-3}$
2.90	$4.17\times10^{-3}\pm1.9\times10^{-4}$	$1.54\times10^{-2}\pm1.4\times10^{-3}$	$1.16\times10^{-2}\pm1.2\times10^{-3}$	$1.04\times10^{-2}\pm1.1\times10^{-3}$
3.25	$1.70\times10^{-3}\pm8.3\times10^{-5}$	$5.98\times10^{-3}\pm5.5\times10^{-4}$	$5.17\times10^{-3}\pm5.0\times10^{-4}$	$4.04\times10^{-3}\pm4.3\times10^{-4}$
3.75	$5.79\times10^{-4}\pm4.4\times10^{-5}$	$2.05\times10^{-3}\pm3.1\times10^{-4}$	$1.68\times10^{-3}\pm2.8\times10^{-4}$	$1.45\times10^{-3}\pm2.5\times10^{-4}$
4.25	$2.21\times10^{-4}\pm2.7\times10^{-5}$	$8.96\times10^{-4}\pm2.2\times10^{-4}$	$7.04\times10^{-4}\pm1.9\times10^{-4}$	$4.70\times10^{-4}\pm1.5\times10^{-4}$

TABLE XXIII. Invariant yields for protons at midrapidity in 15–20%, 20–30%, 30–40%, and 40–50% centrality bins, normalized to unit rapidity. Errors are statistical only.

p_T (GeV/c)	15–20%	20–30%	30–40%	40–50%
0.65	$1.76\times10^{0}\pm6.0\times10^{-2}$	$1.37\times10^{0}\pm4.4\times10^{-2}$	$9.68\times10^{-1}\pm3.2\times10^{-2}$	$6.31\times10^{-1}\pm2.2\times10^{-2}$
0.75	$1.59\times10^{0}\pm5.4\times10^{-2}$	$1.24\times10^{0}\pm4.0\times10^{-2}$	$8.52\times10^{-1}\pm2.9\times10^{-2}$	$5.39\times10^{-1}\pm1.9\times10^{-2}$
0.85	$1.34\times10^{0}\pm4.6\times10^{-2}$	$1.02\times10^{0}\pm3.3\times10^{-2}$	$7.06\times10^{-1}\pm2.4\times10^{-2}$	$4.33\times10^{-1}\pm1.6\times10^{-2}$
0.95	$1.16\times10^{0}\pm4.1\times10^{-2}$	$8.90\times10^{-1}\pm2.9\times10^{-2}$	$5.79\times10^{-1}\pm2.0\times10^{-2}$	$3.60\times10^{-1}\pm1.4\times10^{-2}$
1.05	$9.75\times10^{-1}\pm3.5\times10^{-2}$	$7.41\times10^{-1}\pm2.5\times10^{-2}$	$4.83\times10^{-1}\pm1.7\times10^{-2}$	$2.96\times10^{-1}\pm1.2\times10^{-2}$
1.15	$8.38\times10^{-1}\pm3.1\times10^{-2}$	$6.27\times10^{-1}\pm2.2\times10^{-2}$	$3.93\times10^{-1}\pm1.5\times10^{-2}$	$2.33\times10^{-1}\pm9.7\times10^{-3}$
1.25	$6.47\times10^{-1}\pm2.5\times10^{-2}$	$4.83\times10^{-1}\pm1.8\times10^{-2}$	$3.09\times10^{-1}\pm1.2\times10^{-2}$	$1.77\times10^{-1}\pm7.9\times10^{-3}$
1.35	$5.35\times10^{-1}\pm2.2\times10^{-2}$	$3.93\times10^{-1}\pm1.5\times10^{-2}$	$2.46\times10^{-1}\pm1.0\times10^{-2}$	$1.40\times10^{-1}\pm6.7\times10^{-3}$
1.45	$4.04\times10^{-1}\pm1.8\times10^{-2}$	$2.90\times10^{-1}\pm1.2\times10^{-2}$	$1.89\times10^{-1}\pm8.3\times10^{-3}$	$1.05\times10^{-1}\pm5.4\times10^{-3}$
1.55	$3.33\times10^{-1}\pm1.6\times10^{-2}$	$2.42\times10^{-1}\pm1.0\times10^{-2}$	$1.49\times10^{-1}\pm7.1\times10^{-3}$	$8.39\times10^{-2}\pm4.7\times10^{-3}$
1.65	$2.60\times10^{-1}\pm1.3\times10^{-2}$	$1.80\times10^{-1}\pm8.1\times10^{-3}$	$1.10\times10^{-1}\pm5.6\times10^{-3}$	$6.02\times10^{-2}\pm3.7\times10^{-3}$
1.75	$1.86\times10^{-1}\pm1.0\times10^{-2}$	$1.36\times10^{-1}\pm6.6\times10^{-3}$	$8.52\times10^{-2}\pm4.7\times10^{-3}$	$4.64\times10^{-2}\pm3.1\times10^{-3}$
1.85	$1.51\times10^{-1}\pm8.9\times10^{-3}$	$1.08\times10^{-1}\pm5.7\times10^{-3}$	$6.68\times10^{-2}\pm4.0\times10^{-3}$	$3.64\times10^{-2}\pm2.7\times10^{-3}$
1.95	$1.06\times10^{-1}\pm6.9\times10^{-3}$	$7.98\times10^{-2}\pm4.5\times10^{-3}$	$4.72\times10^{-2}\pm3.2\times10^{-3}$	$2.53\times10^{-2}\pm2.1\times10^{-3}$
2.10	$7.41\times10^{-2}\pm3.3\times10^{-3}$	$5.63\times10^{-2}\pm2.1\times10^{-3}$	$3.32\times10^{-2}\pm1.5\times10^{-3}$	$1.82\times10^{-2}\pm1.0\times10^{-3}$
2.30	$4.46\times10^{-2}\pm2.4\times10^{-3}$	$3.19\times10^{-2}\pm1.5\times10^{-3}$	$1.96\times10^{-2}\pm1.1\times10^{-3}$	$9.61\times10^{-3}\pm7.2\times10^{-4}$
2.50	$2.52\times10^{-2}\pm1.7\times10^{-3}$	$1.79\times10^{-2}\pm1.1\times10^{-3}$	$1.07\times10^{-2}\pm7.8\times10^{-4}$	$5.83\times10^{-3}\pm5.5\times10^{-4}$
2.70	$1.55\times10^{-2}\pm1.3\times10^{-3}$	$1.08\times10^{-2}\pm8.0\times10^{-4}$	$6.78\times10^{-3}\pm6.1\times10^{-4}$	$3.73\times10^{-3}\pm4.4\times10^{-4}$
2.90	$8.35\times10^{-3}\pm9.5\times10^{-4}$	$6.05\times10^{-3}\pm5.8\times10^{-4}$	$4.10\times10^{-3}\pm4.7\times10^{-4}$	$2.20\times10^{-3}\pm3.3\times10^{-4}$
3.25	$3.51\times10^{-3}\pm3.9\times10^{-4}$	$2.54\times10^{-3}\pm2.4\times10^{-4}$	$1.64\times10^{-3}\pm1.9\times10^{-4}$	$8.36\times10^{-4}\pm1.3\times10^{-4}$
3.75	$1.18\times10^{-3}\pm2.2\times10^{-4}$	$8.20\times10^{-4}\pm1.3\times10^{-4}$	$5.66\times10^{-4}\pm1.1\times10^{-4}$	$3.25\times10^{-4}\pm7.8\times10^{-5}$
4.25	$4.64\times10^{-4}\pm1.4\times10^{-4}$	$3.07\times10^{-4}\pm8.3\times10^{-5}$	$1.93\times10^{-4}\pm6.4\times10^{-5}$	$1.07\times10^{-4}\pm4.7\times10^{-5}$

TABLE XXIV. Invariant yields for protons at midrapidity in 50–60%, 60–70%, 70–80%, and 80–92% centrality bins, normalized to unit rapidity. Errors are statistical only.

p_T (GeV/c)	50–60%	60–70%	70–80%	80–92%
0.65	$3.82\times10^{-1}\pm1.5\times10^{-2}$	$2.04\times10^{-1}\pm9.7\times10^{-3}$	$9.09\times10^{-2}\pm5.9\times10^{-3}$	$4.96\times10^{-2}\pm4.2\times10^{-3}$
0.75	$3.25\times10^{-1}\pm1.3\times10^{-2}$	$1.65\times10^{-1}\pm8.1\times10^{-3}$	$7.04\times10^{-2}\pm4.9\times10^{-3}$	$3.79\times10^{-2}\pm3.4\times10^{-3}$
0.85	$2.60\times10^{-1}\pm1.1\times10^{-2}$	$1.27\times10^{-1}\pm6.5\times10^{-3}$	$5.41\times10^{-2}\pm4.0\times10^{-3}$	$2.62\times10^{-2}\pm2.7\times10^{-3}$
0.95	$2.08\times10^{-1}\pm9.1\times10^{-3}$	$1.00\times10^{-1}\pm5.5\times10^{-3}$	$4.11\times10^{-2}\pm3.3\times10^{-3}$	$2.06\times10^{-2}\pm2.3\times10^{-3}$
1.05	$1.61\times10^{-1}\pm7.5\times10^{-3}$	$7.43\times10^{-2}\pm4.5\times10^{-3}$	$3.14\times10^{-2}\pm2.8\times10^{-3}$	$1.54\times10^{-2}\pm1.9\times10^{-3}$
1.15	$1.24\times10^{-1}\pm6.2\times10^{-3}$	$5.88\times10^{-2}\pm3.8\times10^{-3}$	$2.40\times10^{-2}\pm2.3\times10^{-3}$	$8.08\times10^{-3}\pm1.3\times10^{-3}$
1.25	$9.20\times10^{-2}\pm5.0\times10^{-3}$	$3.98\times10^{-2}\pm3.0\times10^{-3}$	$1.68\times10^{-2}\pm1.9\times10^{-3}$	$6.94\times10^{-3}\pm1.2\times10^{-3}$
1.35	$7.34\times10^{-2}\pm4.4\times10^{-3}$	$3.41\times10^{-2}\pm2.7\times10^{-3}$	$1.21\times10^{-2}\pm1.6\times10^{-3}$	$5.84\times10^{-3}\pm1.1\times10^{-3}$
1.45	$4.98\times10^{-2}\pm3.3\times10^{-3}$	$2.41\times10^{-2}\pm2.2\times10^{-3}$	$9.02\times10^{-3}\pm1.3\times10^{-3}$	$3.61\times10^{-3}\pm8.1\times10^{-4}$
1.55	$4.43\times10^{-2}\pm3.1\times10^{-3}$	$1.69\times10^{-2}\pm1.8\times10^{-3}$	$6.98\times10^{-3}\pm1.1\times10^{-3}$	$2.19\times10^{-3}\pm6.3\times10^{-4}$
1.65	$3.29\times10^{-2}\pm2.6\times10^{-3}$	$1.30\times10^{-2}\pm1.5\times10^{-3}$	$4.57\times10^{-3}\pm9.0\times10^{-4}$	$1.36\times10^{-3}\pm4.8\times10^{-4}$
1.75	$2.37\times10^{-2}\pm2.1\times10^{-3}$	$9.76\times10^{-3}\pm1.3\times10^{-3}$	$3.81\times10^{-3}\pm8.0\times10^{-4}$	$1.40\times10^{-3}\pm4.8\times10^{-4}$
1.85	$1.80\times10^{-2}\pm1.8\times10^{-3}$	$7.16\times10^{-3}\pm1.1\times10^{-3}$	$2.56\times10^{-3}\pm6.6\times10^{-4}$	$8.09\times10^{-4}\pm3.7\times10^{-4}$
1.95	$1.24\times10^{-2}\pm1.4\times10^{-3}$	$5.34\times10^{-3}\pm9.1\times10^{-4}$	$2.04\times10^{-3}\pm5.7\times10^{-4}$	$8.46\times10^{-4}\pm3.6\times10^{-4}$
2.10	$9.33\times10^{-3}\pm7.2\times10^{-4}$	$3.47\times10^{-3}\pm4.2\times10^{-4}$	$1.34\times10^{-3}\pm2.7\times10^{-4}$	$4.08\times10^{-4}\pm1.5\times10^{-4}$
2.30	$4.86\times10^{-3}\pm5.0\times10^{-4}$	$2.28\times10^{-3}\pm3.4\times10^{-4}$	$6.06\times10^{-4}\pm1.8\times10^{-4}$	$2.88\times10^{-4}\pm1.2\times10^{-4}$
2.50	$3.01\times10^{-3}\pm3.9\times10^{-4}$	$9.91\times10^{-4}\pm2.2\times10^{-4}$	$3.91\times10^{-4}\pm1.4\times10^{-4}$	$2.19\times10^{-4}\pm1.0\times10^{-4}$
2.70	$1.66\times10^{-3}\pm2.9\times10^{-4}$	$6.31\times10^{-4}\pm1.7\times10^{-4}$	$2.37\times10^{-4}\pm1.1\times10^{-4}$	$1.12\times10^{-4}\pm7.4\times10^{-5}$
2.90	$1.03\times10^{-3}\pm2.2\times10^{-4}$	$4.62\times10^{-4}\pm1.5\times10^{-4}$	$1.06\times10^{-4}\pm7.3\times10^{-5}$	$3.22\times10^{-5}\pm4.0\times10^{-5}$
3.25	$4.01\times10^{-4}\pm8.7\times10^{-5}$	$1.66\times10^{-4}\pm5.5\times10^{-5}$	$6.73\times10^{-5}\pm3.6\times10^{-5}$	$2.02\times10^{-5}\pm2.0\times10^{-5}$
3.75	$1.45\times10^{-4}\pm5.2\times10^{-5}$	$5.72\times10^{-5}\pm3.2\times10^{-5}$	$2.13\times10^{-5}\pm1.9\times10^{-5}$	$2.89\times10^{-6}\pm7.7\times10^{-6}$
4.25	$4.94\times10^{-5}\pm3.2\times10^{-5}$	$2.40\times10^{-5}\pm2.2\times10^{-5}$	$1.02\times10^{-5}\pm1.5\times10^{-5}$	$2.43\times10^{-6}\pm6.7\times10^{-6}$

TABLE XXV. Invariant yields for antiprotons at midrapidity in the minimum bias, 0–5%, 5–10%, and 10–15% centrality bins, normalized to unit rapidity. Errors are statistical only.

p_T (GeV/c)	Minimum bias	0–5%	5–10%	10–15%
0.65	$6.73\times10^{-1}\pm2.0\times10^{-2}$	$2.00\times10^{0}\pm6.8\times10^{-2}$	$1.73\times10^{0}\pm6.0\times10^{-2}$	$1.48\times10^{0}\pm5.2\times10^{-2}$
0.75	$6.16\times10^{-1}\pm1.8\times10^{-2}$	$1.89\times10^{0}\pm6.2\times10^{-2}$	$1.61\times10^{0}\pm5.4\times10^{-2}$	$1.34\times10^{0}\pm4.6\times10^{-2}$
0.85	$5.28\times10^{-1}\pm1.5\times10^{-2}$	$1.67\times10^{0}\pm5.4\times10^{-2}$	$1.42\times10^{0}\pm4.7\times10^{-2}$	$1.19\times10^{0}\pm4.1\times10^{-2}$
0.95	$4.52\times10^{-1}\pm1.3\times10^{-2}$	$1.47\times10^{0}\pm4.8\times10^{-2}$	$1.25\times10^{0}\pm4.2\times10^{-2}$	$1.05\times10^{0}\pm3.6\times10^{-2}$
1.05	$3.65\times10^{-1}\pm1.1\times10^{-2}$	$1.21\times10^{0}\pm4.1\times10^{-2}$	$1.04\times10^{0}\pm3.6\times10^{-2}$	$8.82\times10^{-1}\pm3.1\times10^{-2}$
1.15	$3.19\times10^{-1}\pm9.7\times10^{-3}$	$1.10\times10^{0}\pm3.9\times10^{-2}$	$9.28\times10^{-1}\pm3.4\times10^{-2}$	$7.39\times10^{-1}\pm2.8\times10^{-2}$
1.25	$2.53\times10^{-1}\pm7.9\times10^{-3}$	$8.90\times10^{-1}\pm3.3\times10^{-2}$	$7.47\times10^{-1}\pm2.8\times10^{-2}$	$6.15\times10^{-1}\pm2.4\times10^{-2}$
1.35	$2.01\times10^{-1}\pm6.5\times10^{-3}$	$7.24\times10^{-1}\pm2.8\times10^{-2}$	$6.08\times10^{-1}\pm2.4\times10^{-2}$	$4.88\times10^{-1}\pm2.0\times10^{-2}$
1.45	$1.66\times10^{-1}\pm5.6\times10^{-3}$	$6.12\times10^{-1}\pm2.5\times10^{-2}$	$5.01\times10^{-1}\pm2.1\times10^{-2}$	$4.09\times10^{-1}\pm1.8\times10^{-2}$
1.55	$1.22\times10^{-1}\pm4.1\times10^{-3}$	$4.43\times10^{-1}\pm1.9\times10^{-2}$	$3.69\times10^{-1}\pm1.6\times10^{-2}$	$3.04\times10^{-1}\pm1.4\times10^{-2}$
1.65	$9.61\times10^{-2}\pm3.4\times10^{-3}$	$3.46\times10^{-1}\pm1.6\times10^{-2}$	$3.00\times10^{-1}\pm1.4\times10^{-2}$	$2.43\times10^{-1}\pm1.2\times10^{-2}$
1.75	$7.19\times10^{-2}\pm2.7\times10^{-3}$	$2.70\times10^{-1}\pm1.3\times10^{-2}$	$2.17\times10^{-1}\pm1.1\times10^{-2}$	$1.84\times10^{-1}\pm9.9\times10^{-3}$
1.85	$5.57\times10^{-2}\pm2.1\times10^{-3}$	$2.07\times10^{-1}\pm1.1\times10^{-2}$	$1.68\times10^{-1}\pm9.5\times10^{-3}$	$1.45\times10^{-1}\pm8.4\times10^{-3}$
1.95	$4.04\times10^{-2}\pm1.7\times10^{-3}$	$1.53\times10^{-1}\pm9.2\times10^{-3}$	$1.19\times10^{-1}\pm7.7\times10^{-3}$	$1.02\times10^{-1}\pm6.9\times10^{-3}$
2.10	$2.61\times10^{-2}\pm7.3\times10^{-4}$	$9.75\times10^{-2}\pm4.2\times10^{-3}$	$7.95\times10^{-2}\pm3.7\times10^{-3}$	$6.64\times10^{-2}\pm3.2\times10^{-3}$
2.30	$1.54\times10^{-2}\pm4.8\times10^{-4}$	$5.99\times10^{-2}\pm3.1\times10^{-3}$	$4.59\times10^{-2}\pm2.7\times10^{-3}$	$3.87\times10^{-2}\pm2.4\times10^{-3}$
2.50	$8.66\times10^{-3}\pm3.4\times10^{-4}$	$3.16\times10^{-2}\pm2.2\times10^{-3}$	$2.69\times10^{-2}\pm2.0\times10^{-3}$	$2.29\times10^{-2}\pm1.8\times10^{-3}$
2.70	$4.79\times10^{-3}\pm2.2\times10^{-4}$	$1.79\times10^{-2}\pm1.6\times10^{-3}$	$1.46\times10^{-2}\pm1.4\times10^{-3}$	$1.19\times10^{-2}\pm1.2\times10^{-3}$
2.90	$2.91\times10^{-3}\pm1.6\times10^{-4}$	$1.04\times10^{-2}\pm1.2\times10^{-3}$	$8.43\times10^{-3}\pm1.1\times10^{-3}$	$7.25\times10^{-3}\pm9.6\times10^{-4}$
3.25	$1.16\times10^{-3}\pm6.7\times10^{-5}$	$4.14\times10^{-3}\pm4.7\times10^{-4}$	$3.55\times10^{-3}\pm4.3\times10^{-4}$	$3.02\times10^{-3}\pm3.8\times10^{-4}$
3.75	$3.71\times10^{-4}\pm3.5\times10^{-5}$	$1.29\times10^{-3}\pm2.5\times10^{-4}$	$1.30\times10^{-3}\pm2.5\times10^{-4}$	$1.09\times10^{-3}\pm2.2\times10^{-4}$
4.25	$1.35\times10^{-4}\pm2.1\times10^{-5}$	$5.44\times10^{-4}\pm1.7\times10^{-4}$	$3.98\times10^{-4}\pm1.4\times10^{-4}$	$3.57\times10^{-4}\pm1.3\times10^{-4}$

TABLE XXVI. Invariant yields for antiprotons at midrapidity in 15–20%, 20–30%, 30–40%, and 40–50% centrality bins, normalized to unit rapidity. Errors are statistical only.

p_T (GeV/c)	15–20%	20–30%	30–40%	40–50%
0.65	$1.25\times10^{0}\pm4.5\times10^{-2}$	$9.68\times10^{-1}\pm3.2\times10^{-2}$	$6.98\times10^{-1}\pm2.4\times10^{-2}$	$4.51\times10^{-1}\pm1.7\times10^{-2}$
0.75	$1.16\times10^{0}\pm4.1\times10^{-2}$	$8.94\times10^{-1}\pm2.9\times10^{-2}$	$6.35\times10^{-1}\pm2.2\times10^{-2}$	$4.06\times10^{-1}\pm1.5\times10^{-2}$
0.85	$1.02\times10^{0}\pm3.5\times10^{-2}$	$7.83\times10^{-1}\pm2.5\times10^{-2}$	$5.21\times10^{-1}\pm1.8\times10^{-2}$	$3.37\times10^{-1}\pm1.3\times10^{-2}$
0.95	$8.85\times10^{-1}\pm3.1\times10^{-2}$	$6.61\times10^{-1}\pm2.2\times10^{-2}$	$4.42\times10^{-1}\pm1.5\times10^{-2}$	$2.70\times10^{-1}\pm1.0\times10^{-2}$
1.05	$7.26\times10^{-1}\pm2.6\times10^{-2}$	$5.25\times10^{-1}\pm1.8\times10^{-2}$	$3.54\times10^{-1}\pm1.3\times10^{-2}$	$2.05\times10^{-1}\pm8.4\times10^{-3}$
1.15	$6.43\times10^{-1}\pm2.5\times10^{-2}$	$4.63\times10^{-1}\pm1.6\times10^{-2}$	$2.99\times10^{-1}\pm1.2\times10^{-2}$	$1.79\times10^{-1}\pm7.7\times10^{-3}$
1.25	$4.99\times10^{-1}\pm2.0\times10^{-2}$	$3.65\times10^{-1}\pm1.4\times10^{-2}$	$2.33\times10^{-1}\pm9.5\times10^{-3}$	$1.37\times10^{-1}\pm6.4\times10^{-3}$
1.35	$4.11\times10^{-1}\pm1.8\times10^{-2}$	$2.88\times10^{-1}\pm1.1\times10^{-2}$	$1.80\times10^{-1}\pm7.8\times10^{-3}$	$1.03\times10^{-1}\pm5.2\times10^{-3}$
1.45	$3.40\times10^{-1}\pm1.5\times10^{-2}$	$2.41\times10^{-1}\pm1.0\times10^{-2}$	$1.42\times10^{-1}\pm6.7\times10^{-3}$	$8.40\times10^{-2}\pm4.6\times10^{-3}$
1.55	$2.45\times10^{-1}\pm1.2\times10^{-2}$	$1.77\times10^{-1}\pm7.8\times10^{-3}$	$1.06\times10^{-1}\pm5.3\times10^{-3}$	$6.14\times10^{-2}\pm3.6\times10^{-3}$
1.65	$1.90\times10^{-1}\pm1.0\times10^{-2}$	$1.43\times10^{-1}\pm6.7\times10^{-3}$	$8.53\times10^{-2}\pm4.6\times10^{-3}$	$4.50\times10^{-2}\pm3.0\times10^{-3}$
1.75	$1.45\times10^{-1}\pm8.4\times10^{-3}$	$1.02\times10^{-1}\pm5.2\times10^{-3}$	$6.32\times10^{-2}\pm3.8\times10^{-3}$	$3.49\times10^{-2}\pm2.6\times10^{-3}$
1.85	$1.20\times10^{-1}\pm7.4\times10^{-3}$	$7.97\times10^{-2}\pm4.4\times10^{-3}$	$4.76\times10^{-2}\pm3.1\times10^{-3}$	$2.66\times10^{-2}\pm2.2\times10^{-3}$
1.95	$8.41\times10^{-2}\pm6.0\times10^{-3}$	$5.83\times10^{-2}\pm3.7\times10^{-3}$	$3.56\times10^{-2}\pm2.7\times10^{-3}$	$1.84\times10^{-2}\pm1.8\times10^{-3}$
2.10	$5.22\times10^{-2}\pm2.8\times10^{-3}$	$3.90\times10^{-2}\pm1.7\times10^{-3}$	$2.30\times10^{-2}\pm1.3\times10^{-3}$	$1.27\times10^{-2}\pm8.8\times10^{-4}$
2.30	$3.19\times10^{-2}\pm2.1\times10^{-3}$	$2.24\times10^{-2}\pm1.2\times10^{-3}$	$1.34\times10^{-2}\pm9.2\times10^{-4}$	$7.39\times10^{-3}\pm6.6\times10^{-4}$
2.50	$1.83\times10^{-2}\pm1.5\times10^{-3}$	$1.22\times10^{-2}\pm9.0\times10^{-4}$	$7.78\times10^{-3}\pm6.9\times10^{-4}$	$4.11\times10^{-3}\pm4.8\times10^{-4}$
2.70	$9.79\times10^{-3}\pm1.1\times10^{-3}$	$6.65\times10^{-3}\pm6.4\times10^{-4}$	$4.66\times10^{-3}\pm5.2\times10^{-4}$	$2.30\times10^{-3}\pm3.5\times10^{-4}$
2.90	$6.28\times10^{-3}\pm8.7\times10^{-4}$	$4.33\times10^{-3}\pm5.1\times10^{-4}$	$2.57\times10^{-3}\pm3.8\times10^{-4}$	$1.67\times10^{-3}\pm3.0\times10^{-4}$
3.25	$2.55\times10^{-3}\pm3.4\times10^{-4}$	$1.64\times10^{-3}\pm2.0\times10^{-4}$	$1.05\times10^{-3}\pm1.5\times10^{-4}$	$5.44\times10^{-4}\pm1.1\times10^{-4}$
3.75	$8.03\times10^{-4}\pm1.9\times10^{-4}$	$5.39\times10^{-4}\pm1.1\times10^{-4}$	$2.59\times10^{-4}\pm7.3\times10^{-5}$	$1.75\times10^{-4}\pm5.9\times10^{-5}$
4.25	$2.92\times10^{-4}\pm1.2\times10^{-4}$	$1.74\times10^{-4}\pm6.3\times10^{-5}$	$1.12\times10^{-4}\pm4.9\times10^{-5}$	$5.56\times10^{-5}\pm3.5\times10^{-5}$

TABLE XXVII. Invariant yields for antiprotons at midrapidity in 50–60%, 60–70%, 70–80%, and 80–92% centrality bins, normalized to unit rapidity. Errors are statistical only.

p_T (GeV/c)	50–60%	60–70%	70–80%	80–92%
0.65	$2.84\times10^{-1}\pm1.2\times10^{-2}$	$1.58\times10^{-1}\pm8.1\times10^{-3}$	$6.22\times10^{-2}\pm4.7\times10^{-3}$	$3.55\times10^{-2}\pm3.4\times10^{-3}$
0.75	$2.50\times10^{-1}\pm1.1\times10^{-2}$	$1.25\times10^{-1}\pm6.6\times10^{-3}$	$5.43\times10^{-2}\pm4.0\times10^{-3}$	$2.77\times10^{-2}\pm2.8\times10^{-3}$
0.85	$1.89\times10^{-1}\pm8.3\times10^{-3}$	$9.50\times10^{-2}\pm5.2\times10^{-3}$	$4.16\times10^{-2}\pm3.3\times10^{-3}$	$2.06\times10^{-2}\pm2.2\times10^{-3}$
0.95	$1.58\times10^{-1}\pm7.1\times10^{-3}$	$7.38\times10^{-2}\pm4.3\times10^{-3}$	$3.13\times10^{-2}\pm2.7\times10^{-3}$	$1.56\times10^{-2}\pm1.8\times10^{-3}$
1.05	$1.19\times10^{-1}\pm5.8\times10^{-3}$	$5.50\times10^{-2}\pm3.5\times10^{-3}$	$2.12\times10^{-2}\pm2.1\times10^{-3}$	$1.01\times10^{-2}\pm1.4\times10^{-3}$
1.15	$9.60\times10^{-2}\pm5.1\times10^{-3}$	$4.34\times10^{-2}\pm3.1\times10^{-3}$	$1.73\times10^{-2}\pm1.9\times10^{-3}$	$7.94\times10^{-3}\pm1.2\times10^{-3}$
1.25	$7.11\times10^{-2}\pm4.1\times10^{-3}$	$3.19\times10^{-2}\pm2.5\times10^{-3}$	$1.22\times10^{-2}\pm1.5\times10^{-3}$	$6.05\times10^{-3}\pm1.1\times10^{-3}$
1.35	$5.31\times10^{-2}\pm3.4\times10^{-3}$	$2.40\times10^{-2}\pm2.1\times10^{-3}$	$9.65\times10^{-3}\pm1.3\times10^{-3}$	$4.08\times10^{-3}\pm8.4\times10^{-4}$
1.45	$4.43\times10^{-2}\pm3.1\times10^{-3}$	$1.90\times10^{-2}\pm1.9\times10^{-3}$	$7.69\times10^{-3}\pm1.2\times10^{-3}$	$3.31\times10^{-3}\pm7.6\times10^{-4}$
1.55	$3.13\times10^{-2}\pm2.4\times10^{-3}$	$1.28\times10^{-2}\pm1.4\times10^{-3}$	$4.43\times10^{-3}\pm8.5\times10^{-4}$	$2.02\times10^{-3}\pm5.6\times10^{-4}$
1.65	$2.39\times10^{-2}\pm2.1\times10^{-3}$	$9.29\times10^{-3}\pm1.2\times10^{-3}$	$3.09\times10^{-3}\pm7.0\times10^{-4}$	$1.70\times10^{-3}\pm5.2\times10^{-4}$
1.75	$1.79\times10^{-2}\pm1.7\times10^{-3}$	$6.92\times10^{-3}\pm1.0\times10^{-3}$	$2.79\times10^{-3}\pm6.6\times10^{-4}$	$1.21\times10^{-3}\pm4.3\times10^{-4}$
1.85	$1.28\times10^{-2}\pm1.4\times10^{-3}$	$5.66\times10^{-3}\pm9.3\times10^{-4}$	$1.27\times10^{-3}\pm4.4\times10^{-4}$	$7.33\times10^{-4}\pm3.3\times10^{-4}$
1.95	$1.00\times10^{-2}\pm1.3\times10^{-3}$	$3.93\times10^{-3}\pm7.8\times10^{-4}$	$1.54\times10^{-3}\pm4.9\times10^{-4}$	$7.92\times10^{-4}\pm3.5\times10^{-4}$
2.10	$6.03\times10^{-3}\pm5.9\times10^{-4}$	$2.58\times10^{-3}\pm3.8\times10^{-4}$	$6.91\times10^{-4}\pm2.0\times10^{-4}$	$3.59\times10^{-4}\pm1.4\times10^{-4}$
2.30	$3.46\times10^{-3}\pm4.4\times10^{-4}$	$1.37\times10^{-3}\pm2.7\times10^{-4}$	$5.66\times10^{-4}\pm1.8\times10^{-4}$	$2.03\times10^{-4}\pm1.1\times10^{-4}$
2.50	$2.04\times10^{-3}\pm3.4\times10^{-4}$	$7.56\times10^{-4}\pm2.0\times10^{-4}$	$2.85\times10^{-4}\pm1.3\times10^{-4}$	$1.35\times10^{-4}\pm8.5\times10^{-5}$
2.70	$1.20\times10^{-3}\pm2.5\times10^{-4}$	$3.92\times10^{-4}\pm1.4\times10^{-4}$	$2.26\times10^{-4}\pm1.1\times10^{-4}$	$2.67\times10^{-5}\pm3.8\times10^{-5}$
2.90	$6.21\times10^{-4}\pm1.8\times10^{-4}$	$2.92\times10^{-4}\pm1.2\times10^{-4}$	$1.40\times10^{-4}\pm8.8\times10^{-5}$	$8.76\times10^{-6}\pm2.2\times10^{-5}$
3.25	$2.61\times10^{-4}\pm7.3\times10^{-5}$	$1.10\times10^{-4}\pm4.7\times10^{-5}$	$3.63\times10^{-5}\pm2.8\times10^{-5}$	$9.16\times10^{-6}\pm1.4\times10^{-5}$
3.75	$6.52\times10^{-5}\pm3.6\times10^{-5}$	$2.77\times10^{-5}\pm2.3\times10^{-5}$	$5.76\times10^{-6}\pm1.1\times10^{-5}$	
4.25	$4.82\times10^{-5}\pm3.2\times10^{-5}$	$1.23\times10^{-5}\pm1.6\times10^{-5}$	$2.71\times10^{-6}\pm8.1\times10^{-6}$	

TABLE XXVIII. Invariant yields for $\pi^{\pm}$ and $K^{\pm}$ at midrapidity in 60–92% centrality bins, normalized to unit rapidity. Errors are statistical only.

p_T (GeV/c)	π^+	π^-	K^+	K^-
0.25	$1.28\times10^{1}\pm1.1\times10^{-1}$	$1.21\times10^{1}\pm9.5\times10^{-2}$		
0.35	$6.61\times10^{0}\pm5.7\times10^{-2}$	$6.42\times10^{0}\pm5.2\times10^{-2}$		
0.45	$3.71\times10^{0}\pm3.4\times10^{-2}$	$3.59\times10^{0}\pm3.1\times10^{-2}$	$5.35\times10^{-1}\pm1.5\times10^{-2}$	$4.74\times10^{-1}\pm1.3\times10^{-2}$
0.55	$2.09\times10^{0}\pm2.1\times10^{-2}$	$2.06\times10^{0}\pm1.9\times10^{-2}$	$3.83\times10^{-1}\pm9.7\times10^{-3}$	$3.62\times10^{-1}\pm8.8\times10^{-3}$
0.65	$1.24\times10^{0}\pm1.4\times10^{-2}$	$1.21\times10^{0}\pm1.3\times10^{-2}$	$2.66\times10^{-1}\pm6.8\times10^{-3}$	$2.50\times10^{-1}\pm6.2\times10^{-3}$
0.75	$7.63\times10^{-1}\pm9.6\times10^{-3}$	$7.31\times10^{-1}\pm8.4\times10^{-3}$	$1.81\times10^{-1}\pm4.9\times10^{-3}$	$1.78\times10^{-1}\pm4.6\times10^{-3}$
0.85	$4.64\times10^{-1}\pm6.6\times10^{-3}$	$4.60\times10^{-1}\pm5.9\times10^{-3}$	$1.26\times10^{-1}\pm3.7\times10^{-3}$	$1.21\times10^{-1}\pm3.4\times10^{-3}$
0.95	$2.93\times10^{-1}\pm4.8\times10^{-3}$	$2.95\times10^{-1}\pm4.3\times10^{-3}$	$8.85\times10^{-2}\pm2.9\times10^{-3}$	$8.21\times10^{-2}\pm2.5\times10^{-3}$
1.05	$1.91\times10^{-1}\pm3.5\times10^{-3}$	$1.89\times10^{-1}\pm3.2\times10^{-3}$	$6.34\times10^{-2}\pm2.3\times10^{-3}$	$5.80\times10^{-2}\pm2.0\times10^{-3}$
1.15	$1.26\times10^{-1}\pm2.6\times10^{-3}$	$1.28\times10^{-1}\pm2.5\times10^{-3}$	$4.35\times10^{-2}\pm1.8\times10^{-3}$	$3.91\times10^{-2}\pm1.5\times10^{-3}$
1.25	$8.15\times10^{-2}\pm2.0\times10^{-3}$	$8.12\times10^{-2}\pm1.8\times10^{-3}$	$2.87\times10^{-2}\pm1.4\times10^{-3}$	$2.94\times10^{-2}\pm1.3\times10^{-3}$
1.35	$5.96\times10^{-2}\pm1.7\times10^{-3}$	$5.71\times10^{-2}\pm1.5\times10^{-3}$	$2.03\times10^{-2}\pm1.1\times10^{-3}$	$2.07\times10^{-2}\pm1.0\times10^{-3}$
1.45	$3.95\times10^{-2}\pm1.3\times10^{-3}$	$3.91\times10^{-2}\pm1.2\times10^{-3}$	$1.68\times10^{-2}\pm9.7\times10^{-4}$	$1.35\times10^{-2}\pm8.2\times10^{-4}$
1.55	$2.56\times10^{-2}\pm9.7\times10^{-4}$	$2.81\times10^{-2}\pm9.7\times10^{-4}$	$1.06\times10^{-2}\pm7.5\times10^{-4}$	$1.05\times10^{-2}\pm7.0\times10^{-4}$
1.65	$1.96\times10^{-2}\pm8.4\times10^{-4}$	$2.07\times10^{-2}\pm8.1\times10^{-4}$	$8.39\times10^{-3}\pm6.5\times10^{-4}$	$8.47\times10^{-3}\pm6.2\times10^{-4}$
1.75	$1.44\times10^{-2}\pm7.1\times10^{-4}$	$1.41\times10^{-2}\pm6.5\times10^{-4}$	$5.68\times10^{-3}\pm5.2\times10^{-4}$	$5.15\times10^{-3}\pm4.6\times10^{-4}$
1.85	$1.07\times10^{-2}\pm6.0\times10^{-4}$	$1.04\times10^{-2}\pm5.6\times10^{-4}$	$4.91\times10^{-3}\pm4.7\times10^{-4}$	$4.15\times10^{-3}\pm4.1\times10^{-4}$
1.95	$7.68\times10^{-3}\pm5.1\times10^{-4}$	$7.42\times10^{-3}\pm4.8\times10^{-4}$	$3.59\times10^{-3}\pm4.1\times10^{-4}$	$3.29\times10^{-3}\pm3.7\times10^{-4}$
2.05	$5.87\times10^{-3}\pm3.6\times10^{-4}$	$4.87\times10^{-3}\pm3.3\times10^{-4}$		
2.15	$3.78\times10^{-3}\pm2.9\times10^{-4}$	$3.87\times10^{-3}\pm3.0\times10^{-4}$		
2.25	$2.99\times10^{-3}\pm2.6\times10^{-4}$	$2.55\times10^{-3}\pm2.5\times10^{-4}$		
2.35	$2.47\times10^{-3}\pm2.5\times10^{-4}$	$2.41\times10^{-3}\pm2.6\times10^{-4}$		
2.45	$1.68\times10^{-3}\pm2.1\times10^{-4}$	$1.63\times10^{-3}\pm2.1\times10^{-4}$		
2.55	$1.77\times10^{-3}\pm2.3\times10^{-4}$	$1.54\times10^{-3}\pm2.3\times10^{-4}$		
2.65	$1.28\times10^{-3}\pm2.1\times10^{-4}$	$1.18\times10^{-3}\pm2.0\times10^{-4}$		
2.75	$1.02\times10^{-3}\pm2.0\times10^{-4}$	$7.74\times10^{-4}\pm1.7\times10^{-4}$		
2.85	$7.49\times10^{-4}\pm1.7\times10^{-4}$	$6.23\times10^{-4}\pm1.7\times10^{-4}$		
2.95	$5.61\times10^{-4}\pm1.6\times10^{-4}$	$7.27\times10^{-4}\pm1.9\times10^{-4}$		

TABLE XXIX. Invariant yields for protons and antiprotons at midrapidity in 60–92% centrality bin, normalized to unit rapidity. Errors are statistical only.

p_T (GeV/c)	p	$\bar{p}$
0.65	$1.17\times10^{-1}\pm4.8\times10^{-3}$	$8.63\times10^{-2}\pm3.8\times10^{-3}$
0.75	$9.26\times10^{-2}\pm3.9\times10^{-3}$	$7.00\times10^{-2}\pm3.1\times10^{-3}$
0.85	$7.01\times10^{-2}\pm3.1\times10^{-3}$	$5.31\times10^{-2}\pm2.5\times10^{-3}$
0.95	$5.48\times10^{-2}\pm2.6\times10^{-3}$	$4.07\times10^{-2}\pm2.0\times10^{-3}$
1.05	$4.10\times10^{-2}\pm2.1\times10^{-3}$	$2.92\times10^{-2}\pm1.6\times10^{-3}$
1.15	$3.09\times10^{-2}\pm1.7\times10^{-3}$	$2.32\times10^{-2}\pm1.4\times10^{-3}$
1.25	$2.16\times10^{-2}\pm1.3\times10^{-3}$	$1.70\times10^{-2}\pm1.1\times10^{-3}$
1.35	$1.77\times10^{-2}\pm1.2\times10^{-3}$	$1.27\times10^{-2}\pm9.4\times10^{-4}$
1.45	$1.25\times10^{-2}\pm9.4\times10^{-4}$	$1.02\times10^{-2}\pm8.3\times10^{-4}$
1.55	$8.85\times10^{-3}\pm7.8\times10^{-4}$	$6.51\times10^{-3}\pm6.2\times10^{-4}$
1.65	$6.42\times10^{-3}\pm6.3\times10^{-4}$	$4.76\times10^{-3}\pm5.2\times10^{-4}$
1.75	$5.08\times10^{-3}\pm5.5\times10^{-4}$	$3.69\times10^{-3}\pm4.5\times10^{-4}$
1.85	$3.58\times10^{-3}\pm4.6\times10^{-4}$	$2.60\times10^{-3}\pm3.7\times10^{-4}$
1.95	$2.79\times10^{-3}\pm3.9\times10^{-4}$	$2.11\times10^{-3}\pm3.4\times10^{-4}$
2.10	$1.77\times10^{-3}\pm1.8\times10^{-4}$	$1.23\times10^{-3}\pm1.5\times10^{-4}$
2.30	$1.08\times10^{-3}\pm1.4\times10^{-4}$	$7.22\times10^{-4}\pm1.2\times10^{-4}$
2.50	$5.42\times10^{-4}\pm9.5\times10^{-5}$	$3.97\times10^{-4}\pm8.5\times10^{-5}$
2.70	$3.32\times10^{-4}\pm7.4\times10^{-5}$	$2.17\times10^{-4}\pm6.2\times10^{-5}$
2.90	$2.04\times10^{-4}\pm5.8\times10^{-5}$	$1.49\times10^{-4}\pm5.2\times10^{-5}$
3.25	$8.58\times10^{-5}\pm2.3\times10^{-5}$	$5.24\times10^{-5}\pm1.9\times10^{-5}$
3.75	$2.76\times10^{-5}\pm1.3\times10^{-5}$	$1.14\times10^{-5}\pm8.7\times10^{-6}$
4.25	$1.24\times10^{-5}\pm9.1\times10^{-6}$	$5.08\times10^{-6}\pm6.1\times10^{-6}$

[1] See E. Laermann and O. Philipsen, hep-ph/0303042. (Invited article for Annual Review of Nuclear and Particle Sciences.)
[2] J. D. Bjorken, Phys. Rev. D **27**, 140 (1983).
[3] K. Adcox *et al.*, PHENIX Collaboration, Phys. Rev. Lett. **87**, 052301 (2001).
[4] W. Broniowski and W. Florkowski, Phys. Rev. Lett. **87**, 272302 (2001); Phys. Rev. C **65**, 064905 (2002).
[5] D. Teaney, J. Lauret, and E. V. Shuryak, nucl-th/0110037; Phys. Rev. Lett. **86**, 4783 (2001).
[6] K. Adcox *et al.*, PHENIX Collaboration, Phys. Rev. Lett. **88**, 242301 (2002).
[7] C. Adler *et al.*, STAR Collaboration, Phys. Rev. Lett. **87**, 262302 (2001).
[8] K. Adcox *et al.*, PHENIX Collaboration, Phys. Rev. C **69**, 024904 (2004).
[9] F. Becattini *et al.*, Phys. Rev. C **64**, 024901 (2001).
[10] P. Braun-Munzinger, D. Magestro, K. Redlich, and J. Stachel, Phys. Lett. B **518**, 41 (2001).
[11] W. Florkowski, W. Broniowski, and M. Michalec, Acta Phys. Pol. B **33**, 761 (2002).
[12] K. Adcox *et al.*, PHENIX Collaboration, Phys. Rev. Lett. **88**, 022301 (2002).
[13] K. Adcox *et al.*, PHENIX Collaboration, Phys. Lett. B **561**, 82 (2003).
[14] S. S. Adler *et al.*, PHENIX Collaboration, Phys. Rev. Lett. **91**, 072301 (2003).
[15] X. N. Wang and M. Gyulassy, Phys. Rev. Lett. **68**, 1480 (1992); X. N. Wang, Phys. Rev. C **58**, 2321 (1998).
[16] M. Gyulassy and M. Plümer, Phys. Lett. B **243**, 432 (1990); R. Baier and *et al.*, *ibid.* **345**, 277 (1995).
[17] K. Adcox *et al.*, PHENIX Collaboration, Nucl. Instrum. Methods Phys. Res. A **499**, 469 (2003).
[18] M. Aizawa *et al.*, PHENIX Collaboration, Nucl. Instrum. Methods Phys. Res. A **499**, 508 (2003).
[19] L. Aphecetche *et al.*, PHENIX Collaboration, Nucl. Instrum. Methods Phys. Res. A **499**, 521 (2003).
[20] M. Allen *et al.*, PHENIX Collaboration, Nucl. Instrum. Methods Phys. Res. A **499**, 549 (2003).
[21] C. Adler *et al.*, PHENIX Collaboration, Nucl. Instrum. Methods Phys. Res. A **470**, 488 (2001).
[22] K. Adcox *et al.*, PHENIX Collaboration, Nucl. Instrum. Methods Phys. Res. A **499**, 489 (2003).
[23] S. S. Adler *et al.*, PHENIX Collaboration, Phys. Rev. Lett. **91**, 172031 (2003).
[24] S. S. Adler *et al.*, PHENIX Collaboration, Phys. Rev. Lett. **91**, 241803 (2003).
[25] J. T. Mitchell *et al.*, Nucl. Instrum. Methods Phys. Res. A **482**, 491 (2002).
[26] Computer code GEANT 3.21 (CERN, Geneva, 1993).
[27] X. N. Wang and M. Gyulassy, Phys. Rev. D **44**, 3501 (1991).
[28] K. Adcox *et al.*, PHENIX Collaboration, Phys. Rev. Lett. **89**, 092302 (2002).
[29] P. F. Kolb and R. Rapp, Phys. Rev. C **67**, 044903 (2003).
[30] E. Schnedermann, J. Sollfrank, and U. Heinz, Phys. Rev. C **48**, 2462 (1993).
[31] P. Kolb *et al.*, Nucl. Phys. **A696**, 197 (2001); P. Huovinen *et al.*, Phys. Lett. B **503**, 58 (2001).
[32] U. Heinz and P. Kolb, Nucl. Phys. **A702**, 269 (2002).
[33] E. Schnedermann, J. Sollfrank, and U. Heinz, Phys. Rev. C **48**, 2462 (1994); T. Csörgő and B. Lörstad, *ibid.* **54**, 1390 (1996).
[34] T. Csörgő, S. V. Akkelin, Y. Hama, B. Lukács, and Y. M. Sinyukov, Phys. Rev. C **67**, 034904 (2003).
[35] J. Schaffner-Bielich, D. Kharzeev, L. McLerran, and R. Venugopalan, Nucl. Phys. **A705**, 494 (2002).
[36] P. Christiansen, BRAHMS Collaboration, Nucl. Phys. **A721**, 239 (2003).
[37] C. Adler *et al.*, STAR Collaboration, Phys. Rev. Lett. **86**, 4778 (2001).
[38] J. Adams *et al.*, STAR Collaboration, Phys. Rev. Lett. **90**, 119903 (2003).
[39] C. Adler *et al.*, STAR Collaboration, nucl-ex/0206008, Phys. Lett. B (to be published).
[40] J. Adams *et al.*, STAR Collaboration, Phys. Lett. B **567**, 167 (2003).
[41] I. G. Bearden *et al.*, BRAHMS Collaboration, Phys. Rev. Lett. **87**, 112305 (2001).
[42] B. B. Back *et al.*, PHOBOS Collaboration, Phys. Rev. Lett. **87**, 102301 (2001).
[43] I. G. Bearden *et al.*, BRAHMS Collaboration, Phys. Rev. Lett. **90**, 102301 (2003).
[44] B. B. Back *et al.*, PHOBOS Collaboration, Phys. Rev. C **67**, 021901(R) (2003).
[45] R. C. Hwa and C. B. Yang, Phys. Rev. C **67** 034902 (2003); R. J. Fries, B. Müller, C. Nonaka, and S. A. Bass, Phys. Rev. Lett. **90**, 202303 (2003); V. Greco, C. M. Ko, and P. Lévai, Phys. Rev. Lett. **90**, 202302 (2003).
[46] I. Vitev and M. Gyulassy, Nucl. Phys. **A715**, 779c (2003).
[47] B. Alper *et al.*, Nucl. Phys. **B100**, 237 (1975).
[48] P. Abreu *et al.*, DELPHI Collaboration, Eur. Phys. J. C **17**, 207 (2000).
[49] B. Kämpfer, J. Cleymans, K. Gallmeister, and S. M. Wheaton, Heavy Ion Phys. **18**, 1 (2003).
[50] G. C. Rossi and G. Veneziano, Nucl. Phys. **B123**, 507 (1977); D. Kharzeev, Phys. Lett. B **378**, 238 (1996); S. E. Vance, M. Gyulassy, and X.-N. Wang, *ibid.* **443**, 45 (1998).
[51] G. Van Buren, Nucl. Phys. **A715**, 129c (2003).
[52] I. Vitev and M. Gyulassy, Phys. Rev. C **65**, 041902 (2002); I. Vitev, M. Gyulassy, and P. Lévai, hep-ph/0109198 (EPS-HEP 2001 conference proceedings).
[53] J. Adams *et al.*, STAR Collaboration, Phys. Rev. Lett. **92**, 052302 (2004).
[54] J. Cronin *et al.*, Phys. Rev. D **11**, 3105 (1975).
[55] D. Antreasyan *et al.*, Phys. Rev. D **19**, 764 (1979).
[56] M. Lev and B. Petersson, Z. Phys. C **21**, 155 (1983).
[57] B. Z. Kopeliovich, J. Nemchik, A. Schafer, and A. V. Tarasov, Phys. Rev. Lett. **88**, 232303 (2002).